THESIS

# BIOELECTROCHEMICAL PRODUCTION OF GRAPHENE OXIDE USING BACTERIA AS BIOCATALYSTS

Submitted by

Diana Marcela Nunez Hernandez

Department of Chemical and Biological Engineering

In partial fulfillment of the requirements

For the Degree of Master of Science

Colorado State University

Fort Collins, Colorado

Summer 2019

Master's Committee:

Advisor: Susan De Long

Matt Kipper
Justin Sambur

ABSTRACT

BIOELECTROCHEMICAL PRODUCTION OF GRAPHENE OXIDE USING BACTERIA AS BIOCATALYSTS

The demand for production of graphene oxide (GO), which is a precursor for large-scale production of graphene, has been increasing due to the broad array of uses of both nanomaterials. Due to the unique electrical and mechanical properties of these 2D nanomaterials, applications in composites have shown enhancements by contributing a tunable energetic band gap, high strength, and high transparency among other features. The tunable band gap of the graphene derivatives is one of the key properties of these nanomaterials. By varying the size of the energetic band gap (in eV) between the conduction and valence bands, resistance can be decreased to promote electron flow in the material lattice. Being able to control the band gap of a nanomaterial, allows for many applications in batteries, supercapacitors, and semiconductors being the most promising applications for these nanomaterials. Other applications include flexible electronics, renewable energy, drug delivery, contaminant removal, sensors, and more. Unfortunately, large-scale production of graphene using current methods is challenging due to low yield, impurities, high cost, high energy input, slow production rates, and/or hazardous chemical reactants and wastes. For this study, the focus was on the bioelectrochemical production of GO (BEGO) as a novel technology for producing these nanomaterials with low energy input, inexpensive and non-hazardous reagents at standard conditions, and using microbes as biocatalysts. The BEGO process consists of a single-chamber microbial electrosynthesis cell (MES) that uses a graphite rod anode and a cathode (carbon cloth or

stainless steel) to drive redox reactions. This MES can be operated at low voltage in a three-electrode (-0.8-1.4V vs. Ag/AgCl), or two-electrode system (~3.1V DC), with bacteria inoculated in a phosphate media solution.

During this study, the BEGO process was investigated to advance understanding of the production process and the properties of the BEGO nanomaterial produced. To achieve this, the objectives established include: 1) developing methods for purifying and quantifying the nanomaterial during the production process in the complex aqueous-phase reactor matrix, 2) identifying key physical and chemical properties of the nanomaterial product using various spectroscopy and microscopy techniques, and 3) analyzing the microbial communities present in the reactors and in the graphite anode biofilm.

To quantify the BEGO and estimate production rates, different spectrophotometric and gravimetric methods were used. Ultraviolet-visible spectroscopy (UV-Vis) at 229 nm was found to be the best method. This wavelength is specific to GO as it corresponds to the $\pi \rightarrow \pi^*$ transitions of aromatic C-C bonds comprising the majority of the molecule, regardless of the oxidation state. Different centrifugation and filtration protocols were compared to purify the BEGO out of the complex matrix. For quantification methods in solution, centrifugation at 10,000 x g for 15 minutes was found to be the most effective method for removal of large particles and biological material, with BEGO remaining in solution.

For material characterization, various techniques were used to identify the functional groups present and the morphology of the BEGO sheets. It was found through Fourier transform infrared spectroscopy (FT-IR) and UV-Vis, that the nanomaterial contained less carboxyl/carbonyl groups than GO produced by the traditional Hummers' method. Raman spectroscopy and thermogravimetric analysis (TGA) showed disorder peaks and weight loss

events consistent with known GO spectra. Microscopy analysis revealed the BEGO process yields sheet sizes of a few hundred nm to 1-2 μm in lateral dimensions. Transparency and Fast Fourier transform (FFT) images indicated the BEGO consists of only single-layered to few-layered structures, which are needed for downstream applications.

The microbial analysis was done on bioreactors with different inocula sources. DNA and RNA were extracted from both the bulk liquid media and the rod biofilm. At the end of the operation period, microbial communities in the bioreactors had diverged from the inoculum source. Microbial communities in the BEGO producing reactors consisted of both aerobic and anaerobic microorganisms. The most abundant genera on the rod biofilm were the unclassified *Comamonadaceae* (10-11%), *Hydrogenophaga* (9-21%), *Methyloversatilis* (15-22%), and *Pseudomonas* (11-36%) all from the *Proteobacteria* phylum. These microbial phylotypes may play a key role in catalyzing BEGO production, enabling this novel and sustainable approach to nanomaterial synthesis.

# ACKNOWLEDGEMENTS

I would like to start by thanking my father. He is my inspiration and the reason why I am here today. Thank my family and friends, for supporting me in every possible way throughout this journey.

My adviser Dr. Susan De Long, for being such a wonderful person who encouraged me and supported me through every possible challenge, I am truly grateful to have had her during this experience. I also would like to thank Dr. Charles Henry who was an incredible source of knowledge and resources throughout my research. My committee members: Dr. Matt Kipper for his incredible support and understanding throughout my class work, and Dr. Justin Sambur for providing us with insightful ideas within our research.

Within their teams, I would like to express my sincere gratitude to Dr. Karen Rossmassler and Jorge Rico from De Long's group for their incredible support helping me collecting and analyzing microbial data. I thank Dr. Rob Channon, Dr. Kevin Klunder and Dr. Shirley Yang from Henry's group, for their advice and knowledge on electrochemistry and characterization tools. From Kipper's group I would like to thank Mohammadhasan Hedayati and from Sambur's group, Zach Nilsson for collaborating with characterization data analysis and collection.

Other collaborators include Noelle Fillo, Nick Santiago, Larry Lien, Dr. Jens Blotevogel, Dr. Jason Ren, and Dr. Lauren Greenlee for supplying us with knowledge and other resources. From the chemistry instrumentation facility, I would like to thank Patrick McCurdy and Roy Geiss and from the proteomics and metabolomics facility, Jaqueline Chaparro for taking the time to teach me to use and understand different instrumentation necessary for my research.

Last but not least, a thank you to my sponsors at BEGO Advanced Materials Inc, Song Jin and Paul Fallgren for bringing this project to the team and providing us with knowledge, support, funds, guidance and friendship. This project was a large piece of work that required many different minds working together and it wouldn't have been possible without every single person that helped me along the way. I am truly grateful to each and every one of you.

TABLE OF CONTENTS

LIST OF TABLES

LIST OF FIGURES

# LIST OF ACRONYMS

AFM: Atomic force microscopy
AU: Absorbance units
BES: Bioelectrochemical system
BEGO: Bioelectrochemically produced graphene oxide
CAGR: Compound annual growth rate
cDNA: Complementary DNA
CNT: Carbon nanotubes
COD: Chemical oxygen demand
CSU: Colorado State University
CTR: Continuous tubular reactor
CV: Cyclic voltammetry
DC: Direct current
DI: Deionized water
dCOD: Dissolved chemical oxygen demand
DNA: Deoxyribonucleic acid
DOX: Doxorubicin.
EDS: Energy dispersive X-ray
EKG: Electrocardiography
FBS: fetal bovine serum
FET: Field-effect transistors
FFT: Fast Fourier transform
FRET: Fluorescence resonance energy transfer
FT-IR: Fourier-transform infrared spectroscopy
G: Graphene
GC: Gas chromatography
GO: Graphene oxide
rGO: Reduced graphene oxide
HOPG: Highly oriented pyrolitic graphite
ICP-MS: Inductively coupled plasma mass spectroscopy
LED: light-emitting diode
LSR: Large-scale reactors
LSRA: Abiotic large-scale reactors
LSRB: Biotic large-scale reactors
MES: Microbial electrosynthesis systems
MWCO: Molecular weight cut-off
NADH : β-nicotinamide adenine dinucleotide
NIR: near-infrared
NMR: Nuclear magnetic resonance
PEG: polyethylene glycol
PVC: Polyvinyl Chloride
RE: Reference Electrode
RNA: Ribonucleic acid

rRNA: Ribosomal ribonucleic acid
RPM: Revolutions per minute
RT: Reverse transcription
SAED: Selected area electron diffraction
SAXS: Small-angle X-ray scattering
SEM: Scanning electron microscopy
SERS: Surface-enhanced Raman scattering
SHE: Standard hydrogen electrode
ssDNA: single-stranded DNA
SSR: Small-scale reactors
STEM: Scanning transmission electron microscopy
STM: Scanning tunneling microscopy
TCD: Thermal conductivity detector
TEM: Transmission electron microscopy
TGA: Thermogravimetric analysis
TOC: Total organic carbon
UV: Ultraviolet
UV-Vis: Ultraviolet-visible spectroscopy
WAXS: Wide-angle X-ray scattering
WE: Working electrode
XPS: X-ray photoelectron spectroscopy
YM: Young's Modulus

# 1. INTRODUCTION

Graphene is a two dimensional layer of carbon atoms arranged in a honeycomb lattice that form graphitic materials through Van der Waals interactions. Graphene sheets are the building blocks for larger materials including carbon nanotubes, fullerenes, multilayer graphite, and even diamond [1]. This wonder nanomaterial has gained interest due to its unique physical and chemical properties. Graphene possesses a high electrical and thermal conductivity (~ 5,000 $Wm^{-1}K^{-1}$) [2], large theoretical specific surface area (2,630 $m^2g^{-1}$), high Young's Modulus (~1.0 $TPa$) [3], high optical transmittance (~97.7%) [4], remarkably high carrier mobility (200,000 $cm^2v^{-1}s^{-1}$) [5], high flexibility, and biocompatibility. All of these properties make graphene an attractive additive in composites in many field including electronics, sensors, energy storage, contaminant removal, biotechnologies, aerospace and even fabrics.

## 1.1 Motivation

Current production methods for graphene have proven to be quite challenging to scale up. Issues including low yield, impurities, high cost, high energy input, and time-consuming processes, have driven the need for better production alternatives [6]. Current methods of graphene production include chemical vapor deposition growth [7], metal ion intercalation [8], micromechanical peeling [9,10], thermal decomposition of carbides [11], synthesis from aromatic hydrocarbons [12–14], and reduction from GO [15,16]. The latter manufacturing technique, reduction from GO, is one of the most promising, scalable, low cost techniques due to effective graphite exfoliation. Exfoliation (i.e., disruption of the contiguous graphitic aromatic lattice) is possible via intercalation of oxidizing agents that introduce oxygen containing groups and defects into the graphite layers [17]. The result is single/few-layered graphene structures

with various oxygen groups attached to the surface. These oxygen groups can be then removed using different thermal and chemical methods to produce reduced graphene oxide (rGO) or graphene.

Although GO is valued for its role in the production of graphene, GO is highly valuable in its own right, capable of enhancing the mechanical and electrical properties in composite materials. Areas of interest include electronics, sensors, contaminant removal and biotechnologies [4]. Although GO is easier to produce on a large-scale than graphene, most chemical methods involve strong acids bases, generate hazardous waste, or are simply time consuming. Better techniques for GO production that are more environmentally friendly are necessary to avoid further treatment of hazardous by-products [18]. A new GO production method involving microbial electrosynthesis (MES) cells has emerged as a potentially cost-effective and sustainable alternative to traditional techniques [19]. The bioelectrochemical production of GO (BEGO) process is expected to offer competitive advantages including substantially reduced production costs due to ambient reactor conditions, minimum consumables, very low energy consumption, and minimum hazardous waste. Previous work done by Lu et al. has also shown $H_2$ production as a byproduct that can potentially be used to fuel parts of the process [19]. The BEGO process showed improved GO production in the MES when *Pseudomonas syringae* strains were present compared to the counterpart abiotic electrosynthesis cell. With lower cost materials and the use of microorganisms as biocatalysts, it is expected that the BEGO process could reduce the overall manufacturing cost while increasing the production rate of GO.

There is an increasing need for graphene-based materials that needs to be filled with reliable bulk production techniques. A report by Market Watch reported a compound annual

growth rate (CARG) of 44.4% for a projected $311.2 million by 2022 for graphene based materials [20]. A different report by Grand View Research projected a CAGR of 38% from 2017 to 2025 forecasts a global graphene market (graphene nanoplatelets and graphene oxide) of $552.3 million by 2025 [21]. Demand for graphene-based materials is expected to grow significantly in the next few years and this trend is expected to continue growing once reliable bulk production becomes available.

### 1.2 Objectives

This study focused on further developing the BEGO process. Different sources of microorganisms and electrochemical parameters were explored in order to determine their effects on the production of BEGO. This process was discovered by Lu et al. [19]. They observed higher GO production in a single chamber MES under micro-aerobic conditions compared to a sterile counterpart. Lu et al. hypothesized that microbial communities forming biofilms on reactor anodes catalyze GO production, perhaps via enzymatic redox reactions. The overarching goal of the BEGO research at Colorado State University (CSU) is to further develop this new technology towards achieving a scalable production method that does not produce harmful byproducts and uses low energy input.

To further understand the BEGO process, different reactor configurations were used to test the different parameters. Small-scale reactors (SSR) were inoculated with various microbial sources and run in a three-electrode configuration to understand the impact of different microbial communities on performance. Large-scale reactors (LSR), 8L each, were then built and run using one of the three inoculum sources chosen based on the SSR trial to produce higher quantities of BEGO for downstream testing. The material produced by both the SSR and LSR was investigated using different microscopy and spectroscopy techniques to gather information about

the BEGO properties. By better understanding the surface chemistry of the BEGO, possible applications can be targeted by comparing with other GO products currently on the market. Reduction of the GO was considered by our research collaborators but is only briefly mentioned in this study. The key objectives of this study were:

1. To measure BEGO production rates using multiple techniques and investigate the impact of selected operating parameters on rates
2. To identify key physical and chemical properties of the BEGO produced
3. To compare different inocula and identify microorganisms present in both the bulk solution and the graphite rod biofilm.

Data were generated using either the SSR and/or the LSR, depending on the sample volumes needed. Results were compared between reactor types and between replicates when possible. Additionally, due to the novelty of the studied technology, future work and improvements to the system design and running conditions were suggested to further advance the BEGO technology.

### 1.3 Thesis overview

Chapter 2 focuses on background information mainly for GO and rGO nanomaterials. Key physical and chemical properties are identified along with potential structural models. History of the discovery of GO and current production methods are described briefly, as well as their downsides. Characterization techniques used for the GO/rGO are described as well as the type of information attained with each technique. Knowledge regarding carbon/oxygen ratios, types of functional groups, sheet dimensions and topography information can be obtained from the techniques discussed. A detailed section on GO and rGO applications is included with examples in different fields such as electronics, energy, and biotechnologies. Finally, the BEGO

technology is introduced with background information about MES and their application in redox reactions. The previous study done by Lu et al. [19] is described as well as the parameters previously explored and information obtained. The benefits of this new greener alternative that could increase bulk production are also discussed here.

In Chapter 3, the experimental approach, materials, and methods are described. The construction of the SSR and the LSR, run as two-electrode and three-electrode configurations, is explained. Descriptions of the different inoculum sources, inoculation protocols, and operating conditions are included here. Details regarding voltages, currents, pH, and sampling time points are documented. A section describing purification methods for BEGO including centrifugation, and filtration protocols is also included. The characterization techniques and the sampling methods are described including instrumentation specifications. Finally, protocols and techniques used for genomic analysis are outlined including sample handling, nucleic acid extractions, and gene sequencing.

In Chapter 4, results and discussion for each one of the objectives are reported. Section 4.1 focuses on the development of methods to quantify rates of BEGO production (Objective 1). Different quantification estimation techniques were explored as well as purification methods. Comparisons between inocula sources, reactor configurations, and controls are described in detail. Section 4.2 describes the material characterization results in detail compared with purchased GO standards and literature findings (Objective 2). BEGO produced was inspected for functional groups, dimensions, purity, and number of layers present. To address this objective, various microscopy and spectroscopy techniques were used to better understand the properties of the BEGO. The last section (4.3) reports results from the DNA and RNA analysis (Objective 3).

Comparisons of the communities present in both the bulk phase and the rod biofilm are described.

Finally, Chapter 5 includes conclusions from the work done, and Chapter 6 covers suggestions for future work needed to optimize the MES. The goal is to continue increasing the understanding of the BEGO technology until industrial-scale applications can be achieved.

# 2. BACKGROUND ON GRAPHENE DERIVATIVES

GO is a two-dimensional carbon nanosheet composed of planar carbon atoms arranged in a honeycomb structure (see proposed models in Figure 1). Unlike graphene, GO is functionalized with oxygen groups on its basal plane and edges. These groups result from the production methods that involve the intercalation of oxygen groups to separate the individual sheets. The sheets are approximately an atom thick and can range from a few nanometers to several micrometers in lateral dimensions depending on the production process [22]. GO can be altered through different mechanisms to become reduced GO (rGO). Because of the different production technologies available, the physical and chemical properties of GO and rGO are tunable, allowing these nanomaterials to have a wide range of applications. This tunability is a result of the variations in purity, oxygen content, number of layers, dimensions, and type of functional groups present and is highly dependent on the chosen production method [4]. The graphitic source can also contribute to variations in the GO properties. Since GO is a nonstoichiometric macromolecule, characterization can be challenging due to the variations of the functionalized groups. Many different spectroscopy and microscopy techniques are required to understand the physical and chemical properties of the final product.

Producing pure, single-layered GO, rGO and/or graphene has proven challenging. Most technologies produce a mixture of multi-layered, few-layered, and single-layered materials. Single layer nanomaterials are desired as the electronic properties can vary extensively with additional layers. The one atom thick layers of carbon atoms that are attached by $sp^2$ hybridized bonds have high electron mobility. This high mobility is due to the fact that electrons in the single-layered graphene-like film are confined to only two dimensions; free electrons move more

easily along the planes than through the planes, giving graphene much higher electron mobility than multi-layer graphitic materials [23].

GO and graphene derivatives have gained popularity in the market, due to their high surface area and high thermal and electrical conductivities [24]. Although GO and rGO vary in properties from graphene due to the interrupted $sp^2$ bonds, the oxidized materials have their own valuable optical, and electrical properties that can be exploited in other fields alone or in composites [4,22]. In depth analysis of the structures and physical/chemical properties is necessary to understand and exploit the value of these 2D crystals in today's technologies [25].

## 2.1 Physical and chemical properties of GO and rGO

### *2.1.1 Theoretical structure and stabilities*

Different structural models have been proposed depending on the identified oxygen containing functional groups and C:O ratios of the produced GO (see Figure 1). These models support understanding of the physical and chemical properties of GO as well as stabilities of the functional groups. Different degrees of oxidation and number of layers are a result of the choice of production method. Due to these differences, GO/rGO has tunable properties that can change with further reduction, exfoliation, and even doping.

The structural models that have been proposed consist mainly on epoxide and hydroxyl functional groups. Many studies have proposed different possible arrangements of these functional groups, but most of them agree that it is energetically favorable to have two neighbor hydroxyl groups present on different sides of the GO plane. It is also favorable to have epoxide dimers in the same pattern, as electrons have a better flow path in this configuration [26]. The epoxide and hydroxyl groups distribute closely together, leading to formation of hydrogen bonds. This arrangement lowers the total energy of the system, which is consistent with previous

theoretical predictions [27–30]. The clusters arrayed in these patterns lower the steric hindrance and help keep the layer structure from rolling up into nanotubes.

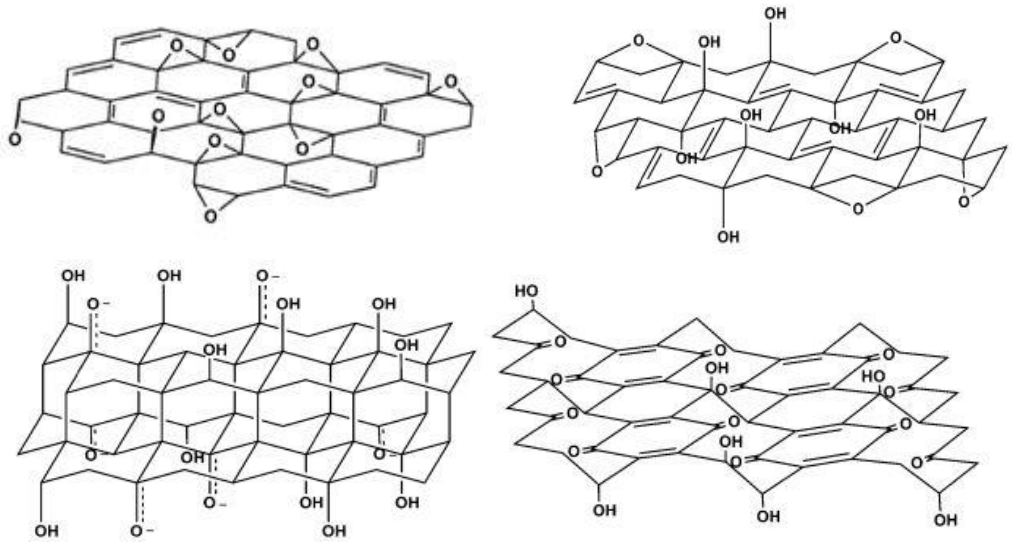

**Figure 1**: Proposed GO structure models. In order, structures found are the Hofmann model (upper left), the Ruess model (upper right), the Nakajima-Matsuo model (lower left), and the Sholz-Boehm model (lower right). Pictures were taken from Wikimedia commons.

Depending on the production process, small holes (or vacancies) due to C-C bond breakage can be formed on the plane. The carbon bonds are more likely to break during reduction methods after the thermal annealing processes (rapid heating >2000°C/min) if epoxide and hydroxyl groups are in close proximity leaving behind these vacancies. The vacancies are even more predominant in areas with localized motifs of clustered epoxide and/or hydroxyl groups. In general, having the clusters is thermodynamically stable. These stability trends and models' predictions are in accordance with experimental observations [31–33].

As for the thermal stability, GO is usually unstable and can change structure if heated. During heating, $CO_2$ gas can be released from decomposing functional groups at as low as 50°C depending on the structure [34]. Under thermal treatment adsorbed water and unstable hydroxyl

groups are removed at around 100°C. At around 200°C the more stable functional groups decompose drastically; no additional significant losses are detected above 800°C. Some structural models predict functional group coverage to be in between 25% and 75% for stable structures. During the heat loss events, coverage can be reduced from 75% to as low as 6.25% (C:O ratio 16:1) [26]. Removal of clustered hydroxyl and epoxy groups can be more difficult than removal of unclustered groups since the formation of these make the structure more stable as previously described.

Differences in structural stability can be affected by pH differences in the solvent in which the GO is being produced. Acid and base exposure can have drastic effects on the GO structure at elevated temperatures (~40°C), but effects are negligible at lower temperatures (~10°C) [35]. Some studies have shown treatment after production with bases favoring hydroxyl group formation whereas treatment with HCl or water favors ether groups. Oxidation of graphene (or graphite) is an exothermic process. Producing a GO with high surface coverage with oxygen groups lowers the formation energy, which is energetically preferable [30]. A higher OH:O ratio increases the stability of the molecule mainly due to increased hydrogen bond formation. Also, ordered GO has been found to be more stable than amorphous GO [36].

GO has an ambiguous chemical formula that depends on the oxygen functional groups present. There are a wide range of possible GO structures that vary depending on functional groups present, their relative abundance, and their arrangements across the planar structure. These functional groups are found to be mainly present on the sheet edges, and when they are present over the sheet plane, they are usually evenly distributed (except for clusters) [4]. Typically GO has a C:O ratio of between 4:1 and 2:1 [37], but this ratio varies substantially among production techniques.

### *2.1.2 Mechanical properties*

GO and rGO have some key structural, properties including high strength, flexibility and transparency. These materials are derivatives of graphene, the strongest material ever recorded with a YM of around 1TPa [3] compared to that of diamond around 1,050 GPa [38]. Unlike graphene, GO/rGO materials have introduced defects as functional groups creating holes in their plane that weakens the structure drastically. Some articles have reported a YM for monolayer rGO of about 250 GPa with a standard deviation of 150 GPa [39–41]. Most of the functionalized C-C bonds will reshape into the honeycomb structure after reduction, removing the majority of these defects. Doping of GO/rGO sheets with alkali earth metals, such as $Mg^{2+}$ or $Ca^{2+}$, can enhance their mechanical strength [42]. Factors that can affect the strength of these nanomaterials include coverage, arrangement, type, and ratio of the functional groups present. GO sheets are also highly flexible, which makes attractive in applications including bendable electronics and fabrics [43].

### *2.1.3 Electronic properties*

GO sheets are usually insulating due to the $sp^3$ defects that increase electron path resistance (around ~$10^{10}$ ohm/sq). GO insulating behavior depends on the degree of coverage with oxygenated groups [44–46]. These resistances can be lowered by reducing GO into rGO and recovering the aromatic structure with the increasing fraction of $sp^2$ carbons that favor electron displacement [47]. Depending on the GO composition and reduction process chosen, the rGO will reach a threshold where the conductivity cannot be increased any further. It should be noted that resistances could increase with increasing number of GO layers, due to a decrease in electron mobility once the free path is extended to three dimensions and electrons scatter.

The energy band gap of GO/rGO materials can be tuned with the presence of oxygen groups. The tunable band gap is one of the key properties of these nanomaterials. By varying the size of the energetic band gap (in eV) between the conduction and valence bands, resistance can be decreased to promote electron flow in the honeycomb lattice. A large band gap (insulators) means more resistance for electron flow. By tuning the size of the band gap a material can behave as an insulator, a conductor or a semiconductor. Graphene by itself has no band gap which results in a theoretical electron mobility of the speed of light [23]. By adding functional groups to the surface of graphene, this band gap forms (and increases) allowing GO and rGO to behave as insulators or semiconductors respectively. Trends show an increase of the band gap with increase in O:C ratio [48]. Studies have shown that GO is conductive at around 25% coverage or less, and is an insulator at larger percentages [26].

### *2.1.4 Optical properties*

GO and rGO monolayers are transparent. These materials have high optical transmittance in the UV range with values recorded as high as 96% at 550 nm [49]. The sheets are semitransparent for few-layered films and become opaque for multi-layered graphite. Reduction of GO into rGO can decrease optical transmittance due to the fact that the vacancies and defects ($sp^3$ carbon) abundant in GO allow more photons to pass through [49–51]. This effect can be ascribed to the increased concentration of $\pi$ electrons in rGO. Since the reduction process increases the $sp^2$ carbon bonds, the GO light absorption is dominated by $\pi$–$\pi^*$ transitions [51].

Other optical properties of GO are its intrinsic fluorescence in the near-infrared (NIR), visible, and UV regions [50]. While graphene does not display intrinsic fluorescence due to the lack of energy gap [52], some studies have reported visible photoluminescence [53] and a weak blue fluorescence around 440 nm [51]. These optical properties can be useful in detection

applications such as sensors (see section 2.4.1). As with the mechanical and electrical properties of GO/rGO, these optical properties are also tunable depending on oxygen content and number of layers. These properties can also be altered by doping or hybridizing with other elements, polymers or nanomaterials.

## 2.2 Current Production Technologies

As previously mentioned, graphene can be produced using chemical, mechanical, and thermal techniques, but one of the most reliable methods for bulk production is formation by reduction from GO. Most of the popular techniques for GO production (e.g., Hummers' method) use strong acids and bases and release toxic gases. Alternatively, GO can be produced at ambient temperatures by electrochemical exfoliation of graphite using various electrolyte solutions, voltages and cathode materials [54]. Methods of GO production are introduced in the following section with their issues and challenges.

### *2.2.1 History of GO Fabrication and Existing Production Methods*

GO can be obtained either by producing graphite oxide and then exfoliating it to obtain single sheets or by producing graphene and oxidizing directly. Since the production of graphene is usually the end goal, only the former method is discussed in this study. GO is not a naturally occurring material. It was discovered in 1859 by Brodie who accidentally synthesized GO by combining a mixture of $KClO_3$ with a slurry of graphite in $HNO_3$ at 60°C during an experiment designed to analyze the structure of graphite. He found that the overall mass of the product had increased. Further analysis showed the new material had a formula of $C_{2.19}H_{0.9}O$ [55,56]. In 1898, Staudenmaier improved Brodie's method by adding concentrated $H_2SO_4$ as well as chlorate in multiple aliquots throughout the reaction for a product similar to Brodie's (C:O ~ 2:1), but more practically in a single reaction vessel [57]. In 1958, Hummers and Offerman

reported the method most commonly used today. Graphite previously treated with $NaNO_3$ in concentrated $H_2SO_4$, was reacted with $KMnO_4$ to catalyze the reaction producing a brown sludge that was then treated with water and hydrogen peroxide ($H_2O_2$) [4]. Sonication was used to further separate the individual layers [58]. The chemical production of GO is a simple, relatively fast process. However, it has the drawback of using harsh acids and bases and generating toxic gases including $NO_2$, $N_2O_2$, and or $ClO_2$; the latter is also an explosive gas [59].

Since the early 1980s, electrochemical production of GO has been researched as a single step, environmentally friendly approach. These electrosynthesis reactions can be conducted in aqueous solutions (with acids or surfactants) and non-aqueous solutions (organic or ionic liquids) under ambient conditions [54]. These processes have the advantage of being fast, inexpensive, and using less harmful reagents. A constant potential (or current) is usually applied to maintain the electrochemical conditions constant. This process involves intercalation of cations or anions to separate individual sheets from the graphite followed by exfoliation. Electrochemical processes produces GO sheets with fewer defects compared with chemical methods, which allow for less harsh reduction methods for conversion into rGO. The choice of the electrolyte is crucial to ensure GO flakes remain in solution and do not aggregate [60]. The electrochemical process can be run as a two-electrode or three-electrode system with graphite as the working electrode (WE), or anode, applying a positive potential to drive the oxidation process. This potential can be optimized to decrease the extent of side reactions that release $CO_2$ and $O_2$ gases, increasing the efficiency of the reaction process [61]. This method has potential for large-scale applications if optimized. Current methods that successfully produce few- to single-layered sheets require at least one of the following: applied potentials from -15V to 15V, expensive electrodes such as HOPG (highly ordered pyrolytic graphite) or Pt, and/or acidic electrolyte solutions that require

proper disposal [54]. Reactions can also be done at relatively low voltage (-2 to 2V) in exchange for reduced rates, which are not suitable for scale up. There is potential for scaled-up production using electrochemical systems for better quality GO. Methods using lower voltage, readily available electrodes, and simple electrolyte solutions can further decrease cost of these processes.

### *2.2.2 Mechanism of GO production from graphite*

GO formation whether chemically or electrochemically produced, follows a similar mechanism regarding a 3 step process [62]. Ions in solution intercalate into the graphite. This step is an intermediate step and occurs almost immediately upon introduction of the graphite to acidic oxidizing medium (often sulfuric acid intercalates in the modified Hummers' method or in electrochemical methods using $H_2SO_4$ in the electrolyte solution). Depending on the solvent, ions in solution, graphite source, and method chosen, the graphite intercalated compound reaction rates might vary, but the concept remains the same. During the second step, the intercalated graphite converts into oxidized graphite oxide with the introduction of an oxidizing agent. This step occurs at a much slower rate than the first one, taking between hours and days. Finally, the graphite oxide is exposed to water causing hydrolysis of the covalently bonded ions (i.e., sulfates) and loss of the interlayer registry. This process occurs gradually starting on the edges of the graphite moving to the center until all of the graphitic material has been converted to GO.

Electrochemical methods rely on the anodic oxidation occurring when a positive potential is applied to a graphite anode. The process promotes the intercalation of anions that lead to the structural expansion of the graphite during exfoliation [63]. Intercalation of acidic anions has been reported as the main mechanism for surface blister formation in previous papers using HOPG as the anode [64,65]. These studies reported hydrolysis resulting in hydroxyl groups (amongst others) that allow the graphite surface to become of hydrophilic nature. The

hydrophilic behavior becomes beneficial in DI water as GO is stable in solution making the reaction favorable to allow exfoliation of the individual flakes [66]. As with chemically produced GO, the use of sulfuric acid can cause excessive oxidation increasing the resistivity and damage the $sp^2$ lattice [67]. Electrochemical methods have been found to be faster and to produce GO containing less defects than the chemically produced methods [68].

### *2.2.3 Existing Reduction Methods*

GO is usually thermally unstable and can be reduced by removing the oxygen groups attached through thermal, chemical or electrochemical processes. A GO molecule typically has a C:O ratio between 4:1 and 2:1 depending on the production technique [69]. After reduction, the C:O ratio can range from 12:1 to 246:1 for the most efficient methods. Reduction can be achieved thermally through annealing at high temperatures, microwave irradiation, and photon irradiation, among other methods. Chemical reduction is based on adding reducing agents to remove the oxygen groups. These methods are usually cheaper than heating because they can be done at room temperature or with moderate heating [69]. The most widely used reagent for reduction is hydrazine ($N_2H_4$) and its derivatives; hydrazine reduction processes result in a rGO product with a C:O ratio of about 12.5:1. Combinations of both chemical and thermal methods into multistep reduction processes have also been reported to increase this ratio [70–79].

Some other common reducing agents used include metal hydrides, such as sodium borohydrate, sodium hydride, and lithium aluminum hydride. These are common reducing agents used in organic chemistry, but they have the drawback of being reactive with water and thus other solvents are needed [69]. More recent studies using hydroiodic acid as a reducing agent have reported higher achieved conductivity than the previously described methods [80,81]. Ascorbic acid (Vitamin C) has also been used as a substitute for hydrazine. It is a more

advantageous chemical as it is non-toxic and does not result in aggregation of rGO colloids [82]. Aggregation is a common issue because reduction processes increase hydrophobicity. Other reducing agents include strong alkaline solutions (sodium/potassium hydroxide), hydroquinone [83], pyrogallol, hydroxylamine [84], alcohols, iron/aluminum powder, ammonia, hexylamine, sulfur-containing compounds ($NaHSO_3$, $Na_2SO_3$, $Na_2S_2O_4$, $Na_2S_2O_3$, $Na_2S{\cdot}9H_2O$, $SOCl_2$, and $SO_2$), urea, lysozyme, N-methyl-2-pyrrolidinone, poly(norepinephrine), BSA, $TiO_2$ nanoparticles, manganese oxide, and bacteria [85]. Electrochemical removal of the oxygen containing groups is also possible under standard conditions by exchanging electrons between the GO and the electrodes [43-46]. All of these alternative methods of reduction are usually not as effective as hydrazine or sodium borohydrate and produce a material with lower conductivity.

The removal of functional groups can be harmful to the GO structure and cause defects throughout the reduction process by introducing vacancies. These vacancies mainly occur in areas of the surface where clustered functional groups are present on the GO as previously mentioned. These type of defects can drastically worsen the electrical properties of the graphene sheets by decreasing the path length due to the introduction of scattering centers [31]; therefore choosing the correct reduction technique is crucial for the desired applications. During the reduction process, hydroxyl and epoxy groups are the first to be removed before carbonyl groups, which have a higher energy barrier due to their formation being thermodynamically and kinetically favorable on GO [86]. $Sp^2$ bonds may reform depending on the functional groups leaving the plane and their arrangement on the plane.

### 2.3 Characterization Techniques

Different techniques are needed to identify the different functional groups present, and the morphology (and topography) of the GO. Spectroscopy techniques used to identify the

functional groups present include nuclear magnetic resonance (NMR), Fourier transform infrared spectroscopy (FT-IR), Raman spectroscopy, X-ray photoelectric spectroscopy (XPS), X-ray absorption near-edge spectroscopy (XANES), ultraviolet-visible spectroscopy (UV-Vis) and more. These techniques are used to identify concentrations of hydroxyl groups, carbonyl groups, epoxide groups, methylene defects and their relative abundance [4]. These data provide insights into the electrical properties (conductor or insulator), the stability in water (hydrophobic or hydrophilic), the active sites present, the $sp^2/sp^3$ bond ratios and the C:O ratio (degree of oxidation).

Microscopy techniques are used to look at the morphology, structure, and number of layers present on the GO. Transmission electron microscopy (TEM) is a common technique used to determine the atomic structure of nanomaterials. Images of the crystal lattice and topological defects are visible, and transparency can be determined compared with carbon films [87]. Areas with clustered oxygen groups will have higher transparency compared to $sp^2$ bonded carbon. Selected area electron diffraction (SAED) patterns of the TEM images also can be obtained from a region of the GO film to show that the graphene honeycomb structure is present. Similar information regarding the GO structure can be obtained using other techniques including atomic force microscopy (AFM), scanning transmission electron microscopy (STEM), and scanning tunneling microscopy (STM) [4]. Other useful information obtained from microscopy techniques includes topography measurements and analysis of the YM, flexibility, elasticity, and conductivity measurements.

These characterization techniques are also useful for measuring the extent of reduction after a chemical or thermal process is performed on the GO. The functional groups and C:O ratios can be observed before and after treatment through these spectroscopy techniques to

monitor changes. The transparency can also decrease due to $sp^2$ bonds being reformed and can be seen via microscopy techniques. Topography measurements can be done to look at the roughness and spacing between the layers of the GO/rGO materials to estimate number of sheets.

## 2.4 Current applications

Oxidized graphene derivatives can vary drastically in their electronic properties as previously described in section 2.1.3. Because of the variations in band gap size, these nanomaterials can act as conductors, insulators, and even semiconductors. Doping with different metals or polymers can change this band gap and further reduction can increase the conductivity [4]. Because of these tunable properties, there are a wide range of applications for oxidized graphene derivatives. This chapter, however, is specifically focused on the applications of oxygenated graphene (GO and rGO). Although one of the largest applications of GO/rGO materials is the production of graphene, these oxidized nanomaterials can have important features in other fields. Moreover, the existence of more effective production methods for GO/rGO, gives these materials an advantage over graphene in some applications.

Other than graphene production, uses for GO and rGO materials include electronics, opto-electronics, energy storage and conversion, sensors, flexible/bendable thin-films, composites, coatings, catalysts, pharmaceutical carriers, and water treatment [51]. Demand for graphene-based materials is expected to grow significantly in the near future [88]. Due to the increasing need for understanding graphene-based materials and production methods, there has been a major increase in publications and patents over the past 10 years. As we move forward with deciphering the methods of production and applications of these wonder materials, projections for GO/rGO nanomaterials could potentially replace silicon in multimillion dollar

industries including semiconductors and other nanotechnologies. Applications in various other fields are described below.

### *2.4.1 Electronics and optics*

The electronic and optical properties of GO/rGO can be changed drastically via different reduction methods as well as by depositing metals on the sheet surfaces. With these modifications, GO and rGO can have behave as insulators, semiconductors or semimetals, which gives them wide ranging applications in the electronics field. Since GO and rGO are transparent, they have potential applications in areas such as solar cells, organic light-emitting diodes (LEDs), and displays [45,89–91]. The high flexibility of GO/rGO has made possible the creation of innovative electronics, such as flexible phones and electrocardiography (EKG) sensing tattoos [92]. Field-effect transistors (FET) are also an appealing application as pristine graphene possesses higher electron mobility than silicon semiconductors [6]. Pristine graphene has low $I_{ON}/I_{OFF}$ ratios due to the finite minimum conductance at zero voltage. By adding oxygen groups to the sheet surface, an induced and controlled band gap can be introduced to increase the FET performance at low field emission thresholds [93].

rGO networks could also be used as molecular sensors due to the change of electric conductance after adsorption of a target molecule. Some molecules have been found to bind onto the graphitic $sp^2$ domains using weak interactions or bind onto the vacancies and oxygen functional groups [39]. With the first mechanism of binding, molecules can be recovered using thermal energy, but the latter interactions are strong, making molecules non-recoverable after detection. Some of the applications in the optics sector include surface-enhanced Raman scattering (SERS) [94], fluorescence quenching [95], and modulation of laser intensity [96]. These applications exploit the fluorescence and high transmittance of GO. Combining both

optical and electronic properties, photovoltaic and LED devices are an appealing use for transparent conducting GO/rGO composites [79,97].

### *2.4.2 Energy Conversion and Storage*

Renewable energy technologies are in high demand for the purpose of reducing carbon emissions produced from current fuel sources. Applications as catalysts or mediators in hydrogen generation are one of the potential uses in alternative renewable energy sources. Functionalized graphene-based materials have the advantage of having a very large surface area and many active sites available for catalysis. Other applications include enhancements in batteries and supercapacitors due to the nanomaterial's fast charging speed and high charge storage, characteristics that are stable over a large number of cycles [4].

GO has some interesting characteristics that make it a promising photocatalyst for $H_2$ evolution from water splitting. GO exhibits p-type conductivity because of oxygen's high electronegativity compared to carbon. The oxygen groups in GO cause the valence band to originate from the 2p orbital of oxygen rather than the $\pi$ orbital of graphene, leading to a larger band gap [98]. The GO conduction band is mostly attributed to the anti-bonding $\pi^*$ orbital, which has a higher energy level than that needed for $H_2$ generation [99–102]. One study reported the use of GO/rGO composites to modify $TiO_2$, a popular photocatalyst with high activity, chemical inertness, low cost and nontoxicity [103]. A drawback with using $TiO_2$ alone is the backward reactions restricting hydrogen production. Chemically bonded $TiO_2$-GO showed improvements in the photocatalytic activity for $H_2$ production as well as degradation of some pollutants. Other composites of GO with metal oxides, metal sulfides, metallates and even other carbon nanomaterials (CNTs) have also shown improvements in their photocatalytic activity. GO-based materials also can be used as co-catalysts replacing noble metals (Pt, Pd Ru, Ag, etc.)

loaded on semiconductors to promote water splitting [103]. Noble metals are expensive and harmful to the environment; thus GO-semiconductor hybrids can be a good alternative for promoting hydrogen evolution [104].

Additionally, physical hydrogen storage is possible for few-layered GO materials. $H_2$ has shown to interact between layers of graphene-based materials. These interactions are highly dependent on the interlayer spacing. A study done varying the interlayer size of GO and rGO materials revealed that an optimal interlayer size of 6.3-6.7Å was ideal for maximum $H_2$ storage capacity (4.8-5.0 wt%) [105,106]. The functional groups present also improve the $H_2$ binding energy compared to pristine graphene in which interactions are too weak [4]. Composite materials with GO/rGO are also a good alternative for $H_2$ storage by allowing adjustments of the interlayer space or increasing the effective active sites available [107].

GO and rGO sheets have also shown potential applications in supercapacitor materials. These nanomaterials have proven to exhibit pseudocapacitive characteristics even though in principle they exhibit poor electrical conductivity. Some multilayer GO nanosheets have exhibited high capacitance retention over time (10,000 cycles) [108]. This pseudocapacitance behavior suggests the functional groups can serve as separators in supercapacitors composed of thin film electrodes [109]. The functional groups induce large pseudocapacitance, less aggregation and good wetting properties [110]. Doping the GO/rGO structure with boron or nitrogen can also enhance supercapacitor performance by increasing conductivity. Other popular applications in energy storage for GO/rGO materials are the possible enhancement of electrodes in batteries. Cathode and anode GO based composite materials have shown superior performance in batteries including lithium-ion, lithium-sulfur, and lithium-air [111–113].

### *2.4.3 Contaminant detection, removal, and conversion*

Environmental applications for the adsorption, detection and/or conversion of contaminants including greenhouse gases, heavy metal ions, and organic species are possible due the unique surface chemistry of GO materials. Studies have shown few-layered GO has readily adsorbed $CO_2$ in water at low pressure (~5 bar) and $N_2$, $CH_4$, $H_2$ at higher pressure (~20 bar) [114]. Composites of polymer-decorated GO have shown positive effects by increasing the available surface area and improving the cycle stability for $CO_2$ capture [115–117]. Other contaminants capable of being removed by GO and its composites include ammonia [118], acetone [119], formaldehyde [120], $H_2S$ [121], $SO_2$ [122], CO [123], and $NO_2$ [124]. GO has shown high affinity for heavy metal ions in wastewater, which are harmful to humans, animals and plants [125]. Highly toxic metals such as Cr(VI) [125], Pb(II) [126], and $Hg^{2+}$ [127] have shown an increase in adsorption in GO/rGO decorated polymers and composites. Other research has shown GO itself is an excellent adsorbent of organic dye pollutants such as methylene blue [128].

Gas conversion has also been enhanced in GO decorated composite catalysts and photocatalysts. Some studies have shown these composites capable of reducing $CO_2$ into valuable chemicals ($CH_4$,$CH_3OH$, $C_2H_5OH$, HCOOH and $CH_3COOH$) [129–132]. Apart from pollutant removal via adsorption and ion selectivity penetration, GO-based materials are also capable of converting pollutants into less toxic forms, as seen with Cr(IV) conversion into Cr (III) [125]. Conversion of other pollutants present in wastewater through catalytic or photocatalytic reduction methods using GO composites has been explored as a substitute for expensive materials (i.e. Pt). Studies have shown catalytic activity in GO or GO-based composites for the reduction of $SO_2$ to $SO_3$ [133], ammonia into primary amides [134] and

nitrobenzene into N-phenylhydroxylamine and aniline[135], amongst others. Organic dye decomposition studies using rGO have shown effective catalytic degradation of Orange II [136] and methylene blue [137].

### *2.4.4 Biotechnologies*

Applications for biofunctionalization, biosensing, enzyme inhibition and drug delivery are also popular fields of study due to the many active sites available on the GO surface. Due to its specific elemental composition, GO is a biocompatible material that can interact with other biomolecules via electrostatic interactions, π-π stacking, and hydrogen bonding [4]. GO can potentially interact with proteins ,such as horseradish peroxidase and glucose oxidase, for potential applications in biosensing [138,139]. The GO surface also has been functionalized with other molecules including hydrogen peroxide ($H_2O_2$), β-nicotinamide adenine dinucleotide (NADH), dopamine, peptides, and cellulose for enhanced biosensor and bioelectrode applications [140,141]. Some studies have reported affinity between single-stranded DNA (ssDNA) and GO due to π- π stacking between nucleotide bases and the graphene-like basal plane. Hydrogen bonding is also possible between the ssDNA and some of the oxygen containing groups in GO [142]. These complexes can have many applications including detection of free nucleotide bases.

Some other bioapplications found for GO include the use of its intrinsic fluorescence in the NIR to UV regions to use as a donor (or acceptor) in the process of fluorescence resonance energy transfer (FRET) for the detection of rotavirus [143] or DNA [144]. Detection of these molecules can be done via photoluminescence quenching. Antibody modified GO sheets for the detection of proteins have also shown some promising advances using inorganic luminescent quantum dots [145]. Other molecules being studied for detection with GO materials include

metals and proteinases [4]. Electrochemical biosensors using rGO are promising since they can mimic the properties of graphene in further reduced materials. Not only can the holes in rGO facilitate the transport of electrolyte ions, but also the functional groups can accelerate redox reactions. This is particularly useful in the electron transfer by proteins or enzymes since rGO materials are biocompatible. These rGO nanocomposites have also shown an increase in stability and response time [146].

## 2.5 Challenges and limitations

Development of bulk graphene production technologies is still ongoing. Substantial resources are being applied to find techniques to produce the most pure material at high rates and at low cost. Before the isolation of graphene in 2004, 2D crystals were thought to be impossible, as they were thought to be thermodynamically unstable. Because of the wrinkled structure of graphene, isolation was made possible using mechanical peeling ("scotch tape method"), which allowed the production of stable sheets [1]. Since this discovery, a number of patents and papers have been published regarding production of this wonder material using various techniques.

Unfortunately, the existing production techniques for graphene require high-energy input, toxic chemicals, or are slow and viable only at a laboratory scale for research purposes. The most promising method of graphene bulk production available has been reduction from GO. Most chemical GO production techniques are fast and able to produce large quantities. However, these techniques have the drawback of producing materials with large defects and holes that cannot completely recover the $sp^2$ lattice after reduction. Toxic byproducts and reagents need to be completely removed, which can also be challenging depending on the production method. Electrochemical production methods have shown to be less harsh on the GO surface, effectively producing sheets with fewer defects avoiding the use of dangerous reductants and disposal of by-

products. However, required conditions are non-ideal as the best reported electrochemical methods still need relatively high voltages, expensive electrodes, or acidic electrolyte solutions. Environmentally friendly production approaches that also further increase production efficiency, decrease the amount of energy input, and decrease reagent cost are desired. For these reasons, the use of MES is an appealing approach to biocatalyze these electrochemical reactions with simpler electrolyte solutions and with readily available, low-cost electrodes. MES methods have shown improvements in other fields and can potentially improve GO production by increasing yields and decreasing cost. Specific features of the BEGO method and the use of MES is introduced in the next section.

### 2.6 Bioelectrochemical production of GO (BEGO)

Bioelectrochemical systems (BES) have become desirable in the past decades due to the use of microorganisms as inexpensive biocatalysts. Microorganisms are capable of driving redox reactions within an electric field, resulting in substantially higher reaction rates [147,148]. These microorganisms are capable of oxidizing (or reducing) organic or inorganic substrates to produce energy in the form of current or hydrogen gas [147]. They are known to transfer electrons via direct or indirect mechanisms through electron shuttles, which can be supplied exogenously or endogenously as well as by conduction [149]. Interactions at the electrode surface of typically immobilized microorganisms have many advantages due to the self-regeneration, substrate flexibility and higher versatility compared to isolated enzymes, organelles and other catalysts. They have shown to decrease overpotentials. Some microorganisms have been found to be capable of oxidizing graphite to GO, by catalyzing the required reaction thus lowering the chemical and energy requirements of chemical methods [150,151]; however, in solution the process is too slow to be practical. Abiotic electrochemical methods also have been studied for

producing GO from graphite [54,152,153], but these methods still require chemical consumption, produce potential toxic by-products, and are limited to either the starting material being annealed or a deposited form of graphite. Although both microbial and electrochemical methods have limitations, by combining both processes a new method of producing GO avoids the use of harsh chemicals, high energy consumption, or toxic by-products resulting in improved performance of bioreactors and higher yields [19].

BEGO Advanced Materials, Inc. (BEGO, Hong Kong) has developed a bioelectrochemical method to produce GO from carbonaceous material known as the "BEGO process." Using MES to produce GO is an attractive technology as MES operate under mild conditions (less hazardous chemistry) and with low energy input, making BEGO a green approach [154]. A recent MES study showed accelerated production of GO and $H_2$ gas under microaerobic conditions where a biofilm was present on the anode compared to an abiotic counterpart [19]. Using graphite as an electron donor, some species of *Pseudomonas*, particularly *P. syringae*, were identified to be the most prominent microbial genotype in the graphite biofilm. The biofilm was identified to be a key factor driving the reaction as the current density of the system was higher (1.24 A/m2) than for the sterile reactor (0.01 A/m2) under the same conditions (cathode poised at -0.6 V vs. SHE). Monitoring of BEGO production was done by conducting current density measurements, dissolved chemical oxygen demand (dCOD) analysis, final anode degradation mass difference, and gas production of $CO_2$ and $H_2$.

The BEGO process is a new technology and thus knowledge gaps exist regarding the operation, design, purification, and quantification of the final material. Further research of the BEGO process could increase production rates of GO, reduce operation time and allow for a better understanding of the capabilities of this unique material. Advancing knowledge of the

advantages of the process is necessary to develop competitive methods compared with existing technologies. Work completed to date suggests that the BEGO process is a promising technology, with future optimization necessary to supply industrial and commercial markets. During the study performed at CSU, specifics of the BEGO technology are explored including developing an estimate of GO production rates, further characterization and purification of the final material, and understanding the role of themicrobes present using different inoculum sources.

# 3. MATERIALS AND METHODS

For this study, the team at CSU focused on extending knowledge of BEGO production under different conditions to make improvements to the existing methods. Measuring rates of production, physical/chemical properties, and comparing inocula were investigated to develop a better understanding of the mechanism of production and quality of the product. Three objectives, indicated in section1.2, will help BEGO Advanced Materials Inc. target the most appropriate markets, depending on the characteristics of the nanomaterial. Two designs at different scales were chosen to run under various conditions to understand scalability. The first sets of experiments were the small-scale reactors (SSR); the SSR trial was used to compare inoculum at a small scale to analyze the microbial community impacts. Controls included reactors inoculated with the same sources, but with no voltage applied to explore the capabilities of the microorganisms alone. The second sets of reactors were the large-scale reactors (LSR) used mainly to produce larger quantities of the BEGO for characterization, but also to explore a different reactor geometry. Abiotic reactors (LSRA) were built as the controls and connected to a power supply to compare production rates with the biotic reactors (LSRB). Sequencing of the 16S rRNA gene was done on the bioreactors inoculated with different microbial sources. Variations in inoculum sources, voltage applied, electrode choice, and purification techniques were some of the operating variables examined throughout the experiments to evaluate their impact on the BEGO production.

Two trials of each configuration were performed, with successive improvements in reactor design. The first trial of the SSR reactors (SSR1) was used to adjust the voltage, control the electrochemistry, and develop methods for quantification of the BEGO. The second trial

(SSR2) was used to further understand the microbial contribution to GO production with more replicates. In comparison, two trials of the LSR reactors were also performed with the goal of improving conditions in the first trial (LSR1) and for high mass production on the second trial (LSR2). Analysis on reduction technologies was done by our collaborators using microwaving protocols but is not discussed in detail here. Production methods were examined under the different parameters chosen using MATLAB, and RStudio analyzing with the Ancova, Tukey, and t test methods for statistical comparison.

### 3.1 Reactor set up

For the SSR configuration, twelve 500-mL vacuum flasks with rubber stopper caps were used for the reactor body. Three holes were drilled in the stoppers to introduce insulated copper wires to attach the electrodes. For the cathode, a 5-cm by 10-cm carbon cloth was attached to an alligator clip bound to one of the copper wires. A graphite anode rod (10-cm length and 0.5-cm diameter) was attached to the other copper wire on the opposite side of the stopper. On day 8 of the first trial, three more graphite rods were introduced through the same hole, so that anodes could later be sacrificed for biofilm analysis. The middle hole was used to attach an Ag/AgCl reference electrode (RE) purchased from BAsi Inc (West Lafayette, IN, USA), as these trials were built as three-electrode systems. A salt bridge was later introduced (days 204 and 210) to replace the RE hole and was made out of 2% agar and 0.1M NaCl inside of a Teflon tube. Conductive glue and heat shrink were used to secure the connections to the wires. A liter gas bag purchased from EnviroSupply (Irvine, CA, USA) was attached on the side port of each vacuum flask using vinyl tubing and a tubing adapter. All the pieces were secured using a glue gun, silicon glue, and epoxy glue as necessary (Figure 2).

The LSR reactors were 8 liters each. The bodies of the LSR were made out of white polyvinyl chloride (PVC) pipes of ~62-cm height and 6-inch diameter. DMV female adapters were placed on the top and bottom of the reactors for sealing. Two 3.5-cm diameter holes were drilled into the middle section (~26-cm from the bottom) and bottom section (~6-cm from the bottom) of the reactors to attach PVC valves for sample collection. The cathodes used were carbon cloth (LSR1) or a 316 stainless steel mesh (LSR2) glued to cover the inner wall of the PVC. A bundle of 29 graphite rods (height of ~50cm) was hung in the center of the PVC pipe (see Figure 7); rods were the same length as those used for the SSR but thicker (1-cm of diameter). Rubber bands were used to secure the rods into bundles. Titanium wires (gauge 22) were attached to anodes and to the outside of the reactor through holes drilled on top (~52-cm from the bottom) of the PVC body. Connections were attached to a power supply using insulated copper wires and alligator clips. A 5-liter Tedlar bag was attached to the top of each reactor for gas production monitoring. Sealing was done using plumbing tape, PVC glue, silicon glue, and epoxy glue as necessary (Figure 3).

**Figure 2:** SSR setup

Figure 3: LSR setup

### 3.2 Inoculation and media preparation

Three microbial sources were compared during the first trials. Sludge samples were collected from the anaerobic digesters at the Drake Water Reclamation facility (Fort Collins, CO) and the New Belgium Brewery (Fort Collins, CO). A third sample was taken from a natural pond in the rural areas outside of town (Fort Collins, CO). All three samples were collected during the fall and stored at 4ºC for 2-7 days until inoculation. The inoculation consisted of 10.0-12.5% of the total reactor aqueous volume. The remainder of the reactor was filled with a media (see Table A1 in Appendix A for media recipe) as previously described by Lu et al. [19], made with previously autoclaved deionized water. Microbial media included trace minerals and vitamins [155]. The media was flushed with either $N_2$ or $CO_2$ depending on the reactor configuration to make it anaerobic.

During the first SSR trial (SSR1), duplicates of the three different inocula were used. Each reactor had a total volume of 400 mL (40 mL inoculum and 360 mL media) with their respective controls (12 reactors total). During the second trial (SSR2), only the Drake and New

Belgium inocula were used in triplicates without controls for a total of 500 mL (50 mL inoculum and 450 mL media). For the SSR2 trial, half of the inoculation was done with enriched samples from the SSR1 trials (25 mL) and the other half (25 mL) was fresh inoculum from the original source described above. Reactors were flushed for 35 minutes with $N_2$ before sealing inside of an anaerobic chamber.

The LSR configurations were inoculated using only the New Belgium sludge; the total reactor volume was 8 liters (1 L inoculum and 7 L media). Four reactors were built for the first trial (LSR1): three biotic and one abiotic that did not contain inoculum. For the second trial (LSR2), ten biotic reactors were built and run until no more GO production was observed. Four out of the ten reactors were sterilized using bleach to create the abiotic reactors. Due to the large size of the reactors, 90-minute flushes with $CO_2$ were performed through a vinyl tube submerged through the Tedlar bag port. Sampling was done through the middle PVC valve and reactors were kept sealed until the end of the run. Reactor naming for each trial, including control conditions, are shown in Table 1.

**Table 1:** Reactor ID key

| **Small-scale reactor (SSR)** | | | **Large-scale reactor (LSR)** | | | |
|---|---|---|---|---|---|---|
| **Trial 1 (SSR1)** | | **Trial 2 (SSR2)** | **Trial 1 (LSR1)** | | **Trial 2 (LSR2)** | |
| D1 | C_D1 | D1 | R1 | AB | R1 | AB1 |
| D2 | C_D2 | D2 | R2 | | R2 | AB2 |
| P1 | C_P1 | D3 | R3 | | R3 | AB3 |
| P2 | C_P2 | N1 | | | R4 | AB4 |
| N1 | C_N1 | N2 | | | R5 | |
| N2 | C_N2 | N3 | | | R6 | |
| | | | | | R7 | |
| | | | | | R8 | |
| | | | | | R9 | |
| | | | | | R10 | |
| D - Inoculum from Drake Water Reclamation Facility anaerobic digester | | | | | | |
| P - Inoculum from goose pond sediments | | | | | | |
| N - Inoculum from New Belgium Brewing Co. anaerobic digester | | | | | | |
| C - Control unconnected reactors | | | | | | |
| R – Large-scale reactor inoculated with New Belgium Brewing Co. anaerobic digester | | | | | | |
| AB – Large-scale abiotic reactors (connected) | | | | | | |

### 3.3 Operating conditions

Initially, the SSR1 reactors were connected to two 4-channel eDAQ quadstats (Colorado Springs, CO) to control the reactor potentials, but were later switched to an eight-channel potentiostat (CHI 1030C) from CH instruments Inc. (Bee Cave, TX) on day 113. The switch was done to achieve better control of set potential and to allow measurement of higher currents (see Appendix A, Figure A2-A3). Amperometric curves were recorded throughout the entire reactor lifetime, resetting every two days to avoid equipment overheating. The reactors were originally set at -0.8V (vs. Ag/AgCl) at the cathode but were later switched to 0.8V (vs. Ag/AgCl) at the anode on day 22 to control the voltage on the working electrode. On day 182, voltage was increased up to a final value of 1.4V (vs. Ag/AgCl) during a period of 30 days to promote GO production as shown in Figure 3. Reactors were covered with foil to avoid algae growth. Every 1-2 weeks, reactors were taken into the anaerobic chamber for sampling, feeding, and refilling after sampling using the aforementioned media to keep the volume constant. About 5 to 8 mL were taken at each sampling event from each reactor and stored in the fridge for future analysis of BEGO production and characterization. The SSR1 trial ran for a total of 359 days from the moment it was connected to the first potentiostat. The SSR2 trial ran using the octastat only at the highest voltage tested with the SSR1 run (1.4 V vs Ag/AgCl), and salt bridges initially in place. These reactors were built with a sampling port comprised of vinyl tube with a 3-way stopcock so that sampling could be done on the bench instead of the anaerobic chamber. The SSR2 reactors ran for a total of 224 days.

The LSR1 reactors were originally poised at 8V, but later voltage was lowered down to 3V as shown in Figure A6 (Appendix A), using a DC power source with multiple attachments

(Eventek KPS305D). The LSR2 trial was poised only at 3V using individual power adapters from RadioShack (#2731121, Fort Worth, TX). Voltage and current were monitored every 1-2 days using a multimeter by Mastech group LLC (MASTECH MS8261, Brea, CA). The LSR1 trial had to be restarted multiple times due to leaks that caused delays in GO production due to dilutions with new media, and reactors being out of commission (data nor reported). The LSR2 reactors underwent a leak test before inoculation and media introduction thus allowing constant volumes throughout the experiment. The 10 biotic reactors on this second trial ran for a period of 105 days and 4 abiotic reactors ran for 108 days until disconnected. The bodies of the first three reactors of the LSR2 trial (R1-R3) were recycled from trial 1 with the old cathodes which caused variations in production rates; thus data for those were not reported. These three reactors (R1-R3) and the AB reactor from the LSR1 trial were bleached and cathode replaced for a 316 stainless steel mesh to create the abiotic reactors for the LSR2 trial.

### 3.4 BEGO purification techniques

Purification techniques were necessary to minimize BEGO contamination with ions, organics, and large suspended solids. Various protocols involving centrifugation and filtration were tested to remove suspended solids before BEGO quantification and characterization. Liquid samples (5-10 mL) collected from the reactors were centrifuged in 15-mL falcon tubes at velocities of 3,000-10,000 RPM (revolutions per minute) for 10, 20 or 30 minutes to optimize solids removal. During different centrifugation trials, UV-Vis was used to test the supernatant of each run. After 8,000 RPM (7441.4 x g) for 15 minutes, there was no obvious change in the UV-Vis absorbance. DNA extraction kits for centrifuging cells use a protocol at 10,000 x g to collect cells at the bottom of the tube (pellet). Thus, 15 minutes at 10,000 x g was chosen as the best centrifugation protocol to ensure the biomass was removed. Centrifugation was done in a Sorvall

Legend XTR (Thermo Fisher Scientific, Waltham, MA) centrifuge with a F15S-8x50C rotor at room temperature. The centrifugation technique was used for liquid sample analysis including UV-Vis, dCOD, and BEGO deposition on substrates for microscopy analysis.

Filtration protocols were set up by Membrane Development Specialists (MDS, Escondido, CA) and then replicated at CSU. For the membrane selection process, see the BEGO characterization section 4.2. Collection of BEGO was performed using a two-step protocol. Liquid samples were processed at CSU using a vacuum bench filtration system with 47 mm filter holders and max processing volume of 250-mL. Large solids and sediments were removed using a 5-µm woven polyester filter cloth (coarse filter) in a pre-filtration step. A 0.5-µm hydrophilic Teflon membrane (BEGO collection membrane) was then used to collect the BEGO flakes. This method was used on the SSR1 reactors after they were terminated to process the total volume and estimate yields. The bottom 20% of the reactor volume needed dilutions prior to filtration due to sedimentation of the inoculum solids or aggregates that caused rapid clogging of the coarse filters. The upper liquid in the reactors (upper 80% volume) had almost no large solids and passed through the coarse filter with minor to no clogging. The BEGO solids on the Teflon membrane were scraped off using a spatula and collected for analysis with FT-IR and TGA. During the SSR2 trial, the filtration protocol was also used for UV-Vis quantification using the permeate of the coarse filtration step during the first 100 days (see Figure B8-B9). Lyophilization protocols were also considered for BEGO collection, but this method was discarded due to high concentration of salts interfering with downstream analysis.

### 3.5 Detection and characterization

For BEGO quantification, UV-Vis, dCOD, and total organic carbon (TOC) were used to track production over time. Material balance techniques using graphite mass losses from the start

to the end of reactor operation were used as an additional means of estimating BEGO production rates. The BEGO collection filter was also weighed before and after filtration to estimate yields. Dilutions of purchased GO samples of known concentration were done in deionized (DI) water and used in the aforementioned methods (UV-Vis, dCOD, and TOC) to create calibration curves for quantification of unknowns. UV-Vis spectroscopy was done by scanning spectra between 210nm and 800nm in a UV-Cuvette micro (12.5x12.5x45 mm) by BRAND (Wertheim, Baden-Württemberg, Germany) using an Agilent 8453 UV-Visible spectrophotometer (Santa Clara, CA). Concentrations of BEGO were measured based on a peak at wavelength 229 nm ($\pi \rightarrow \pi^*$ transitions of aromatic C-C) and a shoulder at 300 nm ($n \rightarrow \pi^*$ transitions of the carbonyl groups C=O) [19]. Sample dilutions were prepared to have absorbance readings below 2 absorbance units (AU) to be within the accurate linear range of the instrument. Dilutions were done using media if dilutions were lower than 1:10, or DI water if higher. dCOD was measured using high range COD digestion vials #2125915 by HACH (Loveland, CO) on a DR 3900 spectrometer, also by HACH. For this assay, centrifuged samples were also filtered prior detection using a 0.2-µm membrane syringe filter and diluted 1:3 in DI water to preserve sample volume. In the Lu et al. study [19], 0.1-µm filters were used to collect the BEGO therefore 0.2-µm should be above the collection range. This filtering step was necessary to remove microbial contributions to the COD that could affect the detected values. Later data showed that 0.2-µm was a small enough pore size to capture the larger BEGO particles thus resulting in an underestimate of the BEGO produced (see section 4.1.1.1). For TOC analysis, the centrifuged samples were diluted 1:20 in DI water for a total volume of 20 mL in autosampler glass vials. TOC was measured using a TOC-VCSH analyzer by Shimadzu (Nakagyo, Kyoto, Japan). Calibration standards were prepared from purchased GO produced using the Hummers' method

purchased from Sigma Aldrich (2 mg/mL, St. Louis, MO) and Graphenea (4 mg/mL, Donostia, Gipuzkoa, Spain). For quantification using mass balance techniques, the change in mass was divided by the reactor volume and number of days during the BEGO production phase (see section on analysis and on quantification methods 4.1.1 for description).

For characterization analysis, the XPS used was a PE-5800 X-ray (Eden Prairie, MN) by depositing material from centrifuged liquid samples on a silica substrate previously sputtered with gold (2 nm thick) and left to air dry. FT-IR was done in a Nicolet iS-50 by Thermo Scientific (Waltham, MA) on solid samples collected from the filtering protocol solids to obtain transmittance spectra. Raman was analyzed with an Olympus IX73 microscope (Center Valley, PA) with a 532 nm Ondax THz Raman system (Monrovia, CA) and Horiba iHR550 spectrometer (Piscataway, NJ) using a 10x objective and 8mW power. This analysis was done on centrifuged liquid drops deposited on glass slides and left to air dry. TEM was done on a JEOL JEM-2100F (St-Hubert, QC, Canada) performed first on the centrifuged samples, and later using solids from the BEGO filtering protocol in DI water; this was done due to surfactant-like molecules, seen in the TEM images in the former purification method that needed to be removed for proper imaging. These samples were deposited on a lacey carbon substrate. The samples for AFM (Bruker BioScope Resolve, Billerica, MA) analysis were purified using the centrifugation protocol and deposited on mica substrates at a concentrations near 1 ppm. Imaging was done using the SCANASYST-AIR probe at a scan rate of 1 Hz. TGA (TA TGA Q500, New Castle, DE) was done on BEGO solids collected from the filtering protocol under nitrogen gas, to monitor mass losses. ICP-MS (Perkin Elmer NexION350D, Waltham, MA) was performed on centrifuged liquid samples for analysis on ion contaminants. Finally, gas chromatography (GC) on the gas bag contents was performed using a HP 6890 GC (Hewlett-Packard, Palo Alto, CA)

equipped with a thermal conductivity detector (TCD) and a RT-Q-Bond column (Restek Corporation, Bellefonte, PA). NMR was also performed but not repeated due to low detection limits and expensive equipment usage fees.

### 3.6 Sequencing

The SSR1 reactors were opened for DNA and RNA extractions on day 32 and days 231/233 in an anaerobic chamber. 25 mL were collected from the bulk media using sterile 50-mL falcon tubes for DNA, and 50-mL autoclaved Nalgene bottles for RNA both placed on ice. Bulk media samples were spun down at 4°C for 25 minutes at 10,000 x g to collect a pellet, discarding the supernatant. Biofilm samples were collected from the graphite rods using two different protocols. Scraping of the biofilm was attempted using sterile scoops but due to time constraints and low yield, rods were instead cut off the wire and placed inside of sterile 15-mL falcon tubes. The sacrificed rods were submerged in media for DNA processing, or in the preservation solution LifeGuard by MoBio (Carlsbad, CA) for RNA. The sacrificed rods were replaced to preserve the electrochemical conditions, and for the second round of extractions, only the rods present in the reactors since startup were sampled. The 15-mL falcon tubes with the rods were briefly vortexed to remove biofilm biomass and centrifuged at the previously mentioned parameters to collect a pellet. Supernatant was discarded.

To isolate the nucleic acids, the DNA isolation kit (PowerSoil) purchased from MoBio (Carlsbad, CA) and the RNA isolation kit (RiboPure, bacteria) purchased from Ambion (Foster City, CA) were used on day 32. Later extractions (days 231/233) were done with Qiagen (Valencia, CA) kits using the PowerSoil isolation for DNA Samples and the PowerBiofilm isolation for RNA. Co-extracted DNA was removed from the RNA samples using the Turbo DNA-free kit from Ambion (Foster City, CA). Reverse transcription (RT) was done on the RNA

samples using the Superscript IV RT protocol from Invitrogen (Carlsbad, CA) to obtain complementary DNA (cDNA). Nucleic acid concentrations and purity (data not shown) were measured using a Take3 plate on a Synergy HT spectrophotometer by BioTek (Winooski, VT), or a Nanodrop 2000c by Thermo Scientific (Waltham, MA). Samples were sent out for sequencing at RTL Genomics (Lubbock, TX) or run at the CSU sequencing core (Fort Collins, CO).

# 4. RESULTS AND DISCUSSION

To advance understanding of the BEGO production process, three main objectives were selected as indicated in Chapter 1:

1. Measure BEGO production rates using multiple techniques and investigate the impact of selected operating parameters on rates,
2. Identify key physical and chemical properties of the BEGO produced,
3. Compare different inocula and identify microorganisms present both in the bulk solution and the graphite rod biofilm.

At the beginning of this project, no methods were available to quantify the rate of BEGO production over time, other than estimates measuring dCOD changes and electron balance [19]. dCOD is not specific to BEGO making it an unreliable parameter for predicting BEGO concentrations. Our goal was to develop a quantification technique specific to BEGO and apply this technique to measure rate constants as a function of other operating parameters. As part of the technique development, BEGO purification methods were developed and refined to remove contaminants to avoid quantifying them, and thus potentially over-predicting BEGO production [54]. The purified BEGO was then analyzed using different characterization techniques to understand the physical and chemical properties of the product. Understanding the nature of the final product provides insight into the best applications and reduction protocols (i.e., to rGO), if necessary. Finally, a detailed analysis of microbial communities was done on the bulk solution and on the rod biofilm for different reactor configurations at various time points. Microbial community structure was analyzed via 16S rRNA gene amplicon sequencing to identify the

microorganisms that were present and active, and provide information on their functional capabilities.

This chapter is divided into three main sections. The first section (4.1) focuses on experimenting with different quantitative techniques to determine rates and yields for BEGO production. Section 4.2 focuses on BEGO characterization via different microscopy and spectroscopy techniques to understand physical and chemical properties of the BEGO. For this analysis, purchased GO produced by Hummers' method and literature studies were used as standards for comparison. Analysis of purity, number of layers, dimensions, functional groups and oxidation degree is also presented in this section (and in Appendix E). Lastly, section 4.3 reports and discusses microbial community characterization results on DNA and RNA done on the bulk and rod biofilm of the SSR1 reactors and controls, at the beginning and the end of operation (data for LSR2 in Appendix F).

### 4.1 Measuring rates of production

BEGO production was monitored for the SSR trials using reactors were naming depending on the inoculum used as shown in Table 1 (see section 3.2), with their respective controls. The LSR trials were inoculated using only the New Belgium bacteria and were run in triplicate for Trial 1 with 1 control, and with 7 replicates and 4 controls in Trial 2 (R1-R2 excluded here). Note that the controls for the SSR and LSR trials are different, as the SSR "C" controls are not connected to a power supply but contain microbes, and the LSR "AB" controls are connected to a power supply but are sterile. In depth analysis focused mainly on the SSR1 and LSR2 trials. Results can be found for SSR2 and LSR1 in Appendices A and D but are discussed here only briefly.

### *4.1.1 Analysis of quantification methods*

Calculations of the production rates were constrained to the time period when production was observed (production phase). Most of the trials (except for the SSR1 and LSRA2) showed no delay and production was calculated from when reactors were first connected. Delay in the SSR1 was due to low voltage but delay in the LSRA2 trial was due to a lag period. The production period ended once no more increase in production was detected with the quantification methods used. Each trial had a different production period that was affected by changes in the parameters and the design. Production rates reported in this chapter were calculated by fitting concentration data and dividing by the production period time (in days) and reactor volume (in L). Information on production periods and rate constants calculated can be found in Figure 4, Figure 6, and Appendix D.

#### 4.1.1.1 The dCOD method

The first BEGO quantification method used dCOD measured over time, as previously done in Lu et al. [19]. Appendix D (Figure D1) shows the calculated BEGO concentrations based on dCOD plotted as a function of time. Production was measured from days 175 to 294 (119 days), due to improvements in parameters on previous days that were necessary to start production (see section 4.1.4 for more details). Rates reported for the Drake reactors (D) were of 3.4 and 19.9 mg/Lday, for the Pond reactors (P) rates were of 11.5 and 16.3 mg/Lday, and for one of the New Belgium (N) reactors the rate was 22.8 mg/Lday. Reactor N2 showed no BEGO production most likely due to a defective channel on the potentiostat and high salt content. The P reactors had the most consistent duplicates during the SSR1 trial. The dCOD method was found to be nonspecific to BEGO, as other organic molecules are detected. This includes organic acids (and other organic molecules in suspension) that are suspected to be produced as pH drop was

observed (Figure A4), and as suggested by Lu et al. This method can be useful for understanding trends in production behavior but is not a representative quantification technique of actual BEGO. However, due to the extra filtration step using a 0.2-μm filter, the detected concentrations were actually lower than expected most likely due to larger BEGO particles captured on the filter and not quantified in solution.

#### 4.1.1.2 The UV-Vis method

Due to the shortcomings of the previously used dCOD method, a UV-Vis method was developed as a cheaper and more accurate BEGO quantification technique. No kits or reagents were necessary, and quantification was more specific due to the use of selective absorbance peaks at 229 nm and 300 nm. Results are shown for SSR1 in Figure 4 including a summary table of the calculated rates for each reactor. Data were collected from day 175 to day 294 (119 days), same as with the dCOD method since data points were the same. It can be seen that the 229 nm method yields higher concentration than the 300 nm method (and higher than the dCOD). The characterization section 4.2.1 explains how the BEGO produced has lower carbonyl groups thus a relatively smaller shoulder at 300 nm than the purchased GO standards produced using Hummers' method (see Figure E1-E6 for comparison). This is an important characteristic of the BEGO as it appears to be a material with less carbonyl/carboxyl stable functional groups than the standard GO. This characteristic explains the lower detection at the 300 nm peak compared to the 229 nm. Due to the BEGO material being mostly carbon atoms arranged in a honeycomb structure, the 229 nm peak proved to be more reliable and was chosen as the most accurate quantification technique. Calculated rates of production for the D reactors were of 8.1 and 35.2 mg/Lday, for the P reactors rates were of 16.1 and 21.7 mg/Lday, and one value for the N

reactors was 52.8 mg/Lday. For the SSR1 trial, there was no statistical difference in rates between the three different inoculum tested.

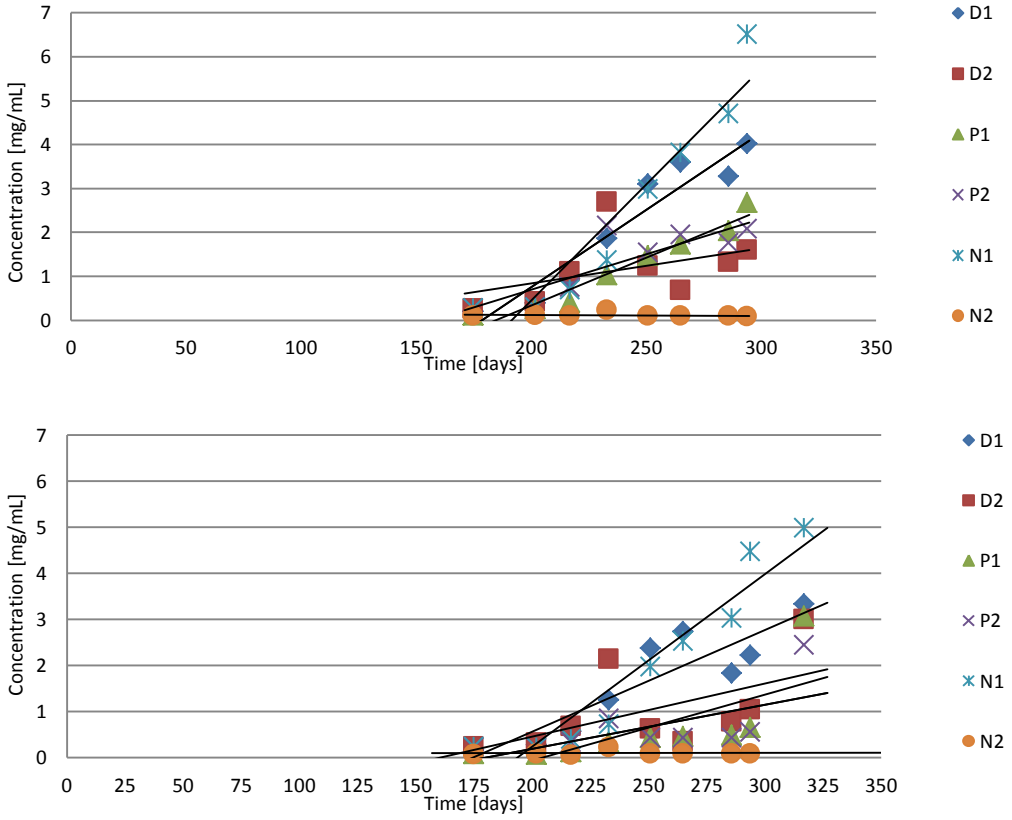


| Reactor | Production rate [mg/Lday] | | $R^2$ value | |
|---|---|---|---|---|
| | 229 | 300 | 229 | 300 |
| D1 | 35.2 | 22.1 | 0.917 | 0.815 |
| D2 | 8.1 | 11.5 | 0.188 | 0.323 |
| P1 | 21.7 | 14.3 | 0.995 | 0.503 |
| P2 | 16.1 | 9.6 | 0.714 | 0.408 |
| N1 | 52.8 | 37.5 | 0.898 | 0.905 |
| N2 | 0 | 0 | 0.023 | 0.002 |

**Figure 4:** Production rates for BEGO production phase using the UV-Vis method on the 229 peak (top) and the 300 peak (bottom) from day 175 to day 294 for the SSR1 reactors

During the SSR2 trial, two purification techniques were tested as explained in the methods section 3.4 for UV-Vis quantification. The centrifuged liquid as done in the other trials, and the permeate of the coarse filtration. Results are shown in Figure D2 (Appendix D) where

only the D and N inocula were tested in triplicates. For the 229 nm peak method, the D reactor rates ranged from 6.2 to 40.7 mg/Lday using the centrifugation protocol and from 9.7 to 39.7 mg/Lday using the two-step filtration. The N reactor rates ranged from 11.9 to 21 mg/Lday, and from 13.4 to 22.3 mg/Lday using the same methods, respectively. N3 showed no production as channel 6 of the potentiostat was shown to be malfunctioning (same with N2 in trial 1). Due to the close agreement from both methods (i.e., centrifugation and filtration), centrifugation was continued for the rest of the experiments for simplicity and time efficiency. A statistical analysis using the Ancova and Tukey method showed no significant difference between the inocula either on SSR1 or SSR2 trials with p values between 0.4 and 0. .8.

Although this technique seems to be the most specific and later results show it is consistent with the material balance method using the filtering protocol (see the yields section 4.1.1.4, Table 2) there are some limitations. For example, the GO calibration standards had a higher concentration of carbonyl groups than BEGO as discussed subsequently. As described in chapter 1 section 2.1.4 on material optics, having more functional groups usually means higher transmittance due to the disrupted $sp^2$ lattice. This could have an effect on the accuracy of our method. UV-Vis photon detection can also vary by the number of layers present in each flake due to scattering. Mourdikoudis et al. reported studies on nanomaterial characterization and detection that agree on the fact that one technology is not enough to accurately understand the properties of nanomaterials [156] . There are some issues and limitations for each analytical approach; thus, by combining them they can complement each other. Particle size distribution using SAXS (Small-angle X-ray scattering), and WAXS (Wide-angle X-ray scattering) with UV-Vis is one of the proposed methods of detection (i.e., SAXS/WAXS/UV-Vis), which could be explored in future studies with BEGO.

#### 4.1.1.3 Graphite rod mass balance method

Lastly, BEGO production was estimated by weighing the final graphite rods and subtracting the difference from new unused rods. The unused rods weighed around 5.470 g each (21.882 g for four rods in the system) whereas the final rods ranged from 1.957 g to 5.770 g per rod. Pictures of rods from each reactor next to two unused rod were visually compared (Figure 5). Some of the rods looked as if they had degraded extensively (e.g., P1) whereas some of the rods showed little to no degradation (e.g., D2). A calculated rate value based on mass loss for one of the other D reactors (D1) was 222.48 mg/Lday. D2 had no degradation thus production calculated was 0 mg/mLday. The P reactors had values of 147.48 mg/Lday for P1, and 257.77 mg/Lday for P2. One of the N reactors (N1) had a value of 212.39 mg/Lday and values for N2 were not reported. These values are an overestimate of the BEGO produced because this approach implies that 100% of the graphite was converted into BEGO. Due to the heterogeneity of the production process, it is possible that some of the graphite was converted into multi-layered graphene oxide (graphite oxide) and precipitate. It is also possible that some unreacted graphite may have simply been shaven or broken off the rods throughout the process. The anode in reactor D2 showed no weight loss, despite measureable BEGO in the aqueous reactor phase via the UV method. It is possible that a biofilm on the rod surface contributed to the weight of the rods after the trials thus no difference was detected between the unused and reacted rods. It is also possible that due to a magnetic stir bar introduced in the reactors for homogeneous sample collection, some rods might have broken off due to the excessive force. One thing to note by looking at trends of production is the fact that the P reactors yielded a higher production rate from this method compared to the other methods that favored N1 and D1. There are some explanations for these discrepancies discussed in sections 4.1.1.4 and 4.1.4 .

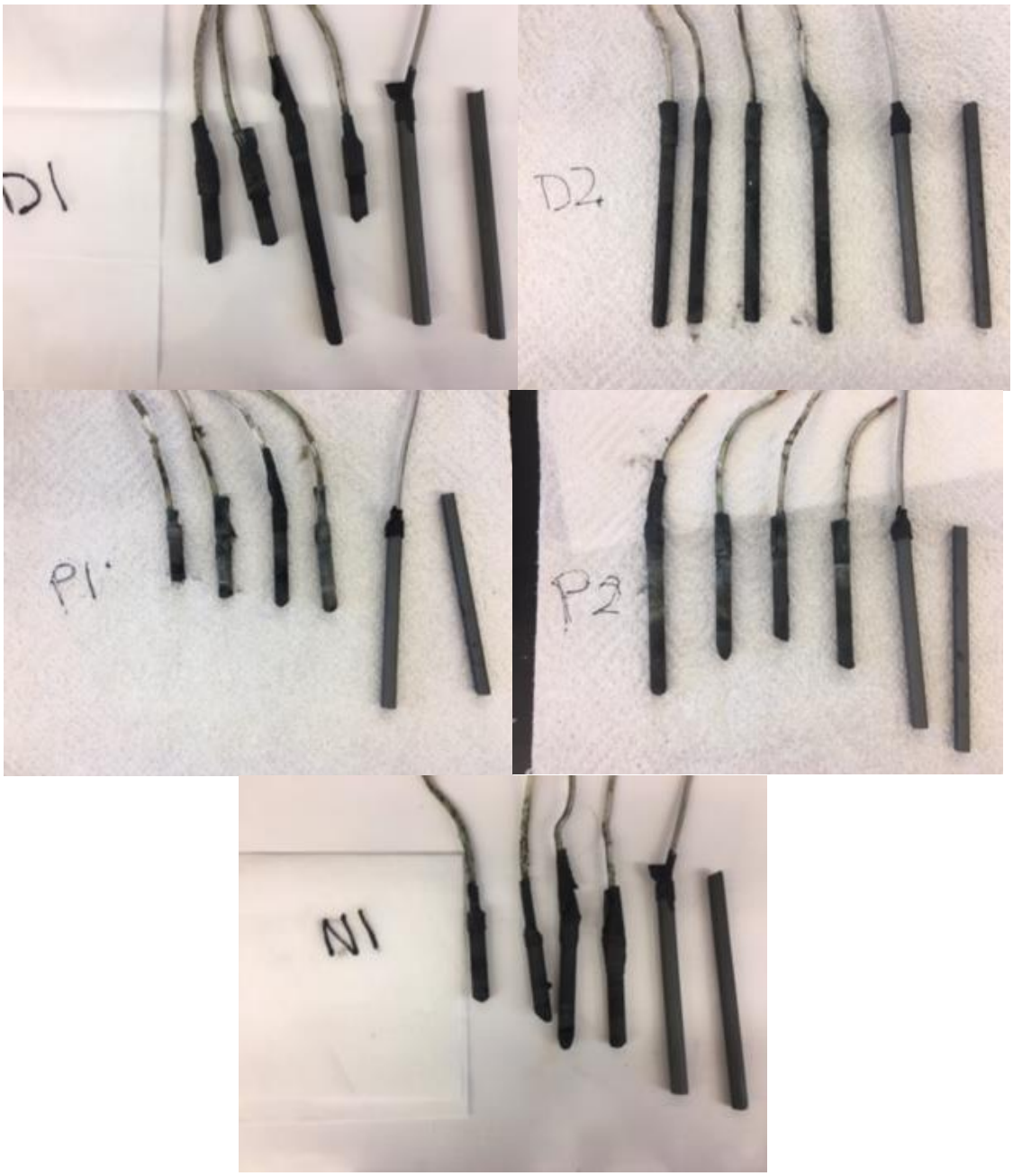


**Figure 5:** Rods from each one of the SSR1 reactors (except for N2) next to two unused rods in each picture.

#### 4.1.1.4 Yields

Table 2 Summarizes the mass of BEGO produced calculated in the SSR1 trial using different protocols for each reactor (excluding N2). The calculated mass loss method reported an

overestimate of BEGO produced as stated in the previous section 4.1.1.3. The UV-Vis method at 229 nm shown in column three is the calculated BEGO produced based on the day with the highest concentration detected. The third and fourth methods (columns 3 and 4 in Table 3) reported values measured at the end of the experiment, based on BEGO collected via the two-step filtration protocol. The third method (column 4) values were obtained from weighing the Teflon membrane (BEGO collection filter) and the fourth method (column 5) was estimated by measuring the UV-Vis at 229 nm of the permeate before and after the BEGO filtration. By subtracting the concentrations measured before and after filtration, we can estimate the mass of BEGO solids on the membrane found in the third method thus compare the 229 nm UV-Vis method with the filtering material balance method.

**Table 2:** Yield of BEGO produced using different methods of quantification

| BEGO yields [g] | | | | |
|---|---|---|---|---|
| Reactor ID | Rod mass losses | UV-Vis at 229 nm on day with highest production detected | Weighed Teflon membranes at the end of the experiment | Difference of permeate UV-Vis at 229 nm from the two-step filtration protocol at the end of the experiment |
| D1 | 19 | 1.608 | 0.1189 | 0.899 |
| D2 | 0* | 1.075 | 0.1018 | 0.198 |
| P1 | 12.27 | 1.073 | 0.0364 | 0* |
| P2 | 7.02 | 0.861 | 0.0473 | 0.037 |
| N1 | 10.11 | 2.606 | 0.1058 | 0.113 |

*In two cases calculated yields were negative, so their yields were reported as zero.

For most of the techniques used (except rod mass losses), the D1 and N1 reactors showed consistently higher yield than the P1, P2, and D2 reactors. The rod mass losses method produced calculated yields about one order of magnitude higher than the other methods. Although the P reactors showed the largest yield (for P1) using the mass losses method (see Figure 5 for visual comparison), analysis on the coarse filter membranes showed that the P reactors also contained

the largest amount of large solids (see Figure B5, in Appendix B). The coarse filter had a large pore size (5 µm), such that collected solids are mostly aggregates, sediments from the sludge, and chunks of crumbled graphite and not BEGO. Due to stir bars being introduced into the reactors for homogenization for sampling, it is possible that with high speed they could have broken the graphite core. These two reactors also showed less color change in the suspended liquid (Figure B4) at the end of the experiment compared to the other working reactors (D1, D2 and N1). Due to low rates in the P reactors and possible aggregation, this inoculum was chosen not to be used during the SSR2 trial.

The last two methods for yield calculations were very close in agreement with each other (mainly for the P and N reactors), suggesting the UV-Vis 229 nm method is reliable. These two methods yielded low material most likely due to the Teflon membranes having a large pore size (0.5-µm), that does not capture all of the BEGO (see Appendix B Figure B6-B7). This was visible in the color of the permeate of both filtrations (see Figure B7). A dark color in the permeate of the BEGO filtration indicated not all of the material was captured in the membrane. Therefore, these two yield measurements are an underestimate of the BEGO produced. Due to the clogging of the coarse membranes, there is also a chance some of the BEGO did not flow through and stuck to the coarse membrane thus adding to the underestimate of the two-filtration method. The concept of the two filtration system is good but a better system and membrane are sizes are necessary to accurately quantify all of the BEGO.

Aggregation was also a possibility occurring in the reactors after the last increase in detection was perceived. Raw data (Figure B2) indicated that after some period of time (after day 294), detected concentrations started decreasing in all of the reactors. This trend was also visible in all of the other trials (SSR2, LSR1, and LSR2). If the BEGO produced started aggregating,

there is a possibility these aggregates sediment and were collected in the coarse filter (or centrifuge out) and were not detected. The nature of these aggregates if any is out of the scope of this thesis; however, samples were saved for future analysis. The aggregation issue is discussed further in section the performance section 4.1.4. A summary of the calculated rates including the LSR2 data are shown in the next section on Table 3. Analysis on trial LSR2 is discussed in the next section for better comparison.

### *4.1.2 Biotic vs Abiotic*

The LSR trials consisted of experiments comparing large-scale reactors using the New Belgium inoculum, and abiotic controls with only media as described in the methods section 3. During the second trial, 10 biotic reactors (LSRB2) were run in parallel but only reactors R4 through R10 were analyzed. This was due to the fact that reactors R1 through R3 had been recycled from trial 1 and showed different trends compared to the other seven due to the different cathode material. The abiotic reactors (LSRA2) were built from the sterilized recycled bodies of R1, R2, R3, and AB from trial 1, and ran after the LSRB2 were terminated to reuse the power supplies. Results using the 229 nm UV-Vis method and the rod mass losses are described below.

#### **4.1.2.1 Comparing BEGO rates using the UV-Vis method**

The purpose of the LSR reactors was to produce the BEGO at a larger scale using a tubular geometry and to collect larger volume samples for characterization. As previously mentioned in the methods section, leak tests on the LSR2 trial allowed for better sealing of the reactors and constant volumes. This made the LSR2 reactors have more stable behavior between replicates compared to the LSR1 trial (see Figure B11-B13 in Appendix B to compare data).

Concentrations over time are shown in Figure 6 for the biotic reactors (LSRB2) and for the abiotic reactors (LSRA2) using the 229 nm UV-Vis method only. Similar results are shown

in Appendix B Figure B13 using the 300 nm wavelength. The average production of the LSRB2 reactors was 0.096 g/Lday and production for the LSRA2 was 0.154 g/Lday (0.085 g/Lday and 0.145 g/Lday with the 300 nm method). The LSR2B reactors show a linear increase in BEGO for the first 34 days, consistent in all replicates. On day 50, concentrations start decreasing at different rates for all replicates; thus, different time periods were necessary to capture the production phase only. The LSRA2 reactors have a lag phase of around 26 days not seen in the LSRB2 reactors. Production was not detected until sampling day 38, after which BEGO production commenced, at what appeared to be a faster rate than the LSRB2 reactors. However, based on a t test on the data obtained comparing biotic and abiotic reactors, there was no significant difference between the production rates for the biotic and abiotic reactors (p value = 0.187).

The variation in the defined production phase time among LSRB2 reactors can most likely be attributed to the graphite rods depleting at different rates. As these rod bundles degrade, there is less surface area to react with and the reaction starts slowing down (see Figure B12-B13 for complete data). If the rod falls before complete depletion, there is no more production detected. The time period of the GO production between replicates was consistent in the LSR2A trial (~42 days with a ~26 day lag). By contrast, some inconsistencies were observed for the abiotic reactor rates; AB2 has a much lower production rate than AB1, AB3, and AB4. Potential explanations for these differences in rates will be discussed in the next sections 4.1.2.2 where rod degradation is analyzed in detail. Differences in rates were also directly related to differences in current production (Figure A7). When current decreased, the BEGO production decreased. Once the current hit 0 mA, no more BEGO production was observed.

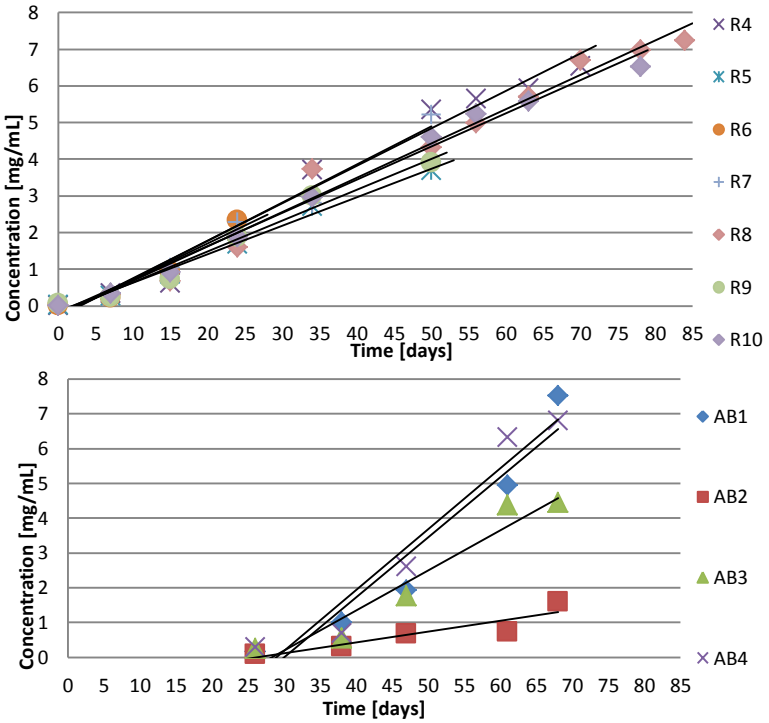


| Production rates [mg/Lday] | | | | | | | |
|---|---|---|---|---|---|---|---|
| **LSRB2** | **229** | **$R^2$** | **Lag [days]** | **LSRA2** | **229** | **$R^2$** | **Lag [days]** |
| R4 | 102.3 | 0.977 | 0 | AB1 | 172.6 | 0.921 | 26 |
| R5 | 77.8 | 0.989 | 0 | AB2 | 31 | 0.830 | 26 |
| R6 | 97.8 | 0.927 | 0 | AB3 | 115 | 0.931 | 26 |
| R7 | 103.9 | 0.976 | 0 | AB4 | 175.1 | 0.940 | 26 |
| R8 | 93.6 | 0.981 | 0 | | | | |
| R9 | 84.3 | 0.973 | 0 | | | | |
| R10 | 90.5 | 0.991 | 0 | | | | |

**Figure 6**: BEGO concentrations using UV-Vis method at wavelength 229 nm for the biotic reactors (top) and the abiotic reactors (bottom) for the LSR2

#### 4.1.2.2 Analysis of yields from rod degradation

Rod degradation analysis on reactors was done at the end of their lifetime similarly to the SSR1 rod mass loss analysis (see Figure 7 and Figure C4). An average of 65.2% degradation was found in the LSRB2 reactors and an average of 53.6% in the LSRA2. For LSR reactors, the top section of the bundles around 10-14 cm on the LSRB2 and around 10-17 cm for the LSRA2, were not submerged in the media. The differences in submerged surface area of rods may have affected BEGO yields, since only the graphite submerged played a role in the bioelectrochemical

production process. For some of the reactors (R4, R5, R9 and AB2) the graphite bundle detached from the anode connection early in the process and reactors were excluded from the statistical analysis as they were found to be outliers. The average production rates removing the outliers were 0.115 g/Lday for the biotic reactors and 0.159 g/Lday for the abiotic reactors. These are much more consistent with the UV-Vis data than the results from the SSR1 trial.

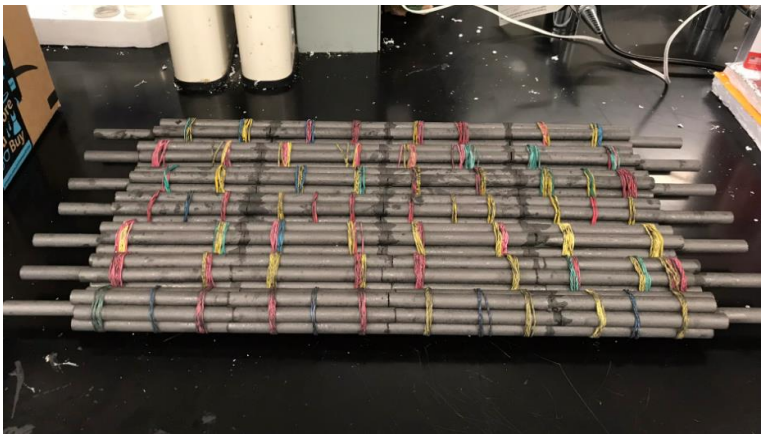

**Figure 7:** Rod bundles before BEGO process for the LSR2 trial


**Figure 8:** Rods R4-R10 before and after lifetime for LSR2

### *4.1.3 Reported rates of production*

A summary of production rates and reactor conditions are shown in Table 3. Lag phases were reported for the LSRA2 reactors. SSR1 had a delay in production but this was due to low voltage applied and not due to a lag in production. The different methods explored were compared with the previous study done by Lu et al. (first two rows). Looking at the BEGO

calculated from the dCOD method, the results from Lu et al. are similar to the results we found in the SSR reactors on the upper limit ranges. We used a dCOD to BEGO conversion formula to relate their produced COD during the entire time the reactors were connected (140 days) to our results. The BEGO Lu et al. reported in their supplementary information section was calculated from filtering with membranes of pore size 0.1-µm. Their calculated BEGO production was higher than our calculated BEGO using the same method. They adjusted their weighed filter mass by normalizing with the volume processed (100-mL) for a period of 31 days. They ran their reactors in a semi-batch mode replenishing the entire media volume 4 times during the entire experiment (140 days total). The 31 day period they used in their calculations was during the third new media replenish period. In our study, we ran our reactors in a batch mode and used a 0.5-µm membrane to collect the BEGO. We also processed the entire volume of the reactor instead of one portion (Lu et al., only processed 100 mL but their reactors were 220 mL). At the time, we chose 0.5-µm membranes thinking these might be good enough to capture all of the BEGO as was suggested looking at the permeate data (see section 4.2 for more details) but there is a chance some of the smaller BEGO molecules did not stuck to the filter as we expected. We also added a coarse membrane step that Lu et al. did not do for removing large particles. They instead centrifuged to remove solids (at 2,500 RPM, time unspecified) and then filtered the supernatant. It is possible that by changing the solid removal step to a coarse filter membrane, we might have lost some of our BEGO that stuck to this first membrane due to clogging. In our purification tests, 2,500 RPM was found to be too slow for all of the solids to completely settle out of solution; therefore it is possible that Lu et al. overestimated their BEGO produced. Without additional information (centrifuge model (g forces), or centrifugation times), this cannot be determined with certainty.

Comparing our methods with each other, the highest production was given by the weighed rods method and the lowest by the weighed filters followed by the dCOD method. It was expected for the dCOD method to be an overestimate of BEGO production due to other organic molecules being detected, but analysis showed this method actually resulted in lower rates than the UV-Vis methods. It was determined that due to the extra filtration step (0.2-µm pores) used to in the dCOD samples method larger BEGO particles were captured thus resulting in an underestimate of the BEGO in solution. In most cases (except for the LSRA2), the UV-Vis method reported higher BEGO concentrations at the 229 nm peak than the 300nm peak. During the LSR2 trial these differences in BEGO detected methods were less far apart, but averages still favored the 229 nm peak (see section 4.1.2.1 for reported averages). The production rates of the abiotic reactors appear to be higher, but analysis showed no statistical differences between both biotic and abiotic reactors (p value = 0.187). Although the abiotic reactors do appear to have higher production rates, they also have a delay in production of around 26 days before BEGO was detected on day 38. It is possible that these reactors were not as sterile as we anticipated and that a biofilm started forming in the rod surface, which might also explain the lag followed by a production phase. Further analysis on the abiotic media and rods is necessary to make conclusions regarding whether microbes ultimately colonized these reactors.

### *4.1.4 Performance*

Some operational issues caused our BEGO production to be lower than expected. Other than possible underestimations due to non-optimized filter pore sizes affecting the BEGO detected, run parameters also affected the biology and electrochemistry causing lower rates of production. By making improvements in our design, operation conditions, and purification

protocols in our first trials, we were able to improve performance overall in the second trials that allowed for better understanding of the process once uncertainties in parameters were removed. Below some of the performance issues and improvements that could affect the yields and production rates are discussed.

**Table 3:** Summary of reactor conditions and estimated production rate constants

| Reactor parameters | | | BEGO production [g/Lday] | | | | | |
|---|---|---|---|---|---|---|---|---|
| **volume [L]** | **Inoculum and source** | **Electrochemical conditions** | **dCOD** | **229 UV-Vis** | **300 UV-Vis** | **Weighed filters **** | **rod mass losses** | **Lag** |
| 0.22* | Anaerobic sludge from brewery digester | Cathode (WE) poised at -0.6 V vs. SHE | 0.036* | N/A | N/A | 0.388* | N/A | none |
| 0.22* | None | Cathode (WE) poised at -0.6 V vs. SHE | 0* | N/A | N/A | 0.08* | N/A | none |
| 0.4-0.5 | Anaerobic sludge from municipal wastewater digester | Anode (WE) poised at +1.6 V vs. SHE | 0.003-0.020 | 0.006-0.041 | 0.006-0.029 | 0.008-0.0185 | 0.22 | none |
| 0.4-0.5 | Pond sediments (>10 cm below sediment surface | Anode (WE) poised at +1.6 V vs. SHE | 0.011-0.016 | 0.016-0.022 | 0.010-0.014 | 0.003-0.002 | 0.147-0.26 | none |
| 0.4-0.5 | Anaerobic sludge from brewery digester | Anode (WE) poised at +1.6 V vs. SHE | 0.023 | 0.012-0.053 | 0.010-0.037 | 0.008 | 0.21 | none |
| 8 | Anaerobic sludge from brewery digester | Direct current applied to electrodes (3V) | N/A | 0.078-0.102 | 0.067-0.099 | N/A | 0.080-0.159 | none |
| 8 | None | Direct current applied to electrodes (3V) | N/A | 0.031-0.175 | 0.028-0.181 | N/A | 0.009-0.198 | 26 days |

*Results from Lu et al. (2015)
**Filters used to collect BEGO in Lu et al. study were 0.1-µm and in this study were 0.5-µm

During the first reactor trial (SSR1), a delay in production was seen until after 121 days (see Appendix B Figure B1-B2), depending on the detection method used. Some operational parameters (i.e., defective quadstats, RE leaks, and low voltage being applied) were changed between days 121 and 202 when BEGO production started being detected. The two quadstats originally used

were not able to display large currents or keep the voltage constant thus reactors were switched on day 114 to one octastat that was more reliable. A short increase in production was seen in the dCOD data on day 147 (Appendix B), followed by a larger increase after day 176. On day 175, maintenance was done on the REs due to electrolyte solution leaking into the reactors. Due to the long experimental runs (224 to 359 days), RE contamination was an issue; therefore, salt bridges were introduced on days 204 and 210. Another contributor to the production increase was voltage adjustments done to account for overpotentials larger than expected. To predict the overpotential of a system, CV analysis is usually conducted on the MES, but to avoid disturbing the microbial communities, this step was not done in our experiments and conditions were poised based on Lu et al. Figure A3 in Appendix A shows the voltage conditions over time with an increase from 0.82 V (vs Ag/AgCl) to 1.4V (vs Ag/AgCl) from day 181 to day 212. Around this time, the reactors started showing significant BEGO production. A combination of these changes to the reactor operating conditions led to the increase in production and allowed for better performance of the SSR2 reactors that were built and operated at the best conditions from the SSR1 trial. During the SSR2 trial, we saw no delay in production. Although the SSR2 reactors did improve compared to the SSR1, it was found that the reactor geometry was not optimal or stable due to the way the carbon clothes were affixed to the side of the flask. It was also found later in the experiments that channel 6 on the octastat was not displaying the correct voltage and found to be defective. This might have caused the N2 reactor in the SSR1 trial and the N3 reactor in the SSR2 trial to underperform. Future experiments at a small-scale with controlled electrode spacing and poised voltage from the beginning of the experiment is necessary to keep replicates reliable.

## 4.2 BEGO characterization

During the LSR1 trials, purification techniques were developed to concentrate BEGO flakes for analysis of solids. Samples also were sent to Larry Lien at MDS for purification via membrane filtration. Liquid samples from the R1 and R2 reactors (2-L each) revealed that BEGO sizes varied extensively (data not shown); thus, a series of filtration tests were done to determine the optimal molecular weight cut-off (MWCO). During this analysis, it was visibly established that the BEGO could be captured using anywhere from 500 to 10,000 MWCO. Only "clear" color permeate was achieved with 500 MWCO (nanofiltration around 0.001-µm). After doing UV-Vis analysis on the permeate of different membranes tested, low detection at the 229 nm indicated BEGO was collected on the membrane surface at a higher range of MWCO filters. Considering achievable flow rates, membrane efficiency, and permeate data, a 0.5-µm (microfiltration between 0.03 and 10-µm collects between 100,000 and 1000,000 MWCO) Teflon membrane was chosen to concentrate the BEGO. This process was replicated at CSU with the process described in methods section 3.4. Analysis on the R2 samples collected on the membrane is shown below. Other results from the SSR1 and LSR2 samples are also shown. More data can be found in Appendix E.

### *4.2.1 UV-Vis*

UV-Vis scan data using wavelength ranges from 210 nm to 800 nm are shown in Figure 9. Spectra show trends consistent with literature data for GO [156,157] and with the purchased GO sample (see Figure E1 in Appendix E). The UV-Vis spectra for this analysis were originally collected by scrapping the material from the surface of the BEGO filter and suspending it in DI water (see results in Figure E2). Complete dissolution was not achieved with manual mixing; thus, sonication was thought to be necessary to further analyze these samples. It was decided not

to test these samples thus to remain consistent with the rates data, the centrifuged samples were analyzed here instead. Serial dilutions were necessary to be under the quantification threshold (~2 AU) that the instrument allowed for smooth peaks. Large dilutions were necessary (~1:200) once the reactors were a few weeks into the production phase. Looking at the UV-Vis spectrum it can be seen that the BEGO has low signals at the 300 nm peak, which indicates little to no presence of carbonyl/carboxyl functional groups. This might indicate BEGO does not have as many active sites present but has potential for reduction into rGO. Since it has fewer defects, there is a better chance for the recovery of $sp^2$ carbon for applications in electronics. More data can be found in Appendix E for other trials.

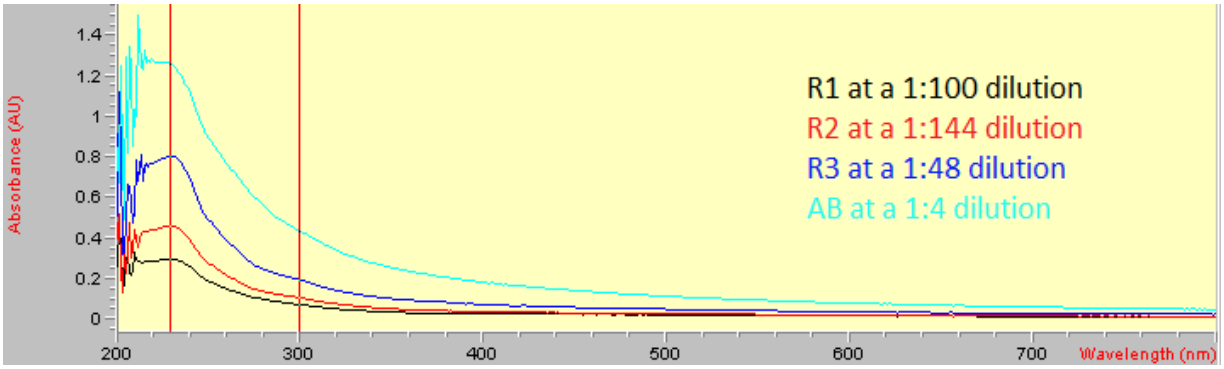


**Figure 9:** UV-Vis scans from wavelength 210 nm to 800nm for the LSR1 reactors. Dilutions in DI water were necessary for smooth curves below 2 AU. The samples shown are taken from reactors on day 97

### *4.2.2 FT-IR*

FT-IR results showed peaks consistent with GO functional group spectra (Figure 10). From left to right, a broad peak appears around 3200 $cm^{-1}$, which corresponds to hydroxyl O-H (alcohol, phenol) groups attached to the graphene. Small C-H stretches appear at wavelengths of 3000 $cm^{-1}$ and 2850 $cm^{-1}$ (alkenyl, alkyl) and are most frequently due to unsaturated compounds. These C-H peaks are small and could be attributed to sp3 defects, in theory concentrated mainly around the edges [4]. A small shoulder located around 1720 $cm^{-1}$

corresponds to the signal for C=O stretching of carbonyl and/or carboxyl functional groups. A shoulder around 1620 $cm^{-1}$ and larger peak at 1550 $cm^{-1}$ next to it correspond to C=C aromatic ring stretches and C-OH bending, respectively. One peak around 1400 $cm^{-1}$ is associated to the O-H bending vibrations in C-OH bonds. Lastly, the signals around 1220 $cm^{-1}$ and 1040 $cm^{-1}$ correspond to C-O stretching vibrations of C-OH (alkoxy) or C-O-C (epoxy) functional groups. Samples match analysis found in the literature for GO produced with other techniques with a few minor differences in peak transmittance that vary depending on the production method [19,163,164].

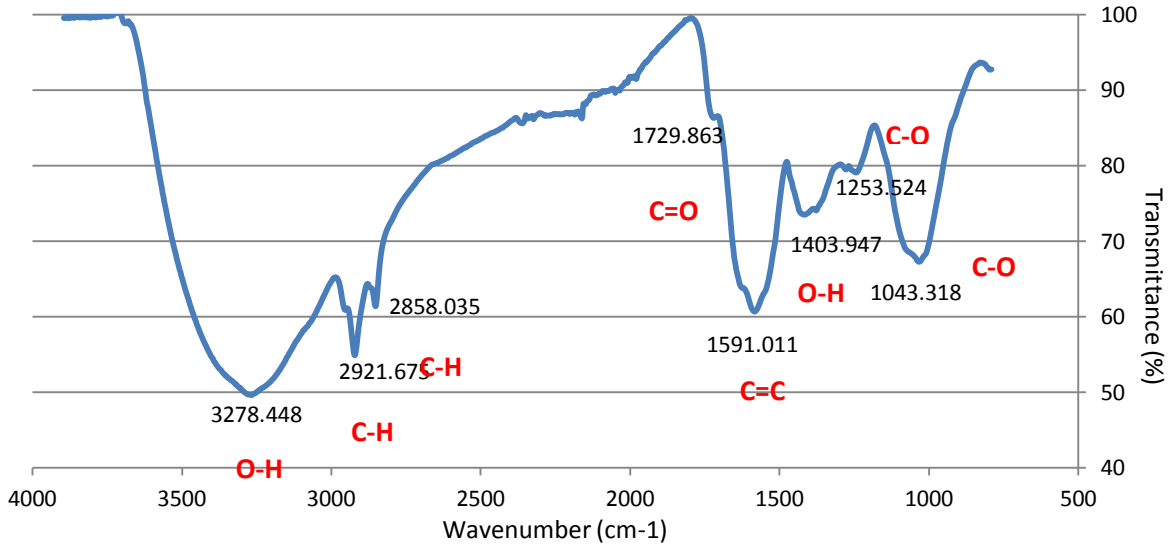


**Figure 10:** FT-IR spectrum from R2 reactor from LSR1

*4.2.3 TGA*

The TGA was done on the powdered samples from the scraped membranes in the LSR1 trial. TGA showed two main weight loss events consistent with GO behavior (Figure 11). The first event happens around a temperature range of 25- 100 °C where 11-15% of the original weight is lost most likely due to water molecules adsorbed to the BEGO leaving the sample and hydroxyl groups being removed. The second event occurs around 200°C and it is attributed to

labile functional groups leaving the material. This weight loss is close to 25% of the original mass and results in the production of gases such as CO, $CO_2$, and steam. After 400°C the weight loss rate slows down which can explained by the removal of more stable functional groups (C=O). More extreme treatments are necessary to remove all functional groups and reform $sp^2$ bonds. These two main events and weight loss percentages are consistent with studies done on GO [165,166] .

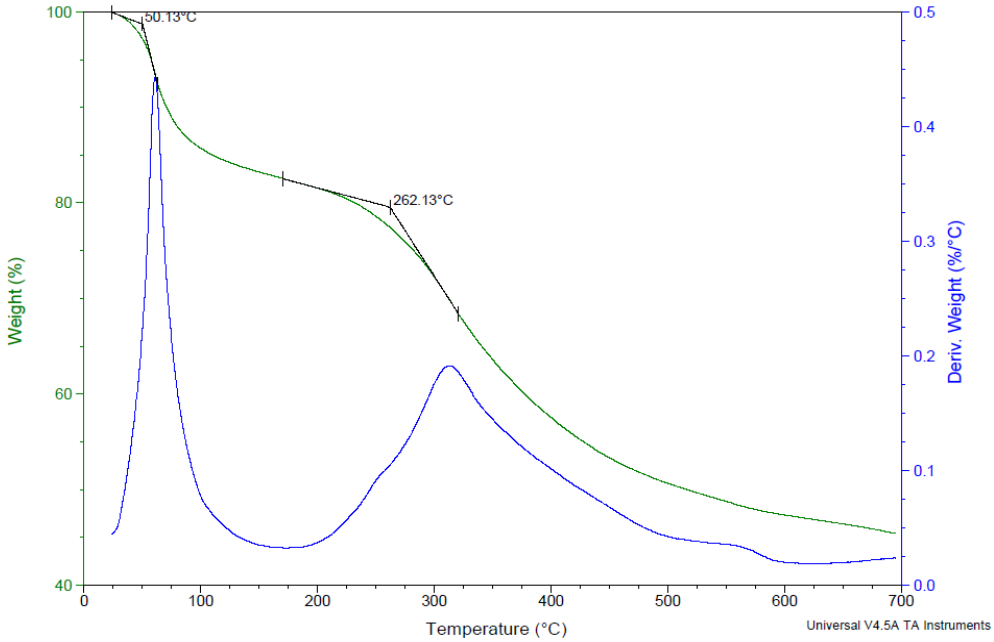


**Figure 11:** TGA analysis on powder R2 samples from LSR1

### *4.2.4 Raman*

The Raman spectra analysis of LSR1 samples showed two bands of interest (Figure 12, top). The G-band at 1583 $cm^{-1}$ represents the planar configuration of $sp^2$ bonded carbon, and the D-band at 1300 $cm^{-1}$ represents expression of the $E_{2g}$ vibration mode of $sp^2$ carbon atoms. The D-band is present in a carbon sample as an indicator of "disorder" present in the carbon molecules. The spectra of a pure graphite sample is characterized by organized C=C bonds expressing a narrow G-band and no D-band [167,168]. The Raman of the BEGO samples shows

a large D-band with visibly $I_D/I_G$ ratio greater than 1 consistent with GO data. This is expected due to the large amount of functional groups present and $sp^3$ defects. The LSR2 images for the biotic reactors Figure 12, bottom) show the same behavior as the preliminary trials with the intensities almost 3X higher, which decreased noise from the spectrometer as it can be noted from the smoother plot. Higher signal is also an indicative of higher concentrations as the samples were not diluted for these assays and LSR2 had shown better performance than LSR1 trials.

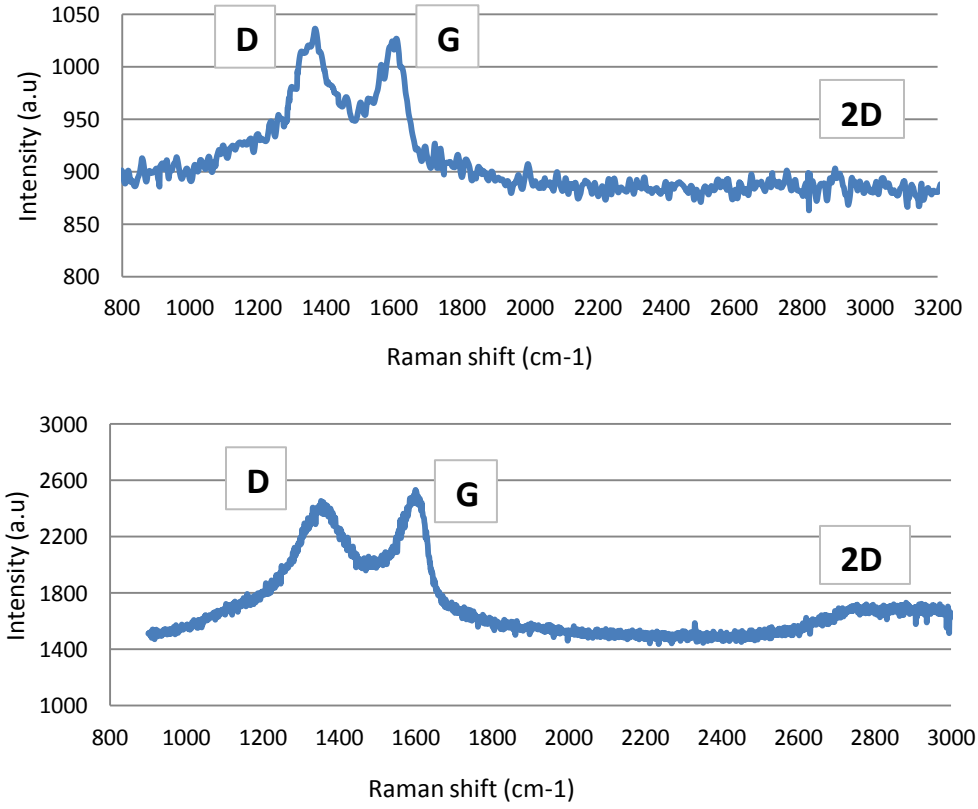


**Figure 12:** Raman spectrum of LSR1 (top) and LSR2 (bottom) at the end of their lifetime.

### *4.2.5 TEM*

Finally, microscopy analysis done on samples from the SSR1 trials suggests few-layered structure materials. The exact number of layers or whether the layers are attached of just sitting

on top of each other was not analyzed. Images from the D1 sample of the SSR1 reactors are shown including the fast Fourier transform (FFT) to visualize the geometric characteristics of a spatial domain (Figure 13). Structures found in the SSR1 samples ranged from a few nm in lateral size, to around 5 μm. Different transparencies shown on the TEM image indicate changes between numbers of layers stacked on top of each other. This is common in single/few-layered structures compared to multilayered structures (graphite) that become opaque and differences in layers deposited are no longer visibly distinguishable. One way to visualize that layers are stacked (and not bonded) on top of each other is by looking at the FFT images. Hexagonal structures are present and at least 4 different hexagonal patterns are apparent in the single image. If there was only one flake of GO in the image shown, only one hexagonal pattern would be apparent in the FFT. Recall that increasing the oxidation of the BEGO increases the transparency of samples as they become easily exfoliated into monolayers (or few layers) [4,169,170].

The images showed wavy structures, which is common for single to few-layered graphene due to the unstable van der Waals forces [171] and in the GO due to functional groups present. Graphite structures under TEM show rigid, darker structures because of the presence of stable multiple layers [172]. Some of the structures found also exhibited dim edges which are thought to be the most oxidized part of the GO structures (data not shown). Other structures appeared to be too weak to sustain the beam and were destroyed during visualizing. Single layer structures might be too sensitive to the beam voltage, which is why few layers were easier to identify. More TEM images can be found in Appendix E (Figure E9-E13).

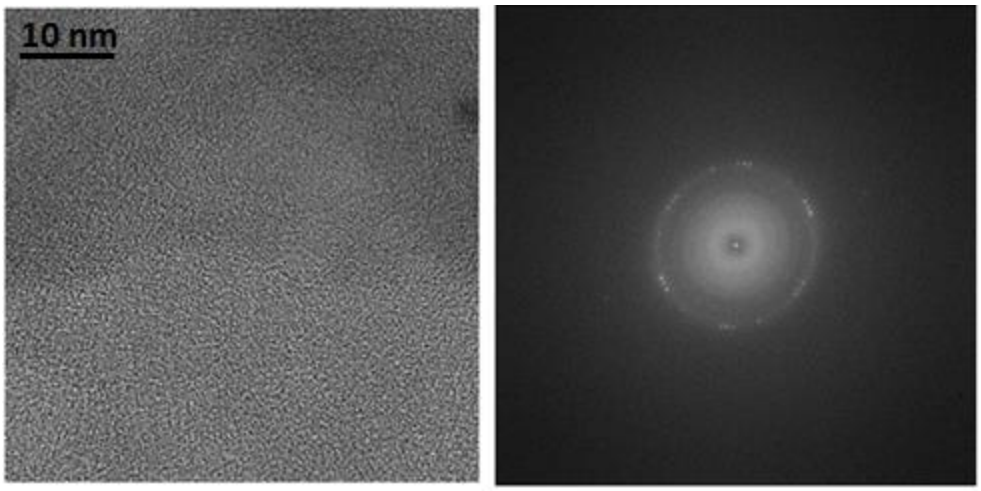


**Figure 13:** TEM images (left) and FFT (right) for D1 samples from SSR1

The key properties of BEGO found indicate exfoliation into few-layers was successful but further analysis is required to measure the exact spacing between sheets as well as surface areas. The data indicates the material produced is indeed GO with large disorder ratio ($I_D/I_G$ visible in Raman). The type of functional groups present might vary with inoculum (see Figure E7-E9). The carbonyl/carboxyl functional groups, unlike the purchased GO produced from Hummers' method, are detected at a lower concentration (from FT-IR and UV-Vis data). These groups are very stable and have value in biosensing applications, but the lack of these means the BEGO is probably easier to reduce thus having more appeal in rGO applications and possibly for producing graphene flakes. More characterization results can be found in Appendix E.

### 4.3 Microbial analysis via 16S rRNA Gene Sequencing

The microbial analysis was done to be able to identify the key microbial communities in the different inoculum sources to be able to have a better understanding of the role of these microbes. A taxonomy study was done using DNA and RNA extracted from the SSR1 trial at the beginning and end of the reactor lifetime. DNA analysis provided information on the type of

microorganisms present and their functional capabilities, while RNA analysis provides information on which microorganisms are active. Gene sequencing of the 16S rRNA gene was performed to identify abundant microorganisms in each MES reactor. Data obtained are presented as percent abundance of microbial phyla/genera at different percent abundance cut-offs for easier visual analysis. For the first set of extractions (on day 32), both the connected and the control reactors were compared sampling from the bulk liquid solution, and the rod biofilm. A second set of extractions (days 231 and 233) were performed on the connected reactors alone. Due to the extensive number of samples sequenced, a key code chart is shown in Table 4 describing the naming arrangement.

The most abundant communities found both in the bulk and rod biofilm consisted of aerobic, facultative, and anaerobic bacteria. Since water splitting was occurring inside of the reactors, $O_2$ production at the anode lead to the environment not being fully anaerobic. RNA extractions were difficult due to low yield; thus only a few samples were sequenced per extraction date. Rod sample collection on day 32 was difficult due to low biofilm visibly present, and nucleic acid yields were also low. In depth analysis on the samples collected on DNA and RNA extractions for both the bulk (B) and rod biofilm (R) are discussed below.

**Table 4:** Key code for DNA/RNA figures

| **Sample name key code** | | | |
|---|---|---|---|
| 1st Letter | Reactor type | Control (disconnected) or potentiostat (connected) | C or N/A |
| 2nd Letter | Inoculum type | Drake sludge, New Belgium sludge, or pond sample | D, N or P |
| 3rd Letter | Duplicate number | First or second | 1 or 2 |
| 4th Letter | Sample type | Rod biofilm or bulk media | R or B |
| 5th Letter | Nucleic acid type | RNA or DNA | RNA or N/A |

*4.3.1 Phylum Level*

Results of the phylum classification at a 1% abundance cut-off on days 32 and 231/233, are shown in Figure 14. The first 11 samples on day 32 are the disconnected controls (C); these showed the least amount of variation between duplicates as expected since conditions were consistent. The most abundant phyla present in all the reactors on day 32 were the *Proteobacteria,* followed by *Bacteroidetes, Thermotogae, Spirochaete, Firmicutes, Cloacimonetes,* and *Actinobacteria.*

For the connected reactors,the New Belgium inoculum (N) showed the largest variety of phyla in the DNA bulk samples (NB), having the largest abundance of *Thermotogae, Spirochaete,* and *Cloacimonetes* (>10%). The *Thermotogae, Spirochaete*, and *Actinobacteria* phyla in the N bulk DNA increased in abundance with the applied electrochemical conditions compared to the control samples (CNB). On the other hand, all of the other inocula samples showed only some of the previously mention phyla in the N samples, at about 5% or lower abundance having less variety of communities. The Drake inoculum bulk samples (CDB and DB) for DNA and RNA samples appeared to have the largest population of *Bacteroidetes* (43-73%) compared to the other inocula. The pond inoculum bulk samples of the connected reactors (PB) showed a significant increase of *Tenericutes* (2.8-3.7%), *Spirochaete* (3.0-5.2%), and *Cyanobacteria* (1.6-8.2%), with the applied electrochemical conditions compared to the controls (CPB) that have these at less than 1% for both DNA and RNA samples. As for the extractions from the rod biofilm, samples obtained from all of the reactors generally showed much more prominent *Proteobacteria* communities (84.5-99.7%) than any of the other samples.

Extractions done on days 231/233 showed higher variations between replicates that do not show trends between the same reactors from duplicates compared to day 32 (See Figure 14,

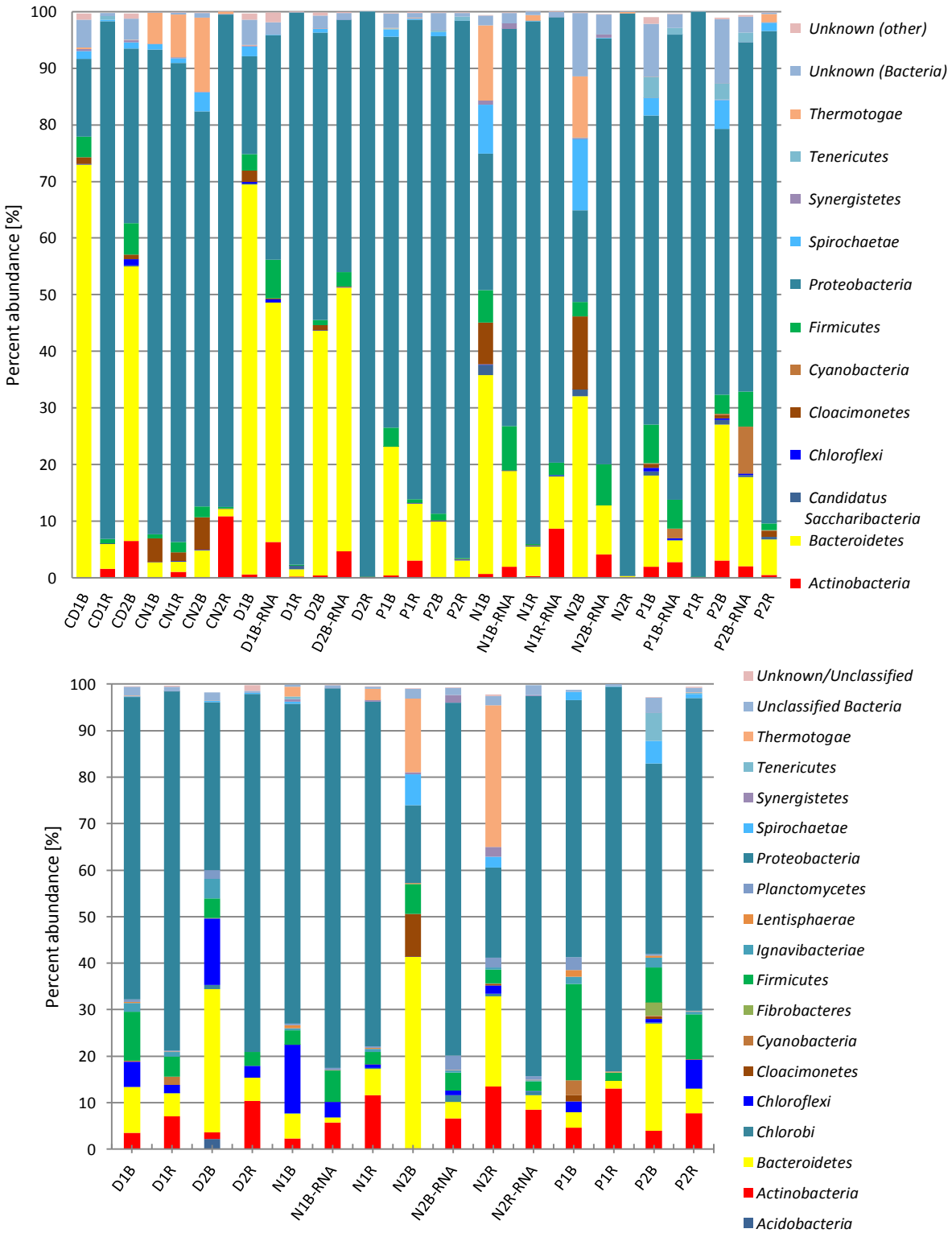


**Figure 14:** SSR1 sequencing results at a phylum classification with 1% microbial cutoff on day 32 (top) and days 231//233 (bottom)

bottom). *Chloroflexi* phylum becomes abundant in all of the reactors, especially in the bulk of the D2B and N1B reactors with abundances of almost 15%. The N2 reactors conserved the community variability seen on day 32. *Thermotogae* were enriched showing around 30% abundance in the rod DNA samples. In contrast, for the replicate N1, these phyla decreased showing less than 3% abundance of the *Thermotogae* phylum, and no detected *Spirochaete* or *Cloacimonetes* in both bulk and rod DNA/RNA samples (PN1B, PN1R, and PN1B-RNA). Patterns noted in all of the reactors were the decreasing abundances in *Bacteroidetes* communities (highest on day 32 was 72% compared to the highest on days 231/233 of 30%) excluding the N2 samples. *Proteobacteria* remained the most prominent microbial group in all DNA/RNA samples excluding N2. N2 had the smallest abundance of *Proteobacteria,* and the least variation from day 32 communities. These trends suggest that the underperforming reactor N2, which had high salt, did not produce communities that supported GO production compared with the other reactors that were more similar to each other at the phyla level.

*4.3.2 Genus Level*

At the genus level, a 1% cut-off resulted into too many genera to display visually; thus a 5% cutoff was chosen instead (See Figure 15 and Figure 16). Extractions on day 32 (Figure 15) showed that the control replicates of the same inoculum source had similar communities to each other mainly in the bulk samples. The CDB samples contained high percentages of *Bacteroidetes* (unknown/unclassified). The CNB/CNR reactors contained high percentages of *Arcobacter* (7-13% in the rods and 43-50% in the bulk samples), followed by *Mesotoga, Comamonas*, *Candidatus Cloacimonas,* and *Pseudomonas* (>5%). The CPB reactors contained mostly *Sulfuricurvum* (31-63%) followed by unknown *Bacteroidetes, Comamonas,* and *Aeromonas* (>5%). DNA analysis on the rod samples showed that *Pseudomonas* and *Comamonas* were the

most prominent genera in of the control reactors, except for CP2 which contained mostly *Marinobacter* at over 70% abundance. No RNA samples were extracted from the control reactors.

The connected reactors on day 32 showed much larger variability in between replicates in the bulk samples compared to the control reactors. The DB reactors showed similar communities on the control CDB, except for the increase in *Pantoea* (36%) abundance in D2B. These similarities in the D genera abundances from both control and connected reactors are mainly due to the fact that the prominent communities are either unknown or unclassified; therefore, conclusions cannot be made about the similarities (or differences) between reactors. The NB showed much more variety than CNB with enriched communities of *Candidatus Cloacimonas, Mesotoga, Sphaerochaeta, Bacteroidales* (unknown), *Bacteroidetes* (unknown) greater than 5% at least for one of the two replicates. Compared with the CNB controls, the NB also showed no significant presence of *Arcobacter* or *Commamonas* (<= 5%). The PB reactors also had more variability compared to the controls CPB with enrichment of *Bacteroidetes* (unknown), *Ochrobactrum, Shinella, Desulfobacola, Campylobacteraceae* (unclassified) greater than 5% but decreasing *Sulfuricurvum* (<8%) for at least one of the replicates. Looking at the rod biofilm DNA samples, communities consistently show that the *Pantoea* genus is the most abundant by a large margin (77-96%) regardless of the inoculum used.

In general, general, RNA samples looked very similar to the DNA counterpart of the same reactor. The bulk RNA of the connected D samples (DB-RNA) showed high abundance of unknown *Bacteroidetes* (41-46%), like in the DNA extractions. However, unlike the DNA, the DB-RNA sample also showed some increasing abundance of *Methylomonas* above 5%. RNA samples for the N reactor replicates (PNB-RNA) were very different from each other. PN1B-

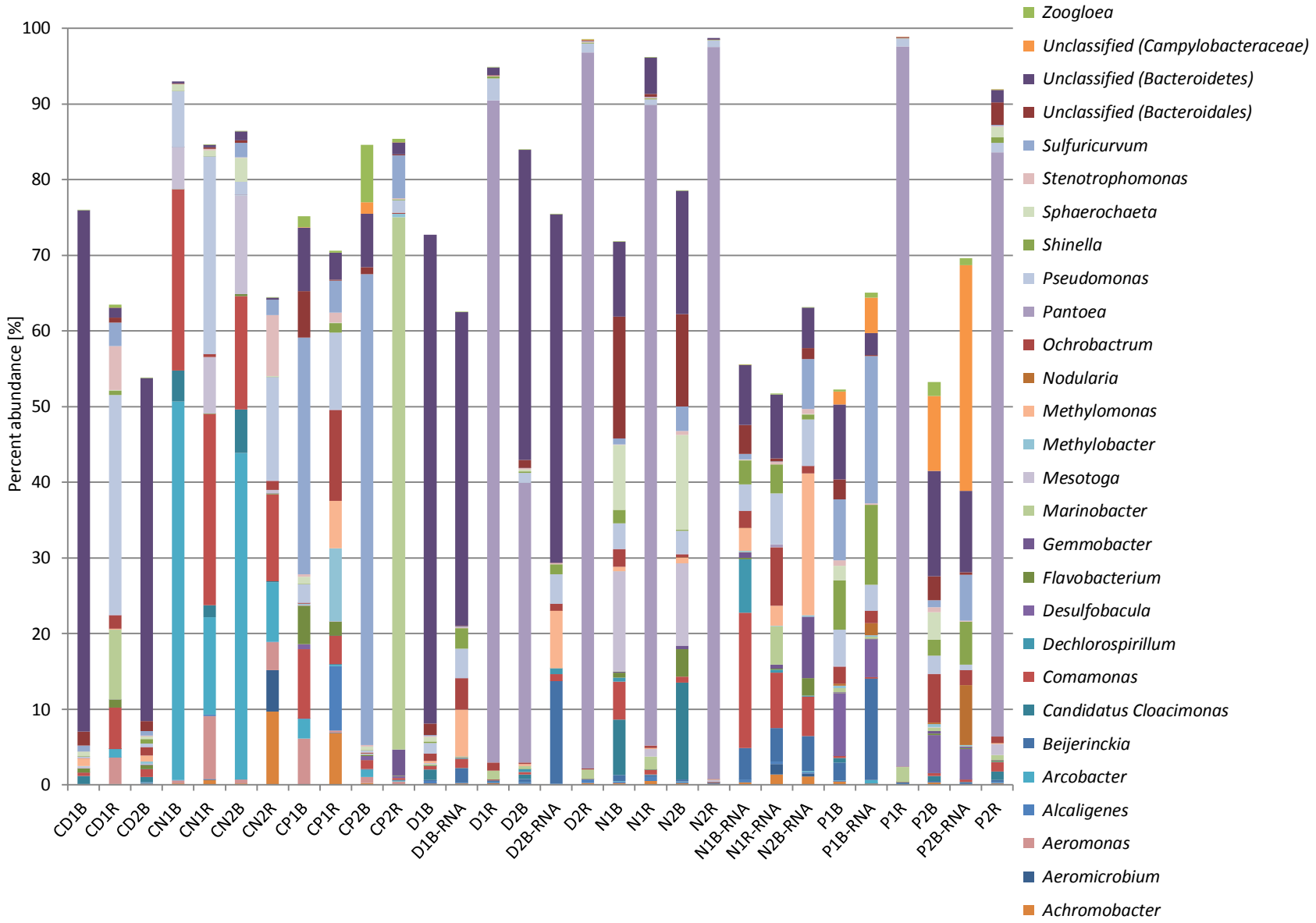


**Figure 15:** SSR1 sequencing results at a genus classification with 5% microbial cutoff on day 32

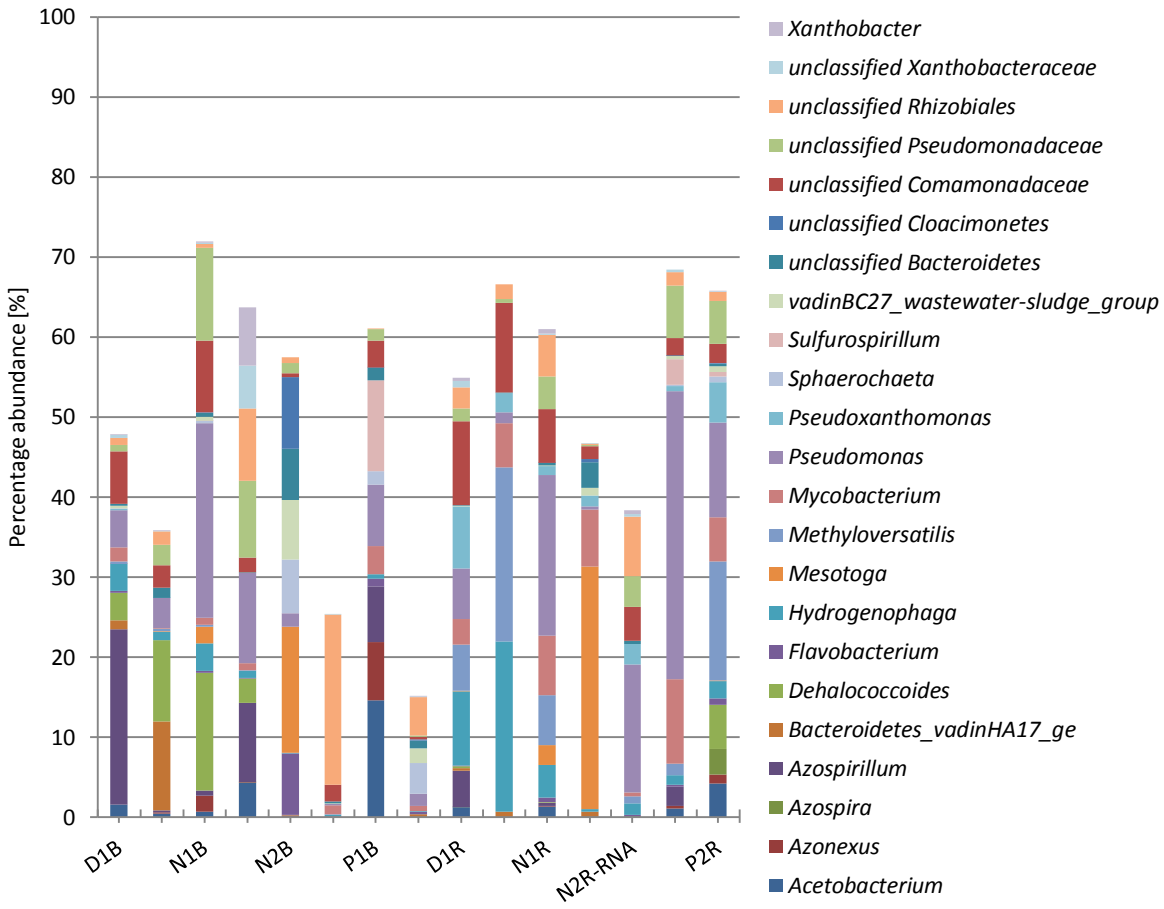


**Figure 16:** SSR1 sequencing results at a genus classification with 5% microbial cut-off on days 231/233 for the connected reactors only

RNA is mostly similar to the DNA sample from the same reactor with enrichment of *Dechlorospirillum, Comamonas* (> 5%), and decreasing *Candidatus Cloacimonas, Mesotoga, Sphaerochaeta* (< 1%). On the other hand, the replicate N2B-RNA, looked nothing like the DNA sample of the same reactor. This reactor has higher abundance of *Gemmobacter, Sulfuricurvum, Methylomonas,* and *Pseudomonas* (>5%) but none of the prominent genera in the DNA bulk mentioned before (below detection limit). Lastly, the RNA of the bulk in the P reactors (PB-RNA) showed similar results to the DNA analysis, except for larger communities of *Nodularia* (7.4%) that enriched in reactor P2. As for rod biofilm, only one sample was sequenced for reactor N1. The communities in N1R-RNA were very similar to the bulk RNA of the same

reactor with larger concentrations of *Marinobacter* and *Ochrobactrum* (5%), but no *Dechlorospirillum* detected.

Genera analysis on days 231 and 233 is shown in Figure 16. Like with the phylum level data, replicates of the same inoculum showed no similarities. Since populations varied extensively between the reactors, only communities representing 10% or more in abundance were analyzed. For bulk DNA samples only, the D1B reactor showed abundance of *Azospirillum* (22%), whereas D2B showed *Dehalococcoides* and *Bacteroidetes* (vadinHA17_ge) at around 10%. The N1B reactor showed abundance of *Pseudomonas* at 34%, and both *Dehalococcoides* and *Comamonadaceae* (unclassified) at around 10%. The replicate N2B showed abundances of *Mesotoga* (16%) and some unclassified *Cloacimonetes* (10%). The P1B reactor contained mostly *Acetobacterium* (15%) and some *Sulfurospirillum* (11%) and the replicate P2B did not contain amounts of a single genus at a 10% or above abundance.

The rod extractions on days 231 and 233, unlike on day 32, showed no clear trends between reactors and do not have the *Pantoea* genus at the cut-off abundance percentage. The *Pantoea* genus is categorized as facultative anaerobic bacteria from the *Proteobacteria* phylum [173]. A research study on antimicrobial activity of graphene-based perioceutics showed inhibitory activity of GO materials in some bacterial strains including the *Pantoea* spp. It is possible that as the BEGO concentration increased, this genus was inhibited until no more detection could be observed [169]. Extractions for both D rod samples showed abundance of unclassified *Comamonadaceae* (10-11%), and *Hydrogenophaga* (9-21%), with D2 also showing high abundance of *Methyloversatilis* at a 22%. N1R showed mostly *Pseudomonas* abundance (20%), whereas N2R contains mostly unclassified *Mesotoga (*30%). Finally, P1R shows the

largest community of *Pseudomonas* at a 36%, which were also present in P2R at a lower percentage (11%), with the highest abundance being the *Methyloversatilis* genus at a 15%.

Three RNA samples were sequenced due to low yield in the other reactors. Two bulk RNA samples from the N1 and N2 reactors showed a significant amount of unclassified *Rhizobiales* (9-21%), but only N2 showed significant abundance of *Azospirillum* and *Pseudomonadaceae (*unclassified) around 10%. The single rod RNA sample sequenced from N2 also showed *Pseudomonas* as the most prominent genus at 16% abundance.

Looking at the genus data of the most prominent microorganisms at the anode (graphite rod biofilm) for days 231/233 some conclusions regarding microbial communities in the bioreactors can be made. There are aerobic, anaerobic and facultative microorganisms in the system, despite the MES being considered anaerobic. Voltages applied at the anode were high enough to split water resulting in local oxygen production, explaining the presence of aerobes. *Pseudomonas,* which was the most abundant genus on days 231/233 in the rod biofilm, are generally considered aerobic (in some cases anaerobic using nitrate as electron acceptor) [170]. This genus was also the most abundant in the Lu et al. study [19]. In their study, *P. syringae* was the most abundant species; although there is no information available suggesting this species can carry out any bioelectrochemical processes of extracellular electron transfer. Some other strains of *Pseudomonas*, specifically *P. aeruginosa* [171] and *P. alcaliphila* [177], have been shown to excrete mediators to transfer electrons to the anode. Other genus-level communities found in days 231/233 include *Hydrogenophaga, Methyloversatilis* and *Mesotoga. Hydrogenophaga* are aerobic bacteria capable of using the oxidation of $H_2$ as an energy source and $CO_2$ as a carbon source. Oxidative carbohydrate metabolism occurs, with oxygen as the terminal electron acceptor [173]. Due to water splitting present in our reactor (GC analysis not shown), we had

$CO_2$, $O_2$, and $H_2$ gas present in our reactors. These molecules can play an important role as they are metabolized by microorganisms present and can alter communities depending on their abundance. The role of these molecules to understanding the redox reactions occurring and their effect on microbial communities was beyond the scope of this study.

All of the prominent genera mentioned are in the *Proteobacteria* phyla, except for the *Mesotoga*, which is of the *Thermotogae* phylum. The *Mesotoga* genus was found in high abundance in the N2 reactor, which had the most variety at the phylum level. The N2 reactor is also the bioreactor that underperformed in BEGO production. This might indicate that the *Mesotoga* abundances are a result of the unique conditions in this reactor (high salt content) and might not be an important microbial genotype in the reactors for biocatalysis of BEGO. Further analysis, possibly at the strain level (e.g., via metagemonic sequencing) could potentially give us more information regarding the biocatalytic capabilities of the microbial communities found throughout this study.

# 5. CONCLUSIONS

Estimation of BEGO production rates using the UV-Vis method at 229 nm was shown to be a useful quantification approach. This wavelength is specific to GO as it corresponds to the $\pi \rightarrow \pi^*$ transitions of aromatic C-C bonds comprising the majority of the molecule, regardless of the oxidation state. This method was corroborated with a parallel study using yields from membrane collection protocols (see section 4.1.1.4). To be able to collect all of the BEGO in powder form, membranes with smaller MWCO are necessary. To purify the samples for analysis, the centrifugation protocol at 10,000 x g for 15 minutes proved to be reliable for quantifying BEGO in solution. Better filtering methods might be necessary (smaller MWCO membranes) to be able to characterize our material under the most sensitive techniques (i.e. TEM, XPS).

The nanomaterial characterized was found to have less carboxyl/carbonyl groups compared to the GO produced by the traditional Hummers' method. This is useful information when attempting reducing methods as harsh reducing agents might not be necessary. Lower carboxyl/carbonyl groups indicate less active sites for biocatalyst applications, but also means better conductivity for the large market of graphene-based technologies in electronics. Characterization analysis also revealed the BEGO process yielded sheet sizes of a few hundred nm to 1-2 μm in lateral dimensions. Transparency and Fast Fourier transform (FFT) images indicate the BEGO consists of only single-layered to few-layered structures, which are more valuable for downstream applications.

The microbial analysis done on bioreactors showed large divergence from the original inoculum sources and among the reactor replicates. Microbial communities in the BEGO producing reactors consisted of both aerobic and anaerobic microorganisms. The most abundant

genera on the rod biofilm were the *Comamonadaceae* (10-11%), *Hydrogenophaga* (9-21%), *Methyloversatilis* (15-22%), and *Pseudomonas* (11-36%), all from the *Proteobacteria* phylum. Further analysis of the potential enzymatic characteristics of these microbial genotypes is necessary to understand the role they play in catalyzing the BEGO process.

# 6. FUTURE WORK

Due to the novelty of the BEGO method, the nanomaterial present in the complex matrix needs to be fully understood to be able to properly purify samples before analysis. Evaluating the precision of the UV-Vis method with respect to the standards is crucial to be able to properly quantify the BEGO process in the future and target the appropriate market. Since our BEGO has characteristics that are different from the Hummers' method GO, understanding these differences with respect to the UV-Vis analysis is important to properly calibrate our concentrations. The BEGO process might have an effect on the sheet sizes produced compared to the purchased GO using from the Hummers' method. Differences in sheet sizes could affect the spectra data collected with respect to our calibration standards. Further microscopic analysis and particle size distribution analysis comparing sheet dimensions of our BEGO and the standards used during calibration could be done to improve the detection method. Complete analysis can be achieved with a thorough AFM imaging and topography analysis on the standards and samples as well as SAXS/WAXS [156]. A complete AFM analysis can also be useful when understanding the number of layers present on the BEGO for electronic application purposes. Recall that with multilayer flakes, the material becomes less conductive.

Current electrochemical methods have reported monolayer production of GO within hours [52]. These methods are at a smaller scale and have been reported using higher voltages than the BEGO process. The BEGO process rates observed in this study might be slower, but there are many factors affecting the rates including voltage applied, reactor size, graphite form, electrode/electrolyte choice, and electrode spacing that can be further optimized. The BEGO process in this study currently takes between 48 and 111 days of active production before

concentrations peak (see section 4.1.4). Lu et al. reported rates of production for 31 days that were higher than the electrochemical method (see Table 3). There is a benefit from having microbes in the system. Whether these improvements are caused by unique microbial communities on the rod (or even in the bulk) or if just the presence of a biofilm is enough to decrease the overpotential should be investigated.

Improvements can be made to decrease the operation time and increase yield. Increasing the production rates (decreasing production time) could be achieved by decreasing the spacing between electrodes, and distributing the current more evenly between them. One option could be to connect the power supply to opposite ends of the electrodes; this might ensure current travels throughout the reactor length avoiding weak points in the electrodes where electron transfer is favored.

To avoid the aggregation issues hypothesized, design improvements can also be made. Salt content (NaCl and KCl) could be decreased by adding and constantly maintaining the vycor frit tips on the salt bridges (and REs) in the three-electrode configurations. Studying the effects of decreasing the presence of key ions in our recipe, mainly $Na^+$ since a phosphate buffer is the largest portion of the total volume (see Table 1), can provide information regarding where the threshold is until BEGO starts aggregating. These key ions have a strong correlation with GO aggregation and should be monitored closely. Having high salt concentration is usually favorable for electrochemical systems; thus analysis on the proper concentrations that can optimize both the BEGO solubility and the redox chemistry are necessary. Another hypothesis regarding decreasing BEGO concentrations was the possibility of reduction occurring in the bulk phase decreasing the hydrophilic behavior of the BEGO. One previous study on the reducing properties of certain bacteria suggested that some microbes can degrade GO, restoring the graphitic mineral

form [174]. Analysis on the biofilm at the cathode might provide insight regarding whether the communities present can use organic compounds as terminal electron acceptors

The role of this biofilm should be studied thoroughly if we want to determine the mechanism for BEGO production. It is currently unknown if BEGO is produced by specific microbes with specific enzymes, or if just the physical presence a biofilm is enough to affect the overpotential. Doing full metagenomics can help understand the capabilities of the microorganisms and look at trends between communities. Key microbes can be isolated and enriched in the bioreactors for proteomics analysis. Looking at the enzymatic properties of the hypothesized key microbes can be a breakthrough and help potentially biocatalyze other MES systems that operate under similar conditions. Understanding the role of the microbes in the anode (and/or cathode) interphase could also help understanding the mechanism as to if and how the key bacteria may metabolize the graphite and possibly the $CO_2$, $H_2$, and/or $O_2$. If a mechanism is discovered we can potentially create a model in which we can alter the important parameters and predict changes in the BEGO process.

Finally, BEGO can be reduced into rGO for wider downstream applications. Our research collaborators tested using microwaving protocols (data not shown), but methods have not been fully developed for scale-up. Previous studies have shown low C:O ratio (4:1) achieved with the microwaving reduction method whereas typical values for rGO are usually around 12.5:1 [20]. Methods including the use of reducing agents such as Vitamin C, electrochemical reduction (possibly bioelectrochemical), and wild carrot roots, have reported more efficient green approaches that increase the C:O ratio to a range of 11.9 to 23.9 C:O. Hydrazine, which is considered the most efficient GO reducing agent (see section 2.2.3), is a hazardous chemical; since our focus is on environmentally sustainable approaches, the previously mentioned methods

might be more suitable. The electric properties of the rGO can then be measured to widen the market applications of the BEGO in electronics.

# REFERENCES


1. Geim AK, Novoselov KS. The rise of graphene. Nanosci Technol Collect Rev Nat J. World Scientific; 2010. p. 11–9.

2. Balandin AA, Ghosh S, Bao W, Calizo I, Teweldebrhan D, Miao F, et al. Superior Thermal Conductivity of Single-Layer Graphene. Nano Lett. 2008;8:902–7.

3. Lee C, Wei X, Kysar JW, Hone J. Measurement of the Elastic Properties and Intrinsic Strength of Monolayer Graphene. Science. 2008;321:385–8.

4. Zhao J, Liu L, Li F. Graphene Oxide: Physics and Applications [Internet]. Berlin, Heidelberg: Springer Berlin Heidelberg; 2015 [cited 2019 Feb 8]. Available from: http://link.springer.com/10.1007/978-3-662-44829-8

5. Bolotin KI, Sikes KJ, Jiang Z, Klima M, Fudenberg G, Hone J, et al. Ultrahigh electron mobility in suspended graphene. Solid State Commun. 2008;146:351–5.

6. Zhu Y, Murali S, Cai W, Li X, Suk JW, Potts JR, et al. Graphene and Graphene Oxide: Synthesis, Properties, and Applications. Adv Mater. 2010;22:3906–24.

7. Li X, Cai W, An J, Kim S, Nah J, Yang D, et al. Large-area synthesis of high-quality and uniform graphene films on copper foils. science. 2009;324:1312–4.

8. Viculis LM, Mack JJ, Kaner RB. A Chemical Route to Carbon Nanoscrolls. Science. 2003;299:1361–1361.

9. Novoselov KS, Jiang D, Schedin F, Booth TJ, Khotkevich VV, Morozov SV, et al. Two-dimensional atomic crystals. Proc Natl Acad Sci. 2005;102:10451–3.

10. Ayari A, Cobas E, Ogundadegbe O, Fuhrer MS. Realization and electrical characterization of ultrathin crystals of layered transition-metal dichalcogenides. J Appl Phys. 2007;101:014507.

11. Ohta T, Bostwick A, Seyller T, Horn K, Rotenberg E. Controlling the electronic structure of bilayer graphene. Science. 2006;313:951–4.

12. Treier M, Pignedoli CA, Laino T, Rieger R, Müllen K, Passerone D, et al. Surface-assisted cyclodehydrogenation provides a synthetic route towards easily processable and chemically tailored nanographenes. Nat Chem. 2011;3:61.

13. Cai J, Ruffieux P, Jaafar R, Bieri M, Braun T, Blankenburg S, et al. Atomically precise bottom-up fabrication of graphene nanoribbons. Nature. 2010;466:470.

14. Tomović Ž, Watson MD, Müllen K. Superphenalene-based columnar liquid crystals. Angew Chem Int Ed. 2004;43:755–8.

15. Gilje S, Han S, Wang M, Wang KL, Kaner RB. A Chemical Route to Graphene for Device Applications. Nano Lett. 2007;7:3394–8.

16. Stankovich S, Dikin DA, Piner RD, Kohlhaas KA, Kleinhammes A, Jia Y, et al. Synthesis of graphene-based nanosheets via chemical reduction of exfoliated graphite oxide. Carbon. 2007;45:1558–65.

17. Shin Y-R, Jung S-M, Jeon I-Y, Baek J-B. The oxidation mechanism of highly ordered pyrolytic graphite in a nitric acid/sulfuric acid mixture. Carbon. 2013;52:493–498.

18. Shahriary L, Athawale AA. Graphene Oxide Synthesized by using Modified Hummers Approach. 2014;02:6.

19. Lu L, Zeng C, Wang L, Yin X, Jin S, Lu A, et al. Graphene oxide and H2 production from bioelectrochemical graphite oxidation. Sci Rep [Internet]. 2015 [cited 2019 Feb 8];5. Available from: http://www.nature.com/articles/srep16242

20. Graphene Market 2018 Global Analysis, Industry Demand, Trends, Size, Opportunities, Forecast 2023 - MarketWatch [Internet]. [cited 2019 Jul 3]. Available from: https://www.marketwatch.com/press-release/graphene-market-2018-global-analysis-industry-demand-trends-size-opportunities-forecast-2023-2018-08-31

21. Graphene Market Size & Share | Industry Growth Analysis Report, 2025 [Internet]. Gd. View Res. [cited 2019 Jun 5]. Available from: https://www.grandviewresearch.com/industry-analysis/graphene-industry

22. Gao W. Graphene oxide: reduction recipes, spectroscopy, and applications. Springer; 2015.

23. Geim AK. Graphene: Status and Prospects. Science. 2009;324:1530–4.

24. Wei J, Qiu J, Li L, Ren L, Zhang X, Chaudhuri J, et al. A reduced graphene oxide based electrochemical biosensor for tyrosine detection. Nanotechnology. 2012;23:335707.

25. Roldán R, Chirolli L, Prada E, Silva-Guillén JA, San-Jose P, Guinea F. Theory of 2D crystals: graphene and beyond. Chem Soc Rev. 2017;46:4387–99.

26. Boukhvalov DW, Katsnelson MI. Modeling of Graphite Oxide. J Am Chem Soc. 2008;130:10697–701.

27. Yan J-A, Xian L, Chou MY. Structural and Electronic Properties of Oxidized Graphene. Phys Rev Lett [Internet]. 2009 [cited 2019 Feb 12];103. Available from: https://link.aps.org/doi/10.1103/PhysRevLett.103.086802

28. Yan J-A, Chou MY. Oxidation functional groups on graphene: Structural and electronic properties. Phys Rev B [Internet]. 2010 [cited 2019 Feb 12];82. Available from: https://link.aps.org/doi/10.1103/PhysRevB.82.125403

29. Wang L, Lee K, Sun Y-Y, Lucking M, Chen Z, Zhao JJ, et al. Graphene Oxide as an Ideal Substrate for Hydrogen Storage. ACS Nano. 2009;3:2995–3000.

30. Wang L, Sun YY, Lee K, West D, Chen ZF, Zhao JJ, et al. Stability of graphene oxide phases from first-principles calculations. Phys Rev B [Internet]. 2010 [cited 2019 Feb 12];82. Available from: https://link.aps.org/doi/10.1103/PhysRevB.82.161406

31. Schniepp HC, Li J-L, McAllister MJ, Sai H, Herrera-Alonso M, Adamson DH, et al. Functionalized Single Graphene Sheets Derived from Splitting Graphite Oxide. J Phys Chem B. 2006;110:8535–9.

32. Yan L, Punckt C, Aksay IA, Mertin W, Bacher G. Local Voltage Drop in a Single Functionalized Graphene Sheet Characterized by Kelvin Probe Force Microscopy. Nano Lett. 2011;11:3543–9.

33. Casabianca LB, Shaibat MA, Cai WW, Park S, Piner R, Ruoff RS, et al. NMR-Based Structural Modeling of Graphite Oxide Using Multidimensional $^{13}$ C Solid-State NMR and ab Initio Chemical Shift Calculations. J Am Chem Soc. 2010;132:5672–6.

34. Eigler S, Grimm S, Hirsch A. Investigation of the thermal stability of the carbon framework of graphene oxide. Chem Eur J. 2014;20:984–9.

35. Eigler S, Grimm S, Hof F, Hirsch A. Graphene oxide: a stable carbon framework for functionalization. J Mater Chem A. 2013;1:11559.

36. Liu L, Wang L, Gao J, Zhao J, Gao X, Chen Z. Amorphous structural models for graphene oxides. Carbon. 2012;50:1690–8.

37. Zhang Q, Scrafford K, Li M, Cao Z, Xia Z, Ajayan PM, et al. Anomalous Capacitive Behaviors of Graphene Oxide Based Solid-State Supercapacitors. Nano Lett. 2014;14:1938–43.

38. Klein CA, Cardinale GF. Young's modulus and Poisson's ratio of CVD diamond. :6.

39. Robinson JT, Zalalutdinov M, Baldwin JW, Snow ES, Wei Z, Sheehan P, et al. Wafer-scale Reduced Graphene Oxide Films for Nanomechanical Devices. Nano Lett. 2008;8:3441–5.

40. Gómez-Navarro C, Burghard M, Kern K. Elastic Properties of Chemically Derived Single Graphene Sheets. Nano Lett. 2008;8:2045–9.

41. Suk JW, Piner RD, An J, Ruoff RS. Mechanical Properties of Monolayer Graphene Oxide. ACS Nano. 2010;4:6557–64.

42. Park S, Lee K-S, Bozoklu G, Cai W, Nguyen ST, Ruoff RS. Graphene oxide papers modified by divalent ions—enhancing mechanical properties via chemical cross-linking. ACS Nano. 2008;2:572–8.

43. Rogala M, Wlasny I, Dabrowski P, Kowalczyk PJ, Busiakiewicz A, Kozlowski W, et al. Graphene oxide overprints for flexible and transparent electronics. Appl Phys Lett. 2015;106:041901.

44. Eda G, Fanchini G, Chhowalla M. Large-area ultrathin films of reduced graphene oxide as a transparent and flexible electronic material. Nat Nanotechnol. 2008;3:270–4.

45. Eda G, Lin Y-Y, Miller S, Chen C-W, Su W-F, Chhowalla M. Transparent and conducting electrodes for organic electronics from reduced graphene oxide. Appl Phys Lett. 2008;92:233305.

46. Becerril HA, Mao J, Liu Z, Stoltenberg RM, Bao Z, Chen Y. Evaluation of Solution-Processed Reduced Graphene Oxide Films as Transparent Conductors. ACS Nano. 2008;2:463–70.

47. Li X, Zhang G, Bai X, Sun X, Wang X, Wang E, et al. Highly conducting graphene sheets and Langmuir–Blodgett films. Nat Nanotechnol. 2008;3:538–42.

48. Nourbakhsh A, Cantoro M, Vosch T, Pourtois G, Clemente F, van der Veen MH, et al. Bandgap opening in oxygen plasma-treated graphene. Nanotechnology. 2010;21:435203.

49. Zhu Y, Cai W, Piner RD, Velamakanni A, Ruoff RS. Transparent self-assembled films of reduced graphene oxide platelets. Appl Phys Lett. 2009;95:103104.

50. Loh KP, Bao Q, Eda G, Chhowalla M. Graphene oxide as a chemically tunable platform for optical applications. Nat Chem. 2010;2:1015–24.

51. Eda G, Chhowalla M. Chemically Derived Graphene Oxide: Towards Large-Area Thin-Film Electronics and Optoelectronics. Adv Mater. 2010;22:2392–415.

52. Essig S, Marquardt CW, Vijayaraghavan A, Ganzhorn M, Dehm S, Hennrich F, et al. Phonon-assisted electroluminescence from metallic carbon nanotubes and graphene. Nano Lett. 2010;10:1589–94.

53. Luo Z, Vora PM, Mele EJ, Johnson ATC, Kikkawa JM. Photoluminescence and band gap modulation in graphene oxide. Appl Phys Lett. 2009;94:111909.

54. Low CTJ, Walsh FC, Chakrabarti MH, Hashim MA, Hussain MA. Electrochemical approaches to the production of graphene flakes and their potential applications. Carbon. 2013;54:1–21.

55. Dreyer DR, Park S, Bielawski CW, Ruoff RS. The chemistry of graphene oxide. Chem Soc Rev. 2010;39:228–40.

56. Chua CK, Pumera M. Chemical reduction of graphene oxide: a synthetic chemistry viewpoint. Chem Soc Rev. 2014;43:291–312.

57. Staudenmaier L. Verfahren zur Darstellung der Graphitsäure. Berichte Dtsch Chem Ges. 1898;31:1481–7.

58. Hummers WS, Offeman RE. Preparation of Graphitic Oxide. J Am Chem Soc. 1958;80:1339–1339.

59. Marcano DC, Kosynkin DV, Berlin JM, Sinitskii A, Sun Z, Slesarev A, et al. Improved Synthesis of Graphene Oxide. ACS Nano. 2010;4:4806–14.

60. Alanyalıoğlu M, Segura JJ, Oró-Solè J, Casañ-Pastor N. The synthesis of graphene sheets with controlled thickness and order using surfactant-assisted electrochemical processes. Carbon. 2012;50:142–52.

61. Morales GM, Schifani P, Ellis G, Ballesteros C, Martínez G, Barbero C, et al. High-quality few layer graphene produced by electrochemical intercalation and microwave-assisted expansion of graphite. Carbon. 2011;49:2809–16.

62. Dimiev AM, Tour JM. Mechanism of Graphene Oxide Formation. ACS Nano. 2014;8:3060–8.

63. Wang G, Wang B, Park J, Wang Y, Sun B, Yao J. Highly efficient and large-scale synthesis of graphene by electrolytic exfoliation. Carbon. 2009;47:3242–3246.

64. Hathcock KW, Brumfield JC, Goss CA, Irene EA, Murray RW. Incipient Electrochemical Oxidation of Highly Oriented Pyrolytic Graphite: Correlation between Surface Blistering and Electrolyte Anion Intercalation. Anal Chem. 1995;67:2201–6.

65. Bourelle E, Claude-Montigny B, Metrot A. Electrochemical exfoliation of HOPG in formic-sulfuric acid mixtures. Mol Cryst Liq Cryst Sci Technol Sect Mol Cryst Liq Cryst. 1998;310:321–326.

66. Dilimon VS, Sampath S. Electrochemical preparation of few layer-graphene nanosheets via reduction of oriented exfoliated graphene oxide thin films in acetamide–urea–ammonium nitrate melt under ambient conditions. Thin Solid Films. 2011;519:2323–2327.

67. You X, Chang J-H, Ju BK, Pak JJ. An electrochemical route to graphene oxide. J Nanosci Nanotechnol. 2011;11:5965–5968.

68. Sima M, Enculescu I, Sima A. Preparation of graphene and its application in dye-sensitized solar cells. Optoelectron Adv Mater. 2011;5:414–418.

69. Pei S, Cheng H-M. The reduction of graphene oxide. Carbon. 2012;50:3210–28.

70. Mattevi C, Eda G, Agnoli S, Miller S, Mkhoyan KA, Celik O, et al. Evolution of Electrical, Chemical, and Structural Properties of Transparent and Conducting Chemically Derived Graphene Thin Films. Adv Funct Mater. 2009;19:2577–83.

71. Gao W, Alemany LB, Ci L, Ajayan PM. New insights into the structure and reduction of graphite oxide. Nat Chem. 2009;1:403–8.

72. Yang D, Velamakanni A, Bozoklu G, Park S, Stoller M, Piner RD, et al. Chemical analysis of graphene oxide films after heat and chemical treatments by X-ray photoelectron and Micro-Raman spectroscopy. Carbon. 2009;47:145–52.

73. Zhu Y, Murali S, Stoller MD, Velamakanni A, Piner RD, Ruoff RS. Microwave assisted exfoliation and reduction of graphite oxide for ultracapacitors. Carbon. 2010;48:2118–22.

74. Hassan HMA, Abdelsayed V, Khder AERS, AbouZeid KM, Terner J, El-Shall MS, et al. Microwave synthesis of graphene sheets supporting metal nanocrystals in aqueous and organic media. J Mater Chem. 2009;19:3832.

75. Cote LJ, Kim F, Huang J. Langmuir−Blodgett Assembly of Graphite Oxide Single Layers. J Am Chem Soc. 2009;131:1043–9.

76. Zhang Y, Guo L, Wei S, He Y, Xia H, Chen Q, et al. Direct imprinting of microcircuits on graphene oxides film by femtosecond laser reduction. Nano Today. 2010;5:15–20.

77. Baraket M, Walton SG, Wei Z, Lock EH, Robinson JT, Sheehan P. Reduction of graphene oxide by electron beam generated plasmas produced in methane/argon mixtures. Carbon. 2010;48:3382–90.

78. Guo Y, Wu B, Liu H, Ma Y, Yang Y, Zheng J, et al. Electrical Assembly and Reduction of Graphene Oxide in a Single Solution Step for Use in Flexible Sensors. Adv Mater. 2011;23:4626–30.

79. Wang X, Zhi L, Müllen K. Transparent, Conductive Graphene Electrodes for Dye-Sensitized Solar Cells. Nano Lett. 2008;8:323–7.

80. Pei S, Zhao J, Du J, Ren W, Cheng H-M. Direct reduction of graphene oxide films into highly conductive and flexible graphene films by hydrohalic acids. Carbon. 2010;48:4466–74.

81. Moon IK, Lee J, Ruoff RS, Lee H. Reduced graphene oxide by chemical graphitization. Nat Commun. 2010;1:73.

82. Fernández-Merino MJ, Guardia L, Paredes JI, Villar-Rodil S, Solís-Fernández P, Martínez-Alonso A, et al. Vitamin C Is an Ideal Substitute for Hydrazine in the Reduction of Graphene Oxide Suspensions. J Phys Chem C. 2010;114:6426–32.

83. Wang G, Yang J, Park J, Gou X, Wang B, Liu H, et al. Facile Synthesis and Characterization of Graphene Nanosheets. J Phys Chem C. 2008;112:8192–5.

84. Zhou X, Zhang J, Wu H, Yang H, Zhang J, Guo S. Reducing Graphene Oxide via Hydroxylamine: A Simple and Efficient Route to Graphene. J Phys Chem C. 2011;115:11957–61.

85. Mao S, Pu H, Chen J. Graphene oxide and its reduction: modeling and experimental progress. RSC Adv. 2012;2:2643.

86. Su Y, Gao X, Zhao J. Reaction mechanisms of graphene oxide chemical reduction by sulfur-containing compounds. Carbon. 2014;67:146–55.

87. Pacilé D, Meyer JC, Fraile Rodríguez A, Papagno M, Gómez-Navarro C, Sundaram RS, et al. Electronic properties and atomic structure of graphene oxide membranes. Carbon. 2011;49:966–72.

88. Alcalde H, Fuente J de la, Kamp B, Zurutuza A. Market Uptake Potential of Graphene as a Disruptive Material. Proc IEEE. 2013;101:1793–800.

89. Wu J, Becerril HA, Bao Z, Liu Z, Chen Y, Peumans P. Organic solar cells with solution-processed graphene transparent electrodes. Appl Phys Lett. 2008;92:263302.

90. Wu J, Agrawal M, Becerril HA, Bao Z, Liu Z, Chen Y, et al. Organic Light-Emitting Diodes on Solution-Processed Graphene Transparent Electrodes. ACS Nano. 2010;4:43–8.

91. Wassei JK, Kaner RB. Graphene, a promising transparent conductor. Mater Today. 2010;13:52–9.

92. Zhou G, Li F, Cheng H-M. Progress in flexible lithium batteries and future prospects. Energy Env Sci. 2014;7:1307–38.

93. Yamaguchi H, Murakami K, Eda G, Fujita T, Guan P, Wang W, et al. Field emission from atomically thin edges of reduced graphene oxide. ACS Nano. 2011;5:4945–52.

94. Huang J, Zhang L, Chen B, Ji N, Chen F, Zhang Y, et al. Nanocomposites of size-controlled gold nanoparticles and graphene oxide: Formation and applications in SERS and catalysis. Nanoscale. 2010;2:2733.

95. Kagan MR, McCreery RL. Reduction of Fluorescence Interference in Raman Spectroscopy via Analyte Adsorption on Graphitic Carbon. Anal Chem. 1994;66:4159–65.

96. Jiang X-F, Polavarapu L, Neo ST, Venkatesan T, Xu Q-H. Graphene Oxides as Tunable Broadband Nonlinear Optical Materials for Femtosecond Laser Pulses. J Phys Chem Lett. 2012;3:785–90.

97. Chen Z, Lin Y-M, Rooks MJ, Avouris P. Graphene nano-ribbon electronics. Phys E Low-Dimens Syst Nanostructures. 2007;40:228–32.

98. Yeh T-F, Chen S-J, Yeh C-S, Teng H. Tuning the Electronic Structure of Graphite Oxide through Ammonia Treatment for Photocatalytic Generation of $H_2$ and $O_2$ from Water Splitting. J Phys Chem C. 2013;117:6516–24.

99. Kudo A, Miseki Y. Heterogeneous photocatalyst materials for water splitting. Chem Soc Rev. 2009;38:253–278.

100. Yeh T-F, Syu J-M, Cheng C, Chang T-H, Teng H. Graphite Oxide as a Photocatalyst for Hydrogen Production from Water. Adv Funct Mater. 2010;20:2255–62.

101. Yeh T-F, Teng H. Graphite Oxide with Different Oxygen Contents as Photocatalysts for Hydrogen and Oxygen Evolution from Water. ECS Trans. 2012;41:7–26.

102. Yeh T-F, Teng C-Y, Chen S-J, Teng H. Nitrogen-doped graphene oxide quantum dots as photocatalysts for overall water-splitting under visible light Illumination. Adv Mater. 2014;26:3297–3303.

103. An X, Yu JC. Graphene-based photocatalytic composites. RSC Adv. 2011;1:1426.

104. Osterloh FE. Inorganic Materials as Catalysts for Photochemical Splitting of Water. Chem Mater. 2008;20:35–54.

105. Li F, Jiang X, Zhao J, Zhang S. Graphene oxide: A promising nanomaterial for energy and environmental applications. Nano Energy. 2015;16:488–515.

106. Kim JM, Hong WG, Lee SM, Chang SJ, Jun Y, Kim BH, et al. Energy storage of thermally reduced graphene oxide. Int J Hydrog Energy. 2014;39:3799–804.

107. Tylianakis E, Psofogiannakis GM, Froudakis GE. Li-doped pillared graphene oxide: a graphene-based nanostructured material for hydrogen storage. J Phys Chem Lett. 2010;1:2459–2464.

108. Zabihinpour M, Ghenaatian HR. A novel multilayered architecture of graphene oxide nanosheets for high supercapacitive performance electrode material. Synth Met. 2013;175:62–7.

109. Shulga YM, Baskakov SA, Smirnov VA, Shulga NY, Belay KG, Gutsev GL. Graphene oxide films as separators of polyaniline-based supercapacitors. J Power Sources. 2014;245:33–6.

110. Lin Z, Liu Y, Yao Y, Hildreth OJ, Li Z, Moon K, et al. Superior capacitance of functionalized graphene. J Phys Chem C. 2011;115:7120–7125.

111. Zhang J, Cao H, Tang X, Fan W, Peng G, Qu M. Graphite/graphene oxide composite as high capacity and binder-free anode material for lithium ion batteries. J Power Sources. 2013;241:619–26.

112. Yamin H, Peled E. Electrochemistry of a nonaqueous lithium/sulfur cell. J Power Sources. 1983;9:281–7.

113. Yang X, He P, Xia Y. Preparation of mesocellular carbon foam and its application for lithium/oxygen battery. Electrochem Commun. 2009;11:1127–30.

114. Kim D, Kim DW, Lim H-K, Jeon J, Kim H, Jung H-T, et al. Intercalation of Gas Molecules in Graphene Oxide Interlayer: The Role of Water. J Phys Chem C. 2014;118:11142–8.

115. Christian Kemp K, Chandra V, Saleh M, Kim KS. Reversible CO $_2$ adsorption by an activated nitrogen doped graphene/polyaniline material. Nanotechnology. 2013;24:235703.

116. Saleh M, Chandra V, Christian Kemp K, Kim KS. Synthesis of N-doped microporous carbon via chemical activation of polyindole-modified graphene oxide sheets for selective carbon dioxide adsorption. Nanotechnology. 2013;24:255702.

117. Alhwaige AA, Agag T, Ishida H, Qutubuddin S. Biobased chitosan hybrid aerogels with superior adsorption: Role of graphene oxide in CO2 capture. RSC Adv. 2013;3:16011.

118. Tang S, Cao Z. Adsorption and Dissociation of Ammonia on Graphene Oxides: A First-Principles Study. J Phys Chem C. 2012;116:8778–91.

119. He Y, Zhang N, Wu F, Xu F, Liu Y, Gao J. Graphene oxide foams and their excellent adsorption ability for acetone gas. Mater Res Bull. 2013;48:3553–8.

120. Matsuo Y, Nishino Y, Fukutsuka T, Sugie Y. Removal of formaldehyde from gas phase by silylated graphite oxide containing amino groups. Carbon. 2008;46:1162–3.

121. Huang L, Seredych M, Bandosz TJ, Van Duin AC, Lu X, Gubbins KE. Controllable atomistic graphene oxide model and its application in hydrogen sulfide removal. J Chem Phys. 2013;139:194707.

122. Seredych M, Bandosz TJ. Effects of Surface Features on Adsorption of SO $_2$ on Graphite Oxide/Zr(OH) $_4$ Composites. J Phys Chem C. 2010;114:14552–60.

123. Wang L, Zhao J, Wang L, Yan T, Sun Y-Y, Zhang SB. Titanium-decorated graphene oxide for carbon monoxide capture and separation. Phys Chem Chem Phys. 2011;13:21126.

124. Chen C, Xu K, Ji X, Miao L, Jiang J. Enhanced adsorption of acidic gases (CO 2 , NO 2 and SO 2 ) on light metal decorated graphene oxide. Phys Chem Chem Phys. 2014;16:11031–6.

125. Ma H-L, Zhang Y, Hu Q-H, Yan D, Yu Z-Z, Zhai M. Chemical reduction and removal of Cr(vi) from acidic aqueous solution by ethylenediamine-reduced graphene oxide. J Mater Chem. 2012;22:5914.

126. Zhao G, Ren X, Gao X, Tan X, Li J, Chen C, et al. Removal of Pb(ii) ions from aqueous solutions on few-layered graphene oxide nanosheets. Dalton Trans. 2011;40:10945.

127. Chandra V, Kim KS. Highly selective adsorption of Hg2+ by a polypyrrole–reduced graphene oxide composite. Chem Commun. 2011;47:3942.

128. Zhou L, Gao C, Xu W. Magnetic Dendritic Materials for Highly Efficient Adsorption of Dyes and Drugs. ACS Appl Mater Interfaces. 2010;2:1483–91.

129. He F, Niu N, Qu F, Wei S, Chen Y, Gai S, et al. Synthesis of three-dimensional reduced graphene oxide layer supported cobalt nanocrystals and their high catalytic activity in F–T CO2 hydrogenation. Nanoscale. 2013;5:8507.

130. An X, Li K, Tang J. Cu2O/Reduced Graphene Oxide Composites for the Photocatalytic Conversion of CO2. ChemSusChem. 2014;7:1086–93.

131. Hsu H-C, Shown I, Wei H-Y, Chang Y-C, Du H-Y, Lin Y-G, et al. Graphene oxide as a promising photocatalyst for $CO_2$ to methanol conversion. Nanoscale. 2013;5:262–8.

132. Cheng J, Zhang M, Wu G, Wang X, Zhou J, Cen K. Photoelectrocatalytic reduction of CO2 into chemicals using Pt-modified reduced graphene oxide combined with Pt-modified TiO2 nanotubes. Environ Sci Technol. 2014;48:7076–7084.

133. Long Y, Zhang C, Wang X, Gao J, Wang W, Liu Y. Oxidation of SO 2 to SO 3 catalyzed by graphene oxide foams. J Mater Chem. 2011;21:13934–13941.

134. Nie R, Shi J, Xia S, Shen L, Chen P, Hou Z, et al. MnO 2/graphene oxide: a highly active catalyst for amide synthesis from alcohols and ammonia in aqueous media. J Mater Chem. 2012;22:18115–18118.

135. Fu H, Zhu D. Graphene Oxide-Facilitated Reduction of Nitrobenzene in Sulfide-Containing Aqueous Solutions. Environ Sci Technol. 2013;47:4204–10.

136. Shi P, Su R, Zhu S, Zhu M, Li D, Xu S. Supported cobalt oxide on graphene oxide: Highly efficient catalysts for the removal of Orange II from water. J Hazard Mater. 2012;229–230:331–9.

137. Zhang Z, Hao J, Yang W, Lu B, Ke X, Zhang B, et al. Porous Co3O4 Nanorods–Reduced Graphene Oxide with Intrinsic Peroxidase-Like Activity and Catalysis in the Degradation of Methylene Blue. ACS Appl Mater Interfaces. 2013;5:3809–15.

138. Kotchey GP, Allen BL, Vedala H, Yanamala N, Kapralov AA, Tyurina YY, et al. The Enzymatic Oxidation of Graphene Oxide. ACS Nano. 2011;5:2098–108.

139. Chen C, Xie Q, Yang D, Xiao H, Fu Y, Tan Y, et al. Recent advances in electrochemical glucose biosensors: a review. RSC Adv. 2013;3:4473.

140. Shao Y, Wang J, Wu H, Liu J, Aksay IA, Lin Y. Graphene Based Electrochemical Sensors and Biosensors: A Review. Electroanalysis. 2010;22:1027–36.

141. Zhou M, Zhai Y, Dong S. Electrochemical Sensing and Biosensing Platform Based on Chemically Reduced Graphene Oxide. Anal Chem. 2009;81:5603–13.

142. Zhang M, Yin B-C, Tan W, Ye B-C. A versatile graphene-based fluorescence “on/off” switch for multiplex detection of various targets. Biosens Bioelectron. 2011;26:3260–3265.

143. Jung JH, Cheon DS, Liu F, Lee KB, Seo TS. A Graphene Oxide Based Immuno-biosensor for Pathogen Detection. Angew Chem. 2010;122:5844–7.

144. Liu F, Choi JY, Seo TS. Graphene oxide arrays for detecting specific DNA hybridization by fluorescence resonance energy transfer. Biosens Bioelectron. 2010;25:2361–5.

145. Liu M, Zhao H, Quan X, Chen S, Fan X. Distance-independent quenching of quantum dots by nanoscale-graphene in self-assembled sandwich immunoassay. Chem Commun. 2010;46:7909.

146. Ping J, Wang Y, Fan K, Wu J, Ying Y. Direct electrochemical reduction of graphene oxide on ionic liquid doped screen-printed electrode and its electrochemical biosensing application. Biosens Bioelectron. 2011;28:204–9.

147. Rabaey K, Rozendal RA. Microbial electrosynthesis — revisiting the electrical route for microbial production. Nat Rev Microbiol. 2010;8:706–16.

148. Thrash JC, Coates JD. Review: Direct and Indirect Electrical Stimulation of Microbial Metabolism. Environ Sci Technol. 2008;42:3921–31.

149. Kato Marcus A, Torres CI, Rittmann BE. Conduction-based modeling of the biofilm anode of a microbial fuel cell. Biotechnol Bioeng. 2007;98:1171–82.

150. Zhu C, Hao Q, Huang Y, Yang J, Sun D. Microbial oxidation of dispersed graphite by nitrifying bacteria 2011.2. Nanoscale. 2013;5:8982–8985.

151. Zhu C, Liu L, Fan M, Liu L, Dai B, Yang J, et al. Microbial oxidation of graphite by Acidithiobacillus ferrooxidans CFMI-1. RSC Adv. 2014;4:55044–55047.

152. Yang S, Lohe MR, Müllen K, Feng X. New-Generation Graphene from Electrochemical Approaches: Production and Applications. Adv Mater. 2016;28:6213–21.

153. Su C-Y, Lu A-Y, Xu Y, Chen F-R, Khlobystov AN, Li L-J. High-quality thin graphene films from fast electrochemical exfoliation. ACS Nano. 2011;5:2332–2339.

154. Christodoulou X, Okoroafor T, Parry S, Velasquez-Orta SB. The use of carbon dioxide in microbial electrosynthesis: Advancements, sustainability and economic feasibility. J CO2 Util. 2017;18:390–9.

155. Balch WE, Fox GE, Magrum LJ, Woese CR, Wolfe RS. Methanogens: reevaluation of a unique biological group. Microbiol Rev. 1979;43:260.

156. Mourdikoudis S, Pallares RM, Thanh NTK. Characterization techniques for nanoparticles: comparison and complementarity upon studying nanoparticle properties. Nanoscale. 2018;10:12871–934.

157. Park CM, Wang D, Heo J, Her N, Su C. Aggregation of reduced graphene oxide and its nanohybrids with magnetite and elemental silver under environmentally relevant conditions. J Nanoparticle Res. 2018;20:93.

158. Wang M, Niu Y, Zhou J, Wen H, Zhang Z, Luo D, et al. The dispersion and aggregation of graphene oxide in aqueous media. Nanoscale. 2016;8:14587–92.

159. Tang H, Zhao Y, Yang X, Liu D, Shao P, Zhu Z, et al. New Insight into the Aggregation of Graphene Oxide Using Molecular Dynamics Simulations and Extended Derjaguin–Landau–Verwey–Overbeek Theory. Environ Sci Technol. 2017;51:9674–82.

160. Shen M, Hai X, Shang Y, Zheng C, Li P, Li Y, et al. Insights into aggregation and transport of graphene oxide in aqueous and saturated porous media: Complex effects of cations with different molecular weight fractionated natural organic matter. Sci Total Environ. 2019;656:843–51.

161. Chowdhury I, Mansukhani ND, Guiney LM, Hersam MC, Bouchard D. Aggregation and Stability of Reduced Graphene Oxide: Complex Roles of Divalent Cations, pH, and Natural Organic Matter. Environ Sci Technol. 2015;49:10886–93.

162. Lai Q, Zhu S, Luo X, Zou M, Huang S. Ultraviolet-visible spectroscopy of graphene oxides. AIP Adv. 2012;2:032146.

163. Rattana, Chaiyakun S, Witit-anun N, Nuntawong N, Chindaudom P, Oaew S, et al. Preparation and characterization of graphene oxide nanosheets. Procedia Eng. 2012;32:759–64.

164. Wang X, Dou W. Preparation of graphite oxide (GO) and the thermal stability of silicone rubber/GO nanocomposites. Thermochim Acta. 2012;529:25–8.

165. Khan M, Al-Marri AH, Khan M, Mohri N, Adil SF, Al-Warthan A, et al. Pulicaria glutinosa plant extract: a green and eco-friendly reducing agent for the preparation of highly reduced graphene oxide. RSC Adv. 2014;4:24119–24125.

166. Park S, An J, Potts JR, Velamakanni A, Murali S, Ruoff RS. Hydrazine-reduction of graphite- and graphene oxide. Carbon. 2011;49:3019–23.

167. Jiang K-C, Xin S, Lee J-S, Kim J, Xiao X-L, Guo Y-G. Improved kinetics of LiNi1/3Mn1/3Co1/3O2 cathode material through reduced graphene oxide networks. Phys Chem Chem Phys. 2012;14:2934.

168. Perumbilavil S, Sankar P, Priya Rose T, Philip R. White light Z-scan measurements of ultrafast optical nonlinearity in reduced graphene oxide nanosheets in the 400–700 nm region. Appl Phys Lett. 2015;107:051104.

169. Stobinski L, Lesiak B, Malolepszy A, Mazurkiewicz M, Mierzwa B, Zemek J, et al. Graphene oxide and reduced graphene oxide studied by the XRD, TEM and electron spectroscopy methods. J Electron Spectrosc Relat Phenom. 2014;195:145–54.

170. Krishnamoorthy K, Veerapandian M, Yun K, Kim S-J. The chemical and structural analysis of graphene oxide with different degrees of oxidation. Carbon. 2013;53:38–49.

171. Channu VS, Bobba R, Holze R. Graphite and graphene oxide electrodes for lithium ion batteries. Colloids Surf Physicochem Eng Asp. 2013;436:245–51.

172. Chen Y. Solid-state formation of carbon nanotubes. Carbon Nanotechnol [Internet]. Elsevier; 2006 [cited 2019 May 25]. p. 53–80. Available from: https://linkinghub.elsevier.com/retrieve/pii/B9780444518552500061

173. Grimont PAD, Grimont F. Pantoea. Bergeys Man Syst Archaea Bact [Internet]. American Cancer Society; 2015 [cited 2019 May 31]. p. 1–14. Available from: https://onlinelibrary.wiley.com/doi/abs/10.1002/9781118960608.gbm01157

174. Popa M, Măruţescu L, Ion I, Kamerzan C, Bleotu C, Oprea E, et al. Chapter 14 - Antimicrobial and cytotoxic activity of graphene-based perioceuticals. In: Grumezescu AM, editor. Fullerens Graphenes Nanotub [Internet]. William Andrew Publishing; 2018 [cited 2019 May 31]. p. 585–99. Available from: http://www.sciencedirect.com/science/article/pii/B9780128136911000142

175. Palleroni NJ. Pseudomonas. Bergeys Man Syst Archaea Bact [Internet]. American Cancer Society; 2015 [cited 2019 May 31]. p. 1–1. Available from: https://onlinelibrary.wiley.com/doi/abs/10.1002/9781118960608.gbm01210

176. Rabaey K, Boon N, Siciliano SD, Verhaege M, Verstraete W. Biofuel cells select for microbial consortia that self-mediate electron transfer. Appl Environ Microbiol. 2004;70:5373–82.

177. Wang Z, Zhou X, Zhang J, Boey F, Zhang H. Direct Electrochemical Reduction of Single-Layer Graphene Oxide and Subsequent Functionalization with Glucose Oxidase. J Phys Chem C. 2009;113:14071–5.

178. Willems A, Gillis M. Hydrogenophaga. Bergeys Man Syst Archaea Bact [Internet]. American Cancer Society; 2015 [cited 2019 May 31]. p. 1–15. Available from: https://onlinelibrary.wiley.com/doi/abs/10.1002/9781118960608.gbm00947

179. Salas EC, Sun Z, Lüttge A, Tour JM. Reduction of Graphene Oxide *via* Bacterial Respiration. ACS Nano. 2010;4:4852–6.

# APPENDIX A: EXPERIMENTAL CONDITIONS

**Experiment SSR1: Small-scale reactors - trial 1**

**Table A1:** Media recipe

**Figure A2:** Current over time for SSR1

**Figure A3: Voltage** over time for SSR1

**Figure A4:** pH over time for SSR1

**Experiment SSR2: Small-scale reactors - trial 2**

**Figure A5:** Current over time for SSR2. Poised at 1.4V

**Experiment LSR1: Large-scale reactors - trial 1**

**Figure A6:** Currents (top) and voltages (bottom) for the LSR1 over time. Lines represent changes in operating voltage as indicated on the bottom plot

**Experiment LSR2: Large-scale reactors - trial 2**

**Figure A7:** Currents over time for LSR2B (top) and LSR2A (bottom) at ~3.1V DC. On day 25 R6 was emptied and restarted on day 57 (blue line)

**Figure A8:** Voltage variations over time for LSR2B (top) and LSR2A (bottom)

**Figure A9:** pH over time for LSR2 for Biotic (top) and Abiotic (bottom) at ~3.1V DC

**Table A1:** Media recipe

| | | |
|---|---|---|
| **Media contents (1L)** | | |
| **Main contents** | | |
| Glucose | 0.36 | g |
| Na2HPO4*7H2O | 8.65 | g |
| NaH2PO4*H2O | 2.45 | g |
| NH4Cl | 0.31 | g |
| KCl | 0.13 | g |
| Trace mineral solution | 1 | mL |
| Trace vitamin solution | 1 | mL |
| **Trace mineral solution (1L in DI water)** | | |
| Dissolve nitrilotriacetic acid with KOH to pH 6.5; then proceed to add minerals. | | |
| nitriloacetic acid | 15 | g/L |
| MgSO4 | 14.63 | g/L |
| MnSO4*H2O | 4.04 | g/L |
| NaCl | 10 | g/L |
| FeSO4*7H2O | 1 | g/L |
| CoSO4*7H2O | 1.81 | g/L |
| CaCl2*2H2O | 1 | g/L |
| ZnSO4*7H2O | 1.78 | g/L |
| CuSO4*5H2O | 0.1 | g/L |
| AlK(SO4)2*12H2O | 0.18 | g/L |
| Na2MoO4*2H2O | 0.1 | g/L |
| KOH | until pH 6.5 | |
| **Trace vitamin solution (1L in DI water)** | | |
| biotin | 2 | mg/L |
| folic acid | 2 | mg/L |
| pyridoxine hydrochoride | 10 | mg/L |
| thiamine hydrochloride | 5 | mg/L |
| riboflavin | 5 | mg/L |
| nicotinic acid | 5 | mg/L |
| DL-calcium pantothenate | 5 | mg/L |
| Vitamin B12 | 0.1 | mg/L |
| p-aminobenzoic acid | 5 | mg/L |
| lipoic acid | 5 | mg/L |

**Experiment SSR1: Small-scale reactors - trial 1**

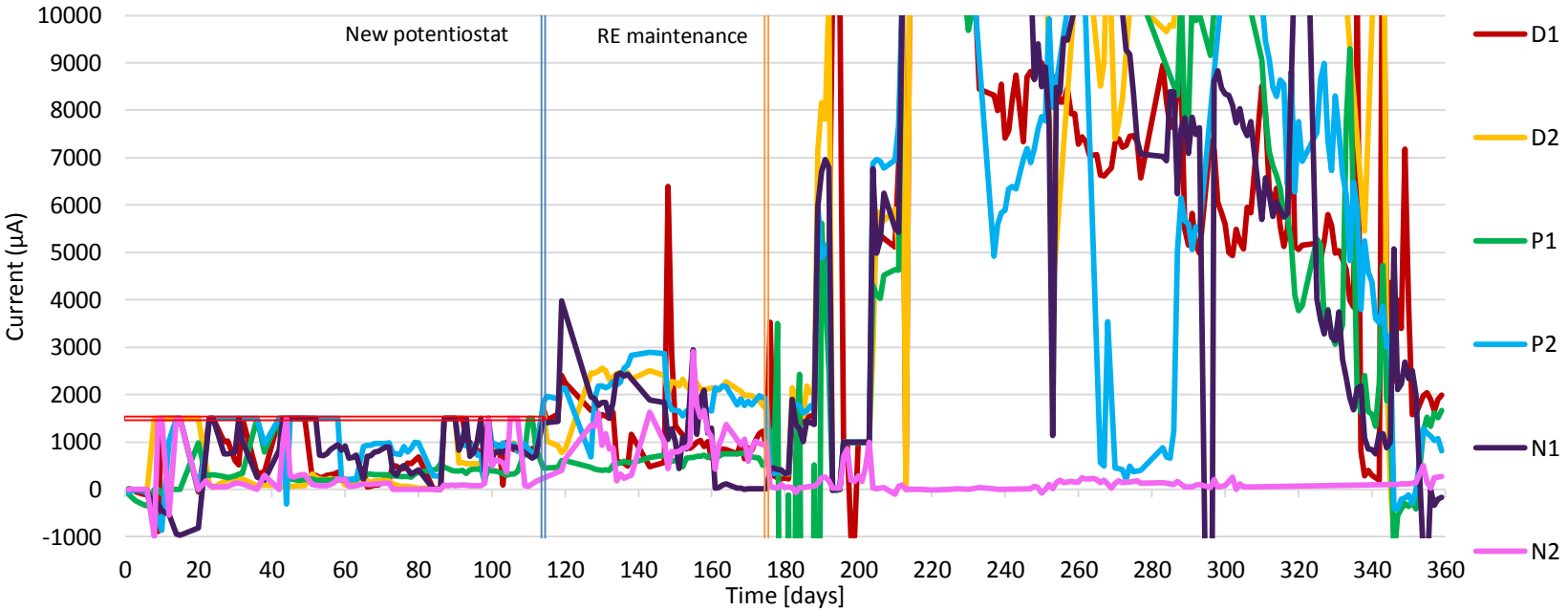


**Figure A2:** Current over time for SSR1

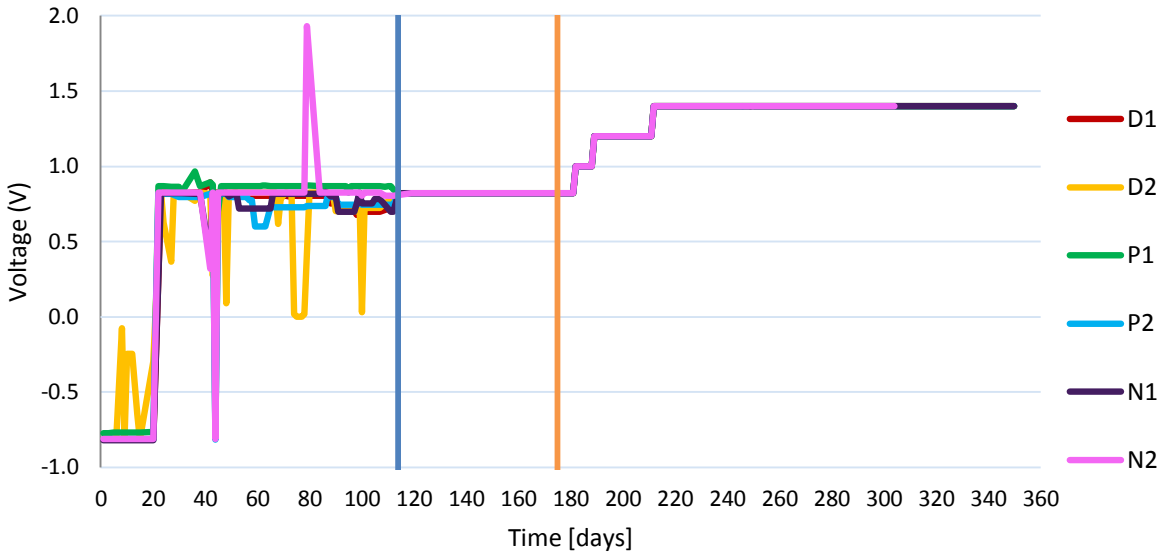


**Figure A3:** Voltage over time for SSR1.The blue line represents when the reactors were connected to the new octastat and the orange line represents replenishing of the RE solution and the beginning of the increasing voltage trial

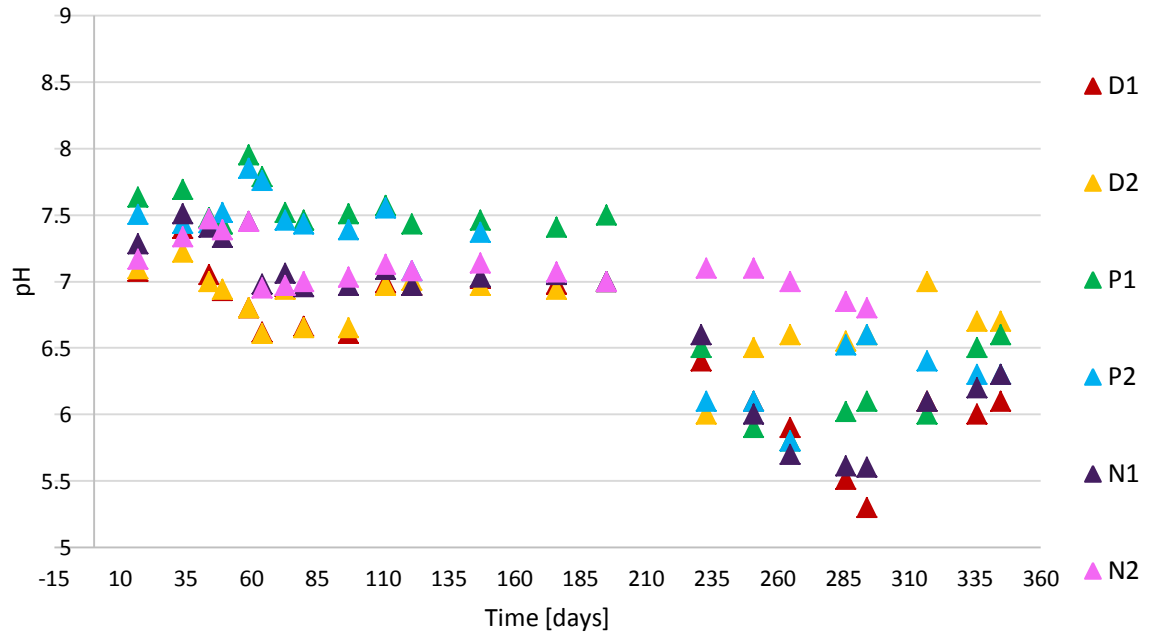


**Figure A4:** pH over time for SSR1

**Experiment SSR2: Small-scale reactors - trial 2**

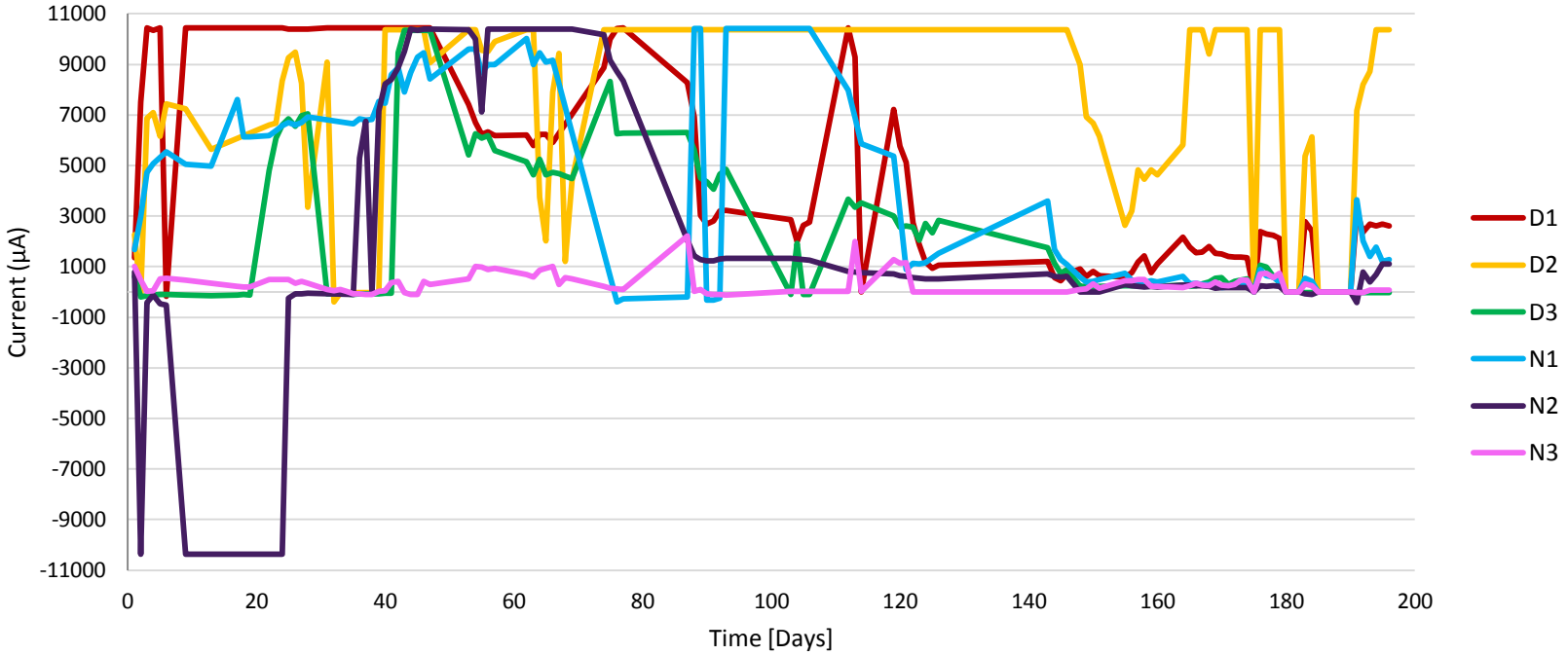


**Figure A5:** Current over time for SSR2. Poised at 1.4V

**Experiment LSR1: Large-scale reactors - trial 1**

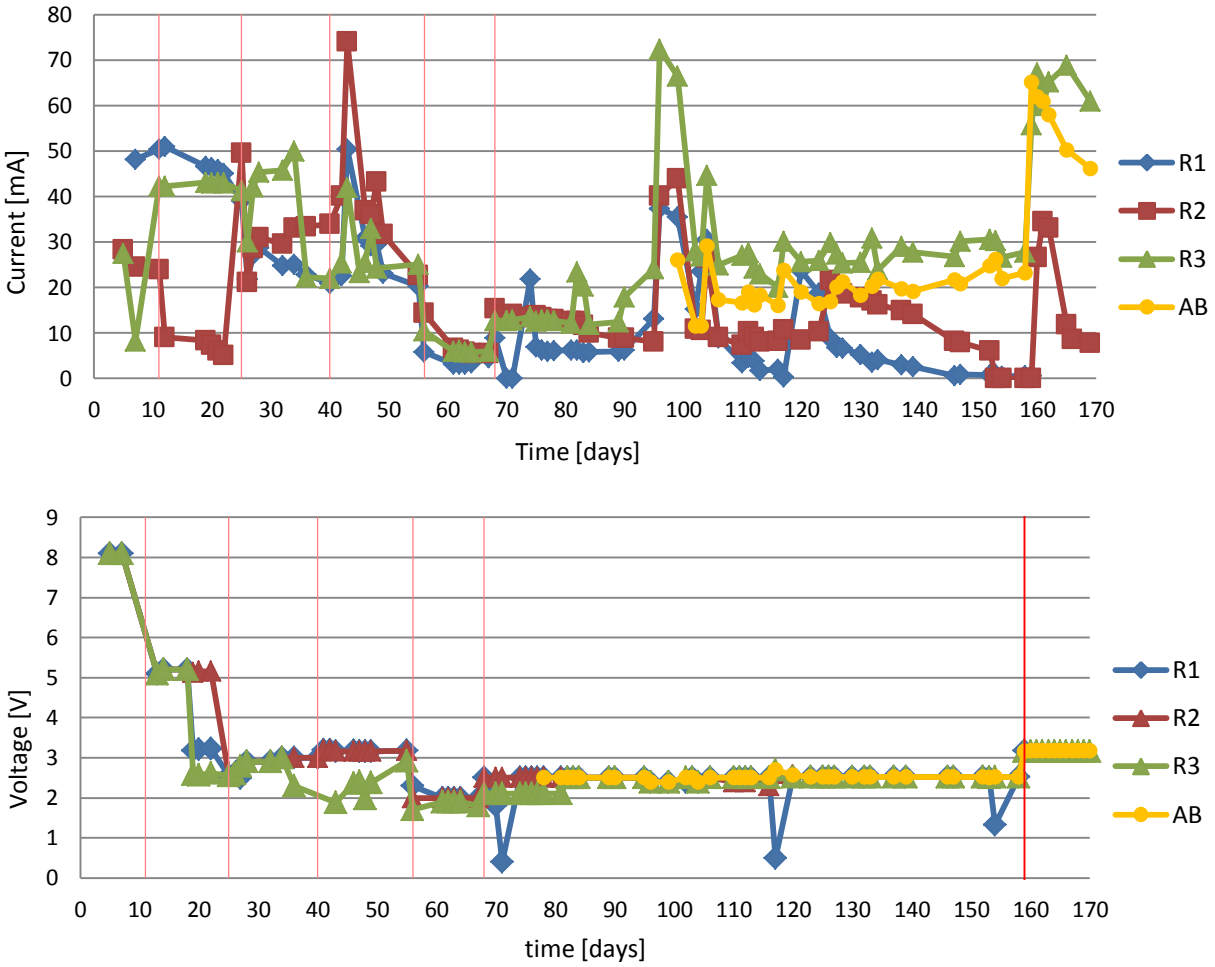


**Figure A6:** Currents (top) and voltages (bottom) for the LSR1 over time. Lines represent changes in operating voltage as indicated on the bottom plot

**Experiment LSR2: Large-scale reactors - trial 2**

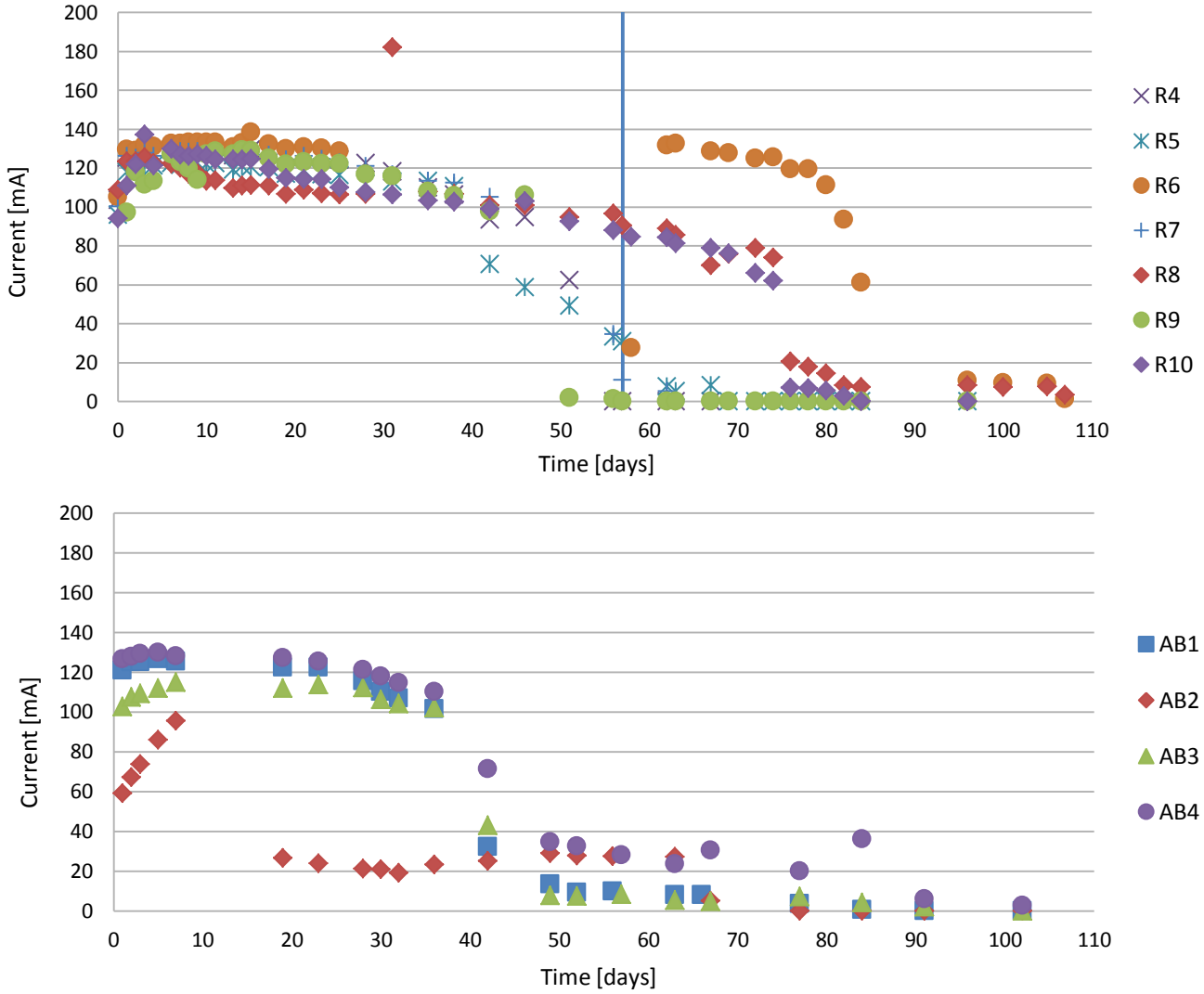


**Figure A7:** Currents over time for LSR2B (top) and LSR2A (bottom) at ~3.1V DC. On day 25 R6 was emptied and restarted on day 57 (blue line)

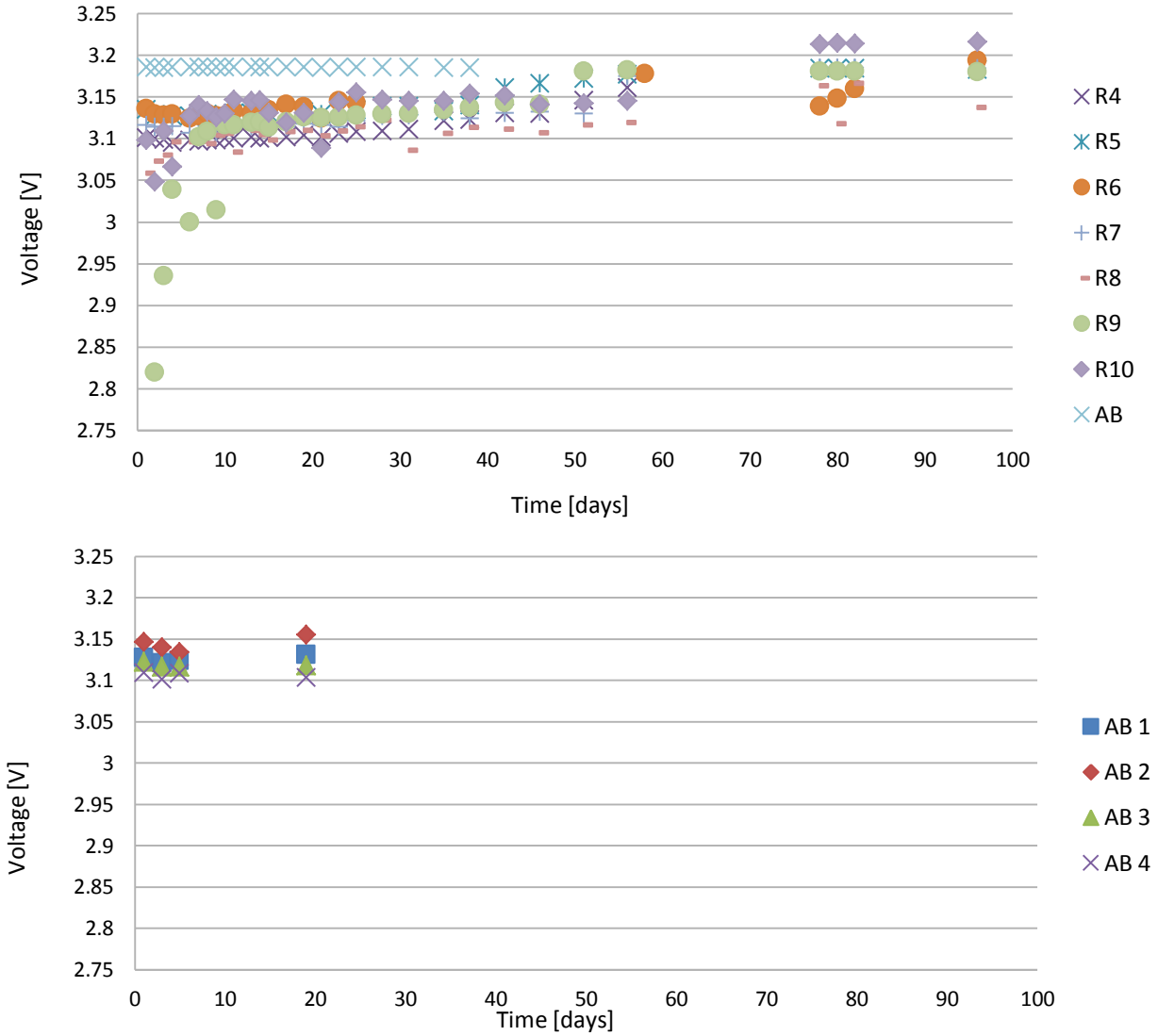


**Figure A8:** Voltage variations over time for LSR2B (top) and LSR2A (bottom)

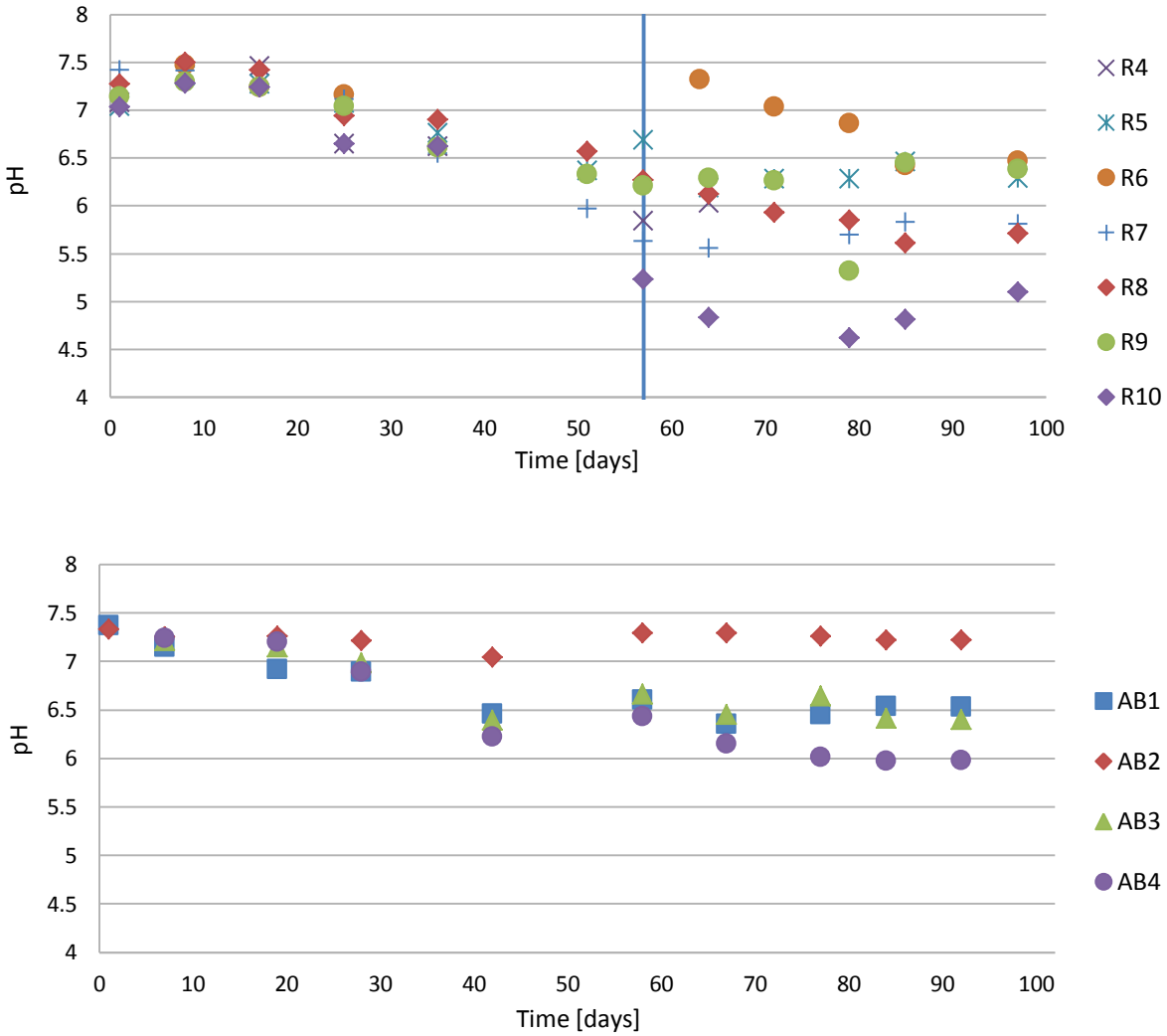


**Figure A9:** pH over time for LSR2 for Biotic (top) and Abiotic (bottom) at ~3.1V DC. On day 25 R6 was emptied and restarted on day 57 (blue line)

APPENDIX B: OTHER RESULTS AND SUPPLEMENTARY WORK

**Experiment SSR1: Small-scale reactors - trial 1**

**Figure B1:** BEGO concentrations over time using dCOD measurements for SSR1

**Figure B2:** BEGO concentrations using UV-Vis method at 229 nm (top) and 300 nm (bottom) for SSR1. After reactors were terminated on day 360, the two step-filtration protocol was conducted in the entire volume. On day 440 measurements of the permeate of the coarse filtration were performed and on day 450 measurements of the BEGO collection filter permeate were done

**Figure B3:** Total organic carbon (top) and inorganic carbon (bottom) measurements for SSR1

**Figure B4:** Reactor contents divided by upper half of the reactor volume (suspended liquid) and lower half of reactor volume (sludge and aggregates) for the SSR1 trial excluding N2

**Figure B5**: Solids on the coarse filter for all of the SSR1. These were done in separate trials to avoid clogging of the membrane

**Figure B6:** One Teflon membrane from each reactor with BEGO collected. This step was done multiple times to avoid clogging of the membrane

**Figure B7**: Permeate of the coarse filtration (C) next to the permeate of the BEGO collection filtration (B) for each reactor

**Experiment SSR2: Small-scale reactors - trial 2**

**Figure B8:** BEGO concentrations using UV-Vis method at 229 nm for the Drake (top) and New Belgium (bottom) inoculated reactors. Samples were purified using the centrifugation (C) and filtration (F) protocols for the SSR2

**Figure B9:** BEGO concentrations using UV-Vis method at 300 nm for the Drake (top) and New Belgium (bottom) inoculated reactors. Samples were purified using the centrifugation (C) and filtration (F) protocols for the SSR2

**Experiment LSR1: Large-scale reactors - trial 1**

**Figure B10:** BEGO concentrations over time using dCOD data for LSR1

**Figure B11:** BEGO concentrations over time using UV-Vis data at wavelength 229 (top) and 300 (bottom) for LSR1

**Experiment LSR2: Large-scale reactors - trial 2**

**Figure B12:** BEGO concentration over time calculated using the UV-Vis method at wavelength 229 nm for the LSR2A (top) and LSR2B (bottom). Reactor R6 was terminated on day 24 for BEGO harvesting and restarted on day 57 with new media. Reactor R4 was terminated on day 67 due to current decreasing to zero and rod samples were needed for surface chemistry analysis. All of the other reactors reached zero current at different rates (Figure A7) and were terminated on day 105 for the LSR2B and day 108 for the LSR2A

**Figure B13:** BEGO concentration over time calculated using the UV-Vis method at wavelength 300nm for the LSRB (top) and LSRA (bottom). Reactor R6 was terminated on day 24 for BEGO harvesting and restarted on day 57 with new media. Reactor R4 was terminated on day 67 due to current decreasing to zero and rod samples were needed for

surface chemistry analysis. All of the other reactors reached zero current at different rates (Figure A7) and were terminated on day 105 for the LSR2B and day 108 for the LSR2A

**Experiment SSR1: Small-scale reactors - trial 1**

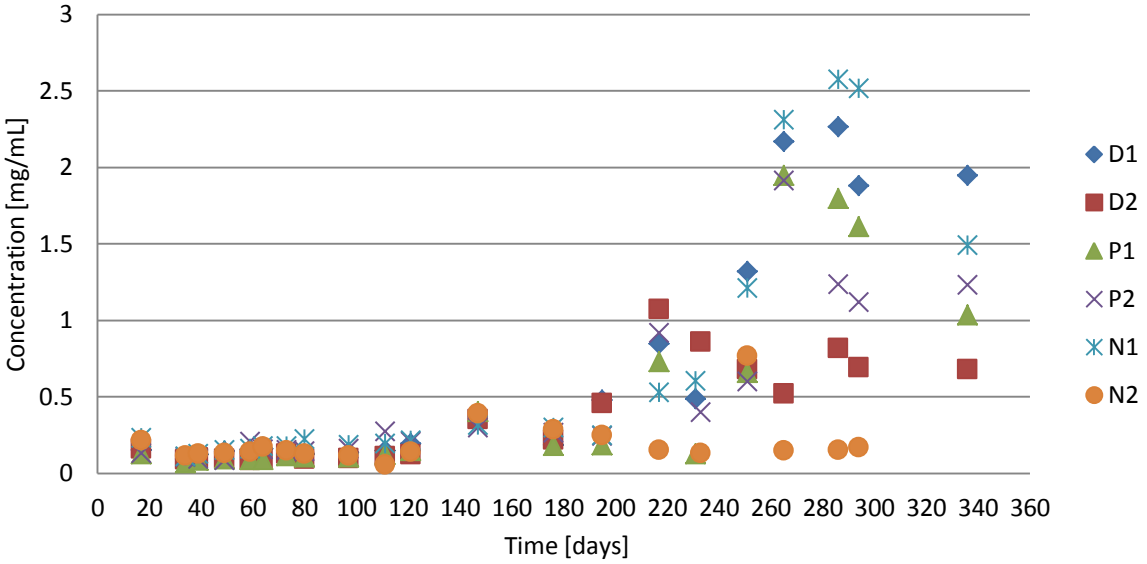


**Figure B1:** BEGO concentrations over time using dCOD measurements for SSR1

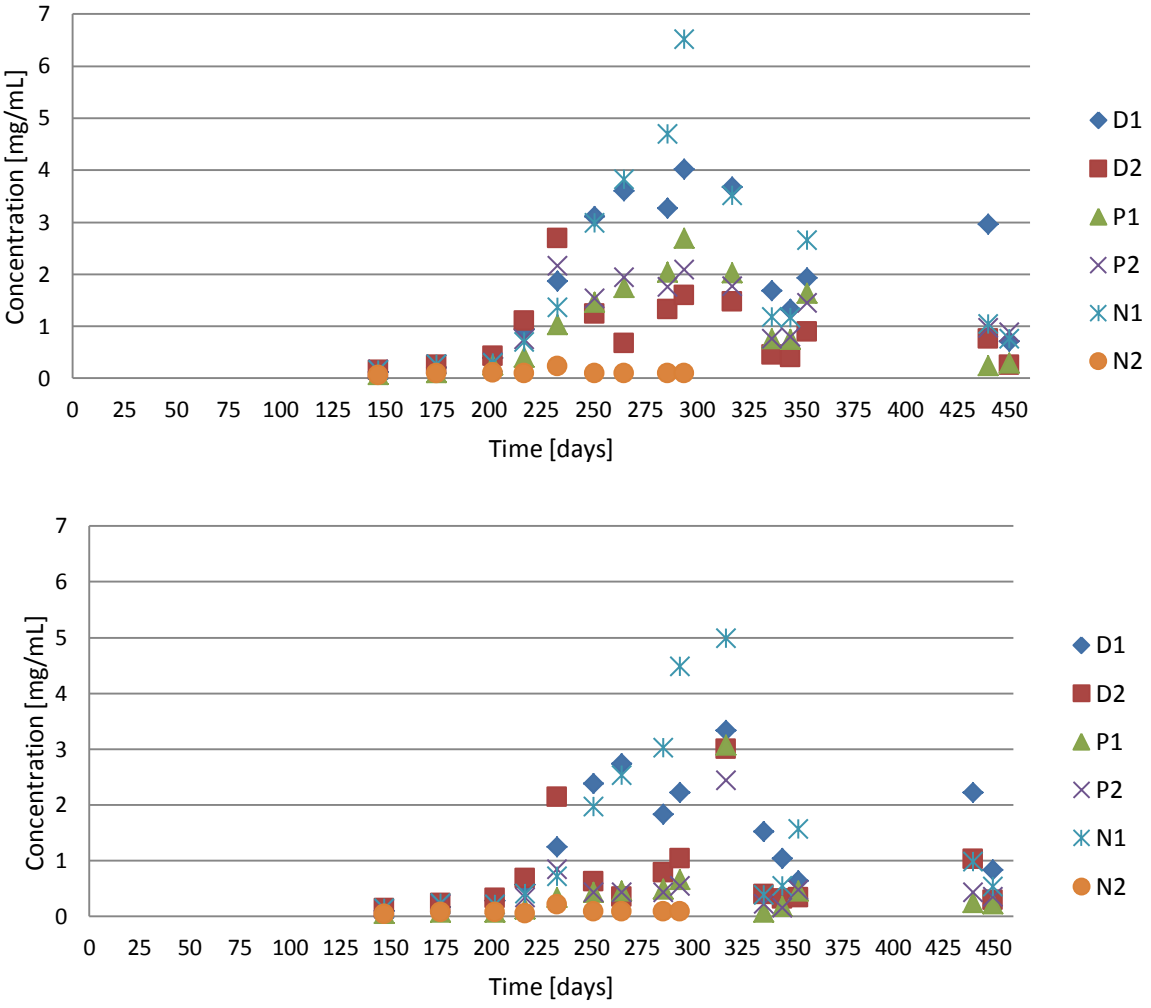


**Figure B2:** BEGO concentrations using UV-Vis method at 229 nm (top) and 300 nm (bottom) for SSR1. After reactors were terminated on day 360, the two step-filtration protocol was conducted in the entire volume. On day 440 measurements of the permeate of the coarse filtration were performed and on day 450 measurements of the BEGO collection filter permeate were done

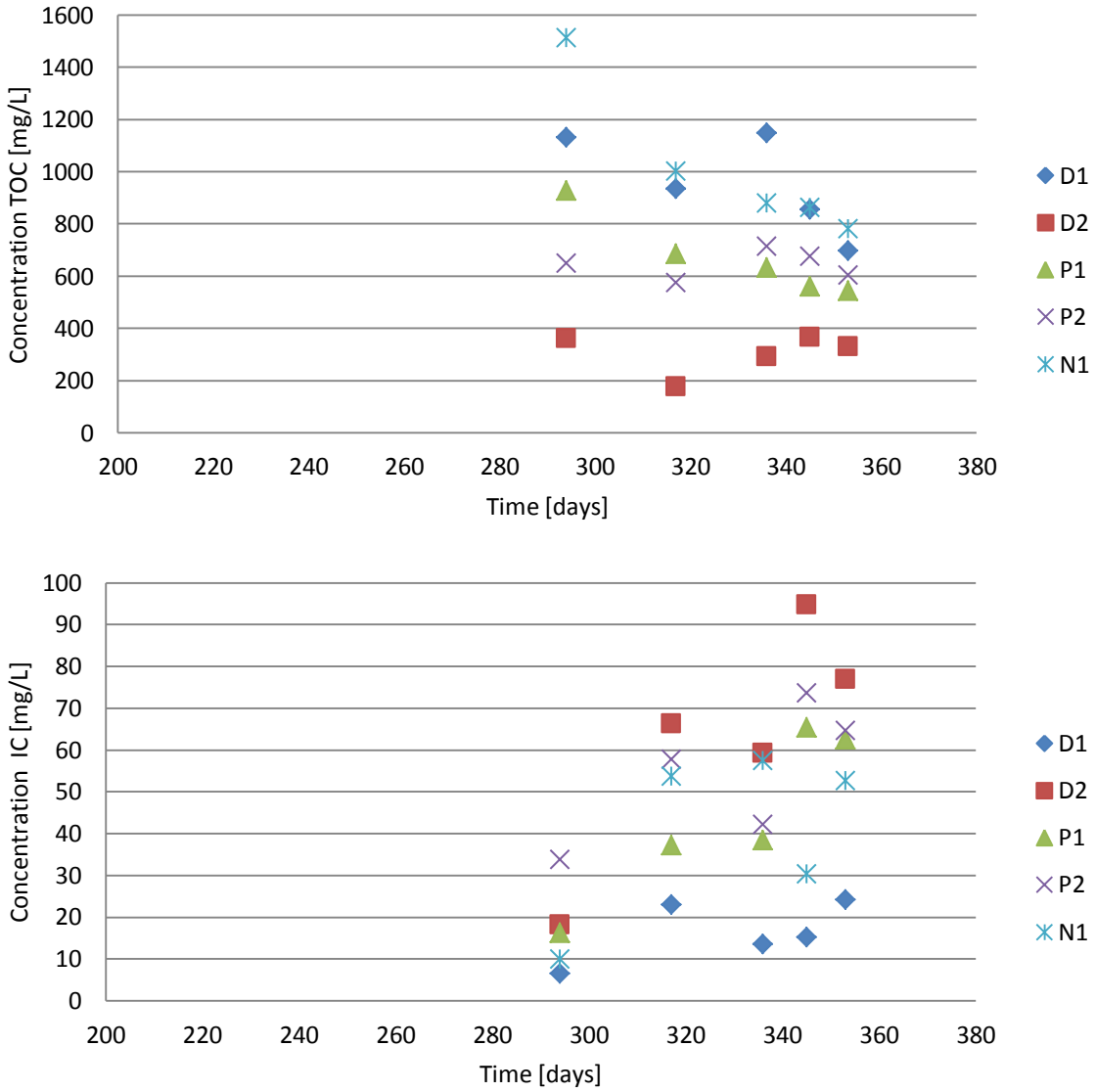


**Figure B3:** Total organic carbon (top) and inorganic carbon (bottom) measurements for SSR1

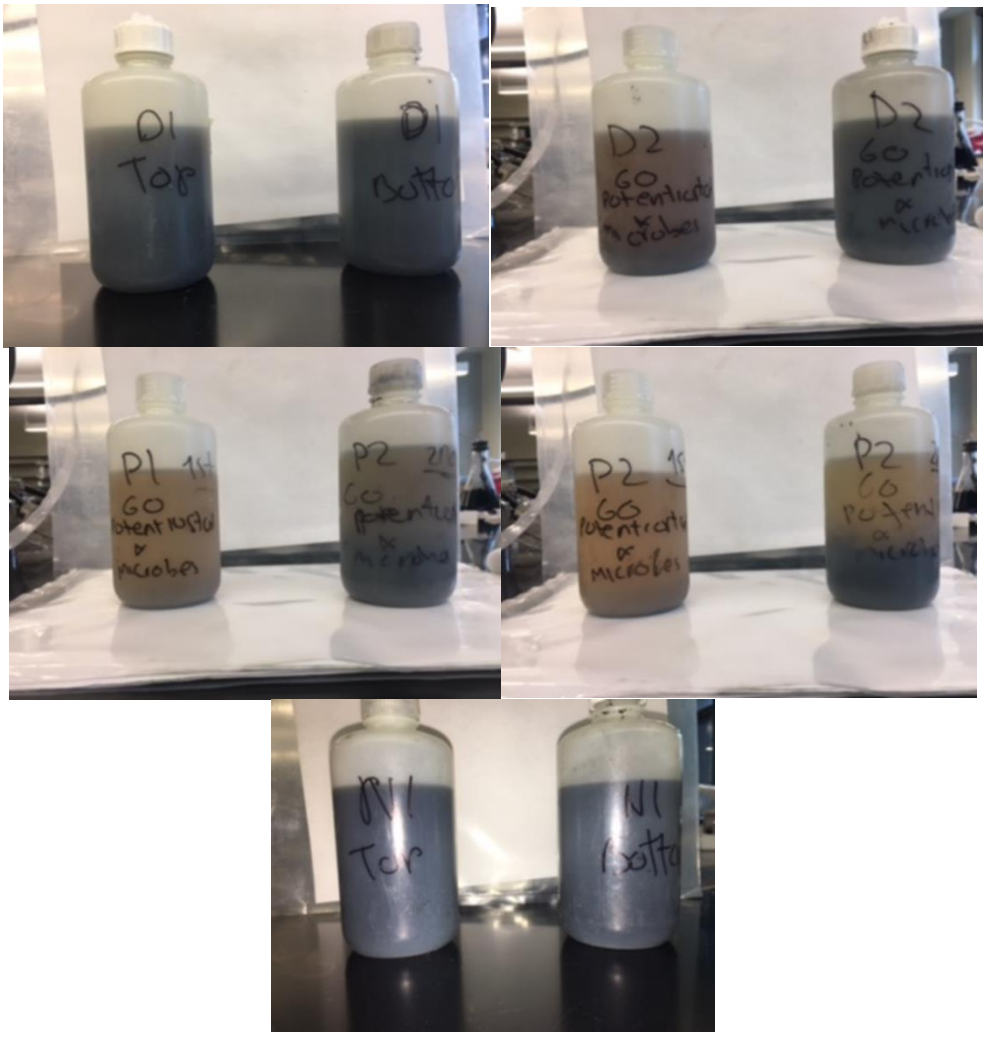


**Figure B4:** Reactor contents divided by upper half of the reactor volume (suspended liquid) and lower half of reactor volume (sludge and aggregates) for the SSR1 trial excluding N2

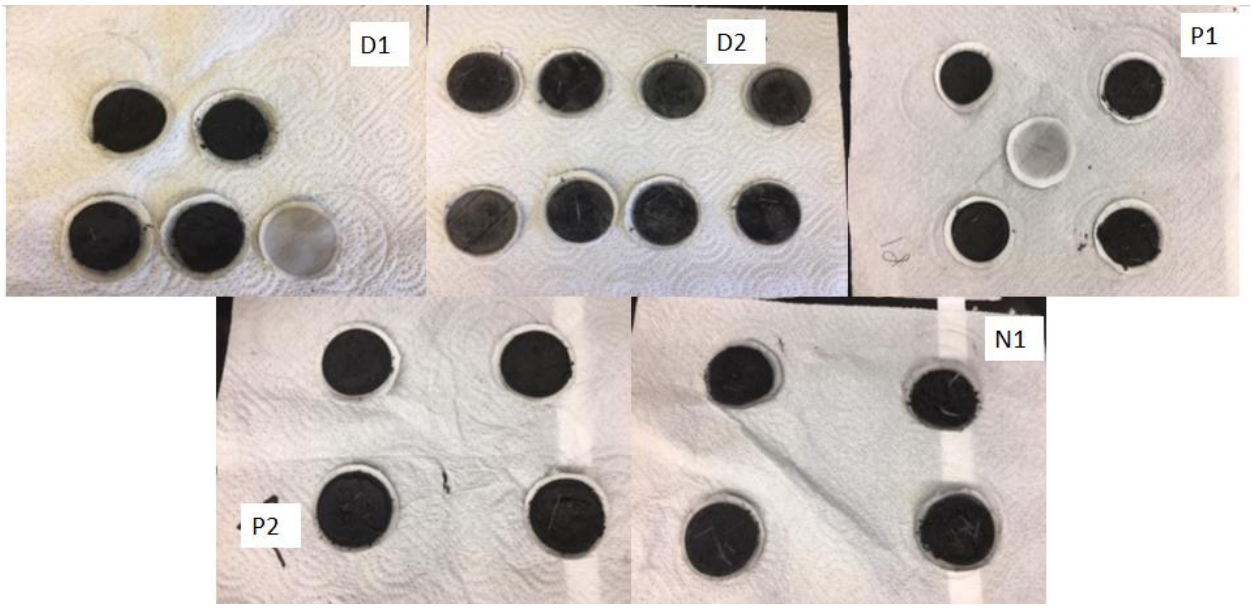


| Reactor ID | Total solids on coarse membrane [g] |
|---|---|
| D1 | 4.93 |
| D2 | 0.95 |
| P1 | 13.57 |
| P2 | 16.28 |
| N1 | 8.85 |

**Figure B5:** Solids on the coarse filter for all of the SSR1. These were done in separate trials to avoid clogging of the membrane

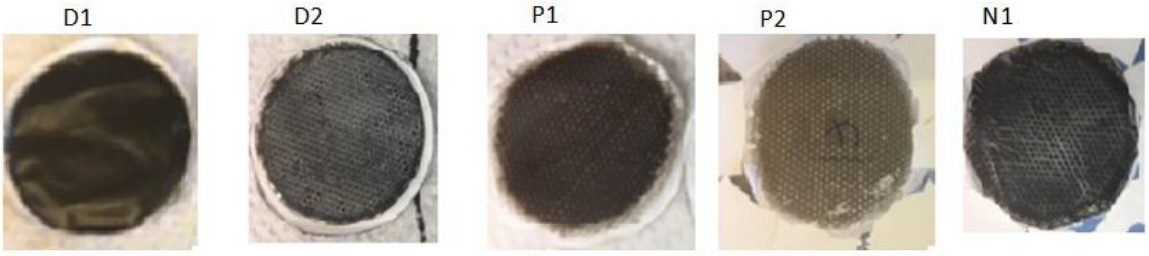


**Figure B6:** One Teflon membrane from each reactor with BEGO collected. This step was done multiple times to avoid clogging of the membrane

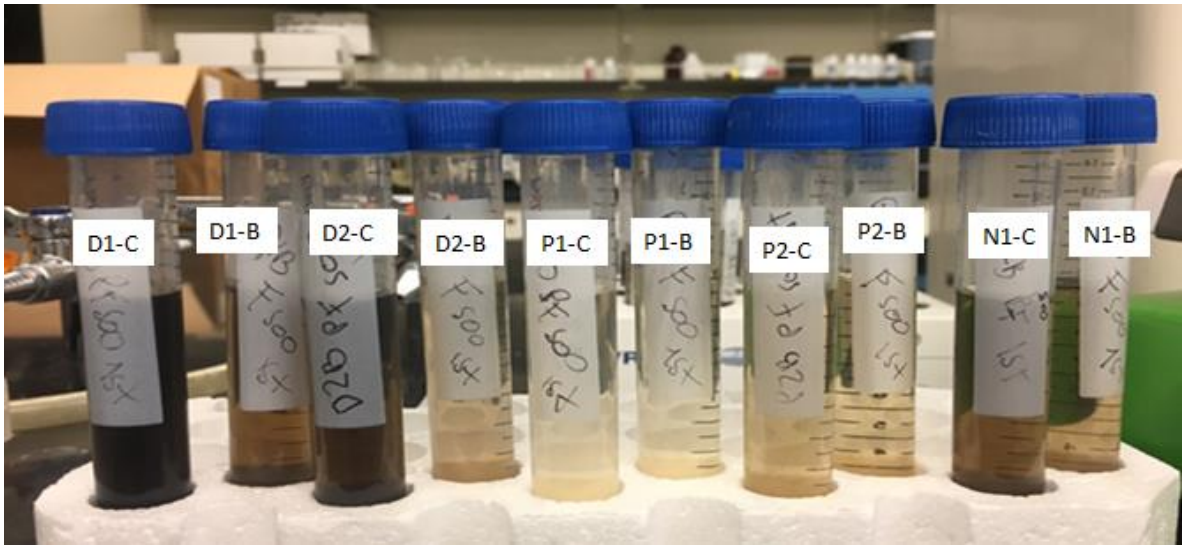


**Figure B7:** Permeate of the coarse filtration (C) next to the permeate of the BEGO collection filtration (B) for each reactor. Some of these were diluted to allow faster flow through the filters and avoid clogging

**Experiment SSR2: Small-scale reactors - trial 2**

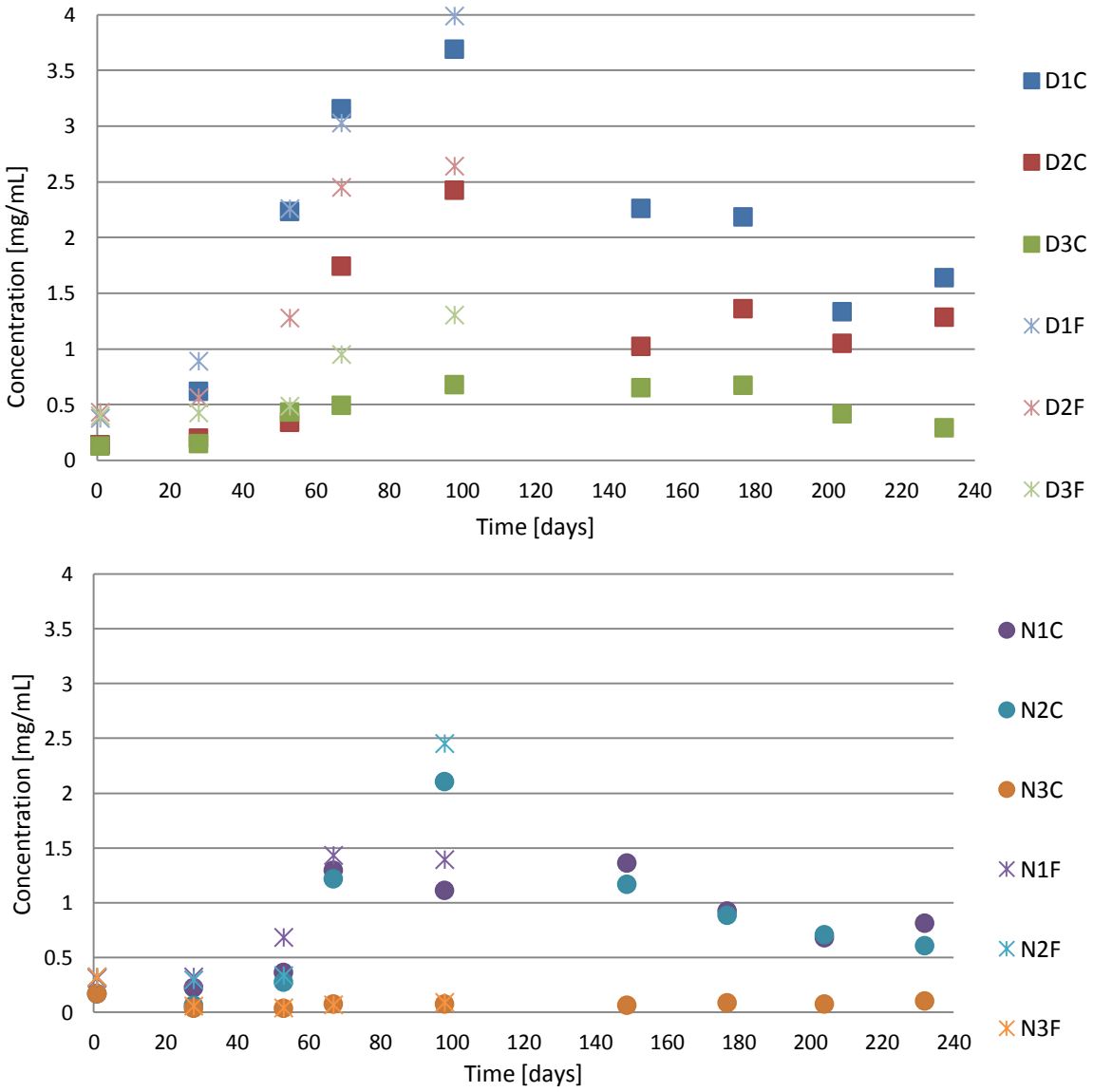


**Figure B8:** BEGO concentrations using UV-Vis method at 229 nm for the Drake (top) and New Belgium (bottom) inoculated reactors. Samples were purified using the centrifugation (C) and filtration (F) protocols for the SSR2

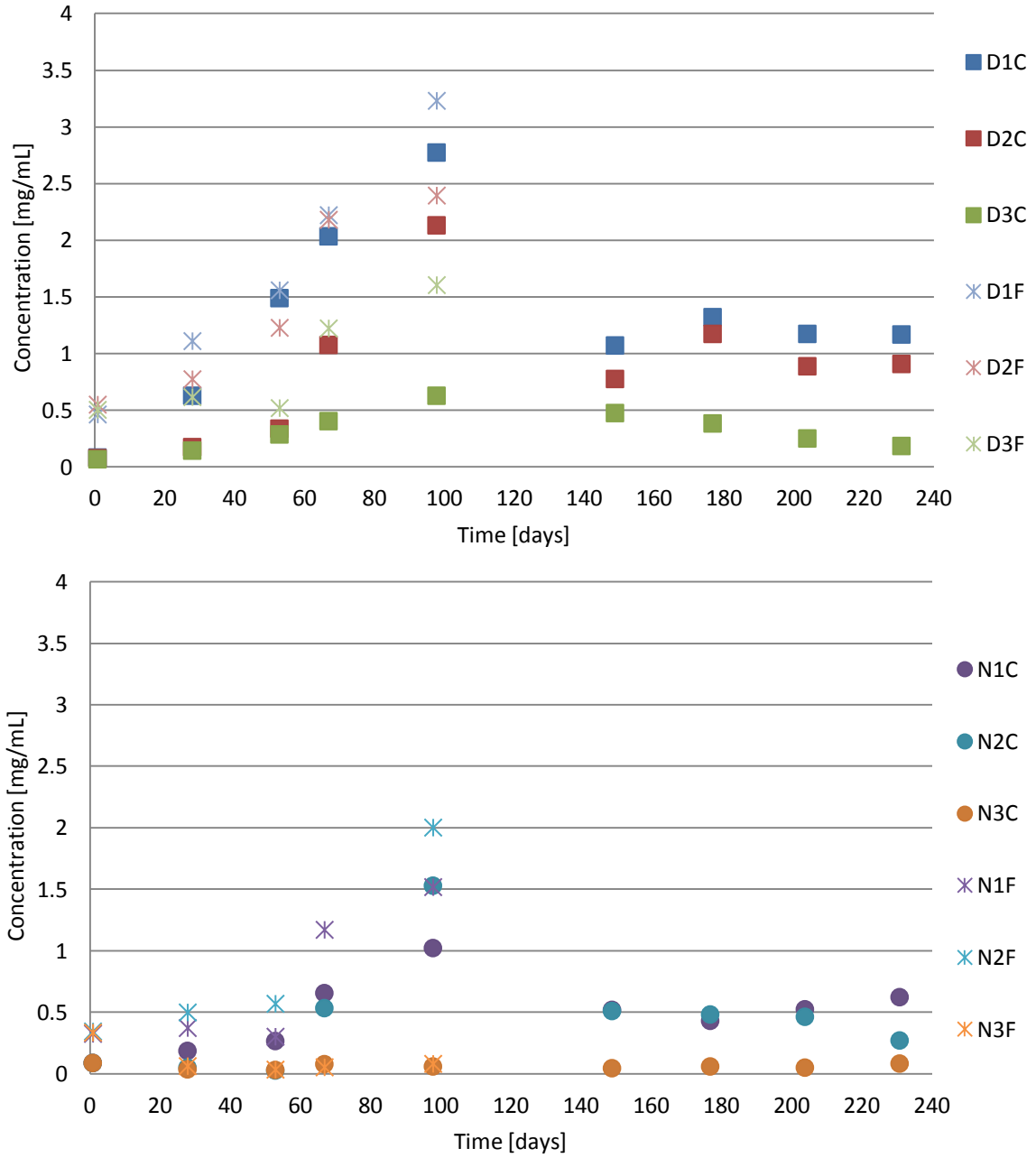


**Figure B9:** BEGO concentrations using UV-Vis method at 300 nm for the Drake (top) and New Belgium (bottom) inoculated reactors. Samples were purified using the centrifugation (C) and filtration (F) protocols for the SSR2

**Experiment LSR1: Large-scale reactors - trial 1**

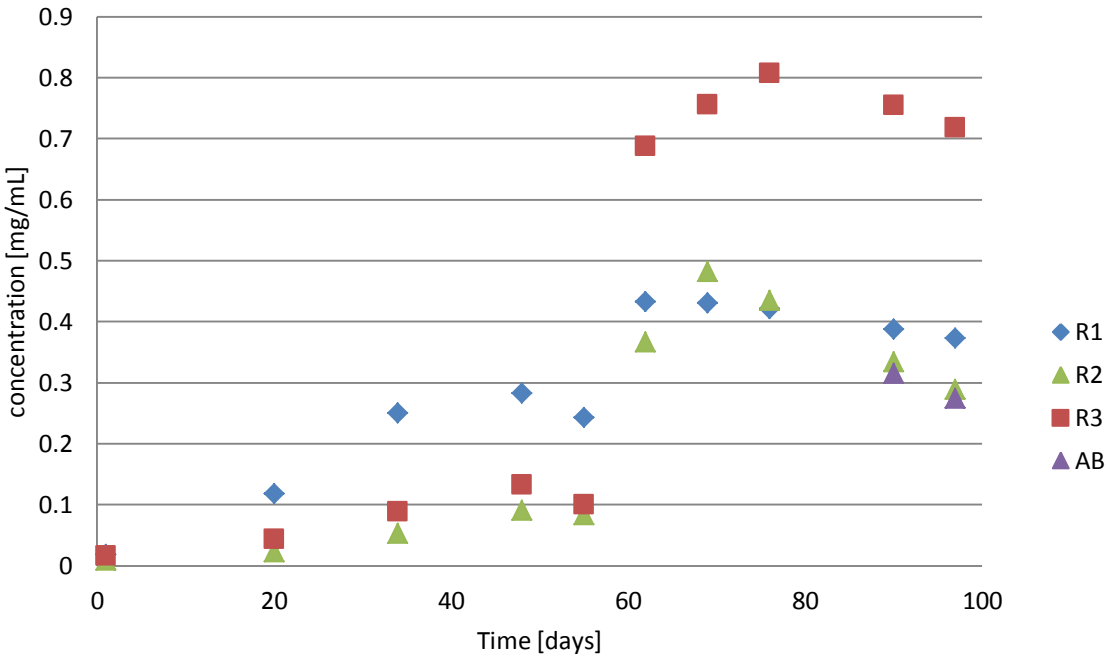


**Figure B10:** BEGO concentrations over time using dCOD data for LSR1

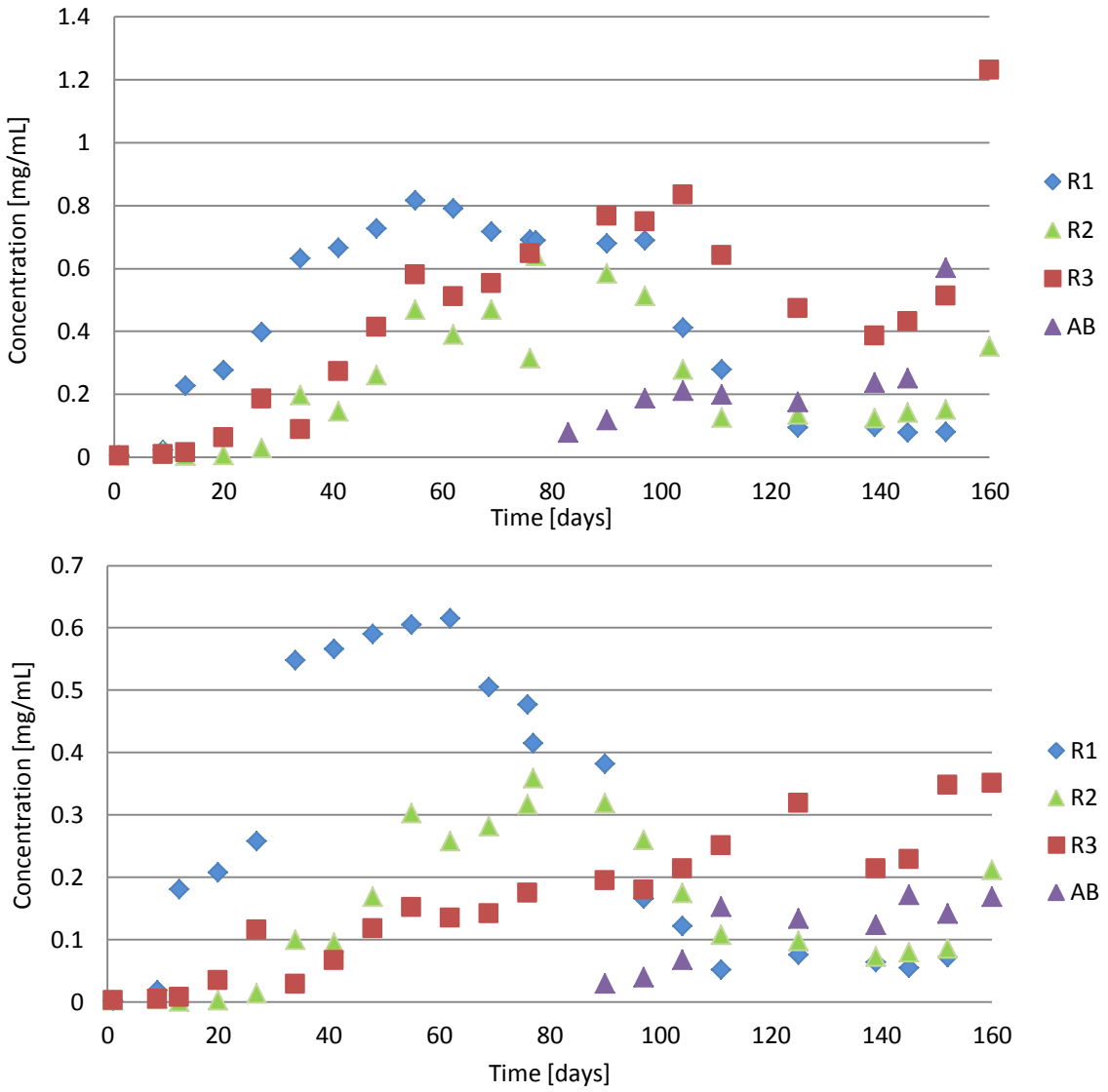


**Figure B11:** BEGO concentrations over time using UV-Vis data at wavelength 229 (top) and 300 (bottom) for LSR1

**Experiment LSR2: Large-scale reactors - trial 2**

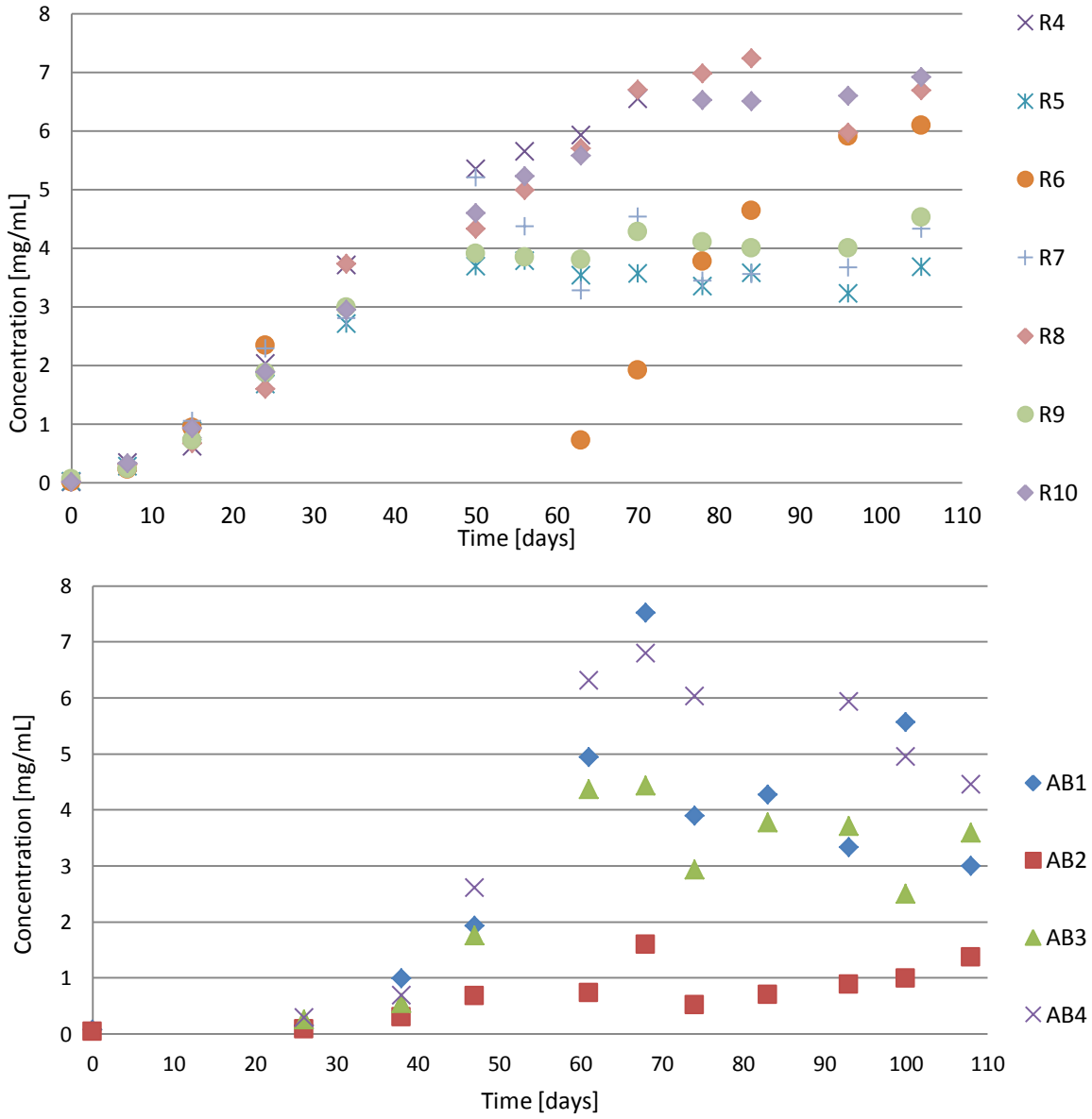


**Figure B12:** BEGO concentration over time calculated using the UV-Vis method at wavelength 229 nm for the LSR2A (top) and LSR2B (bottom). Reactor R6 was terminated on day 24 for BEGO harvesting and restarted on day 57 with new media. Reactor R4 was terminated on day 67 due to current decreasing to zero and rod samples were needed for surface chemistry analysis. All of the other reactors reached zero current at different rates (Figure A7) and were terminated on day 105 for the LSR2B and day 108 for the LSR2A

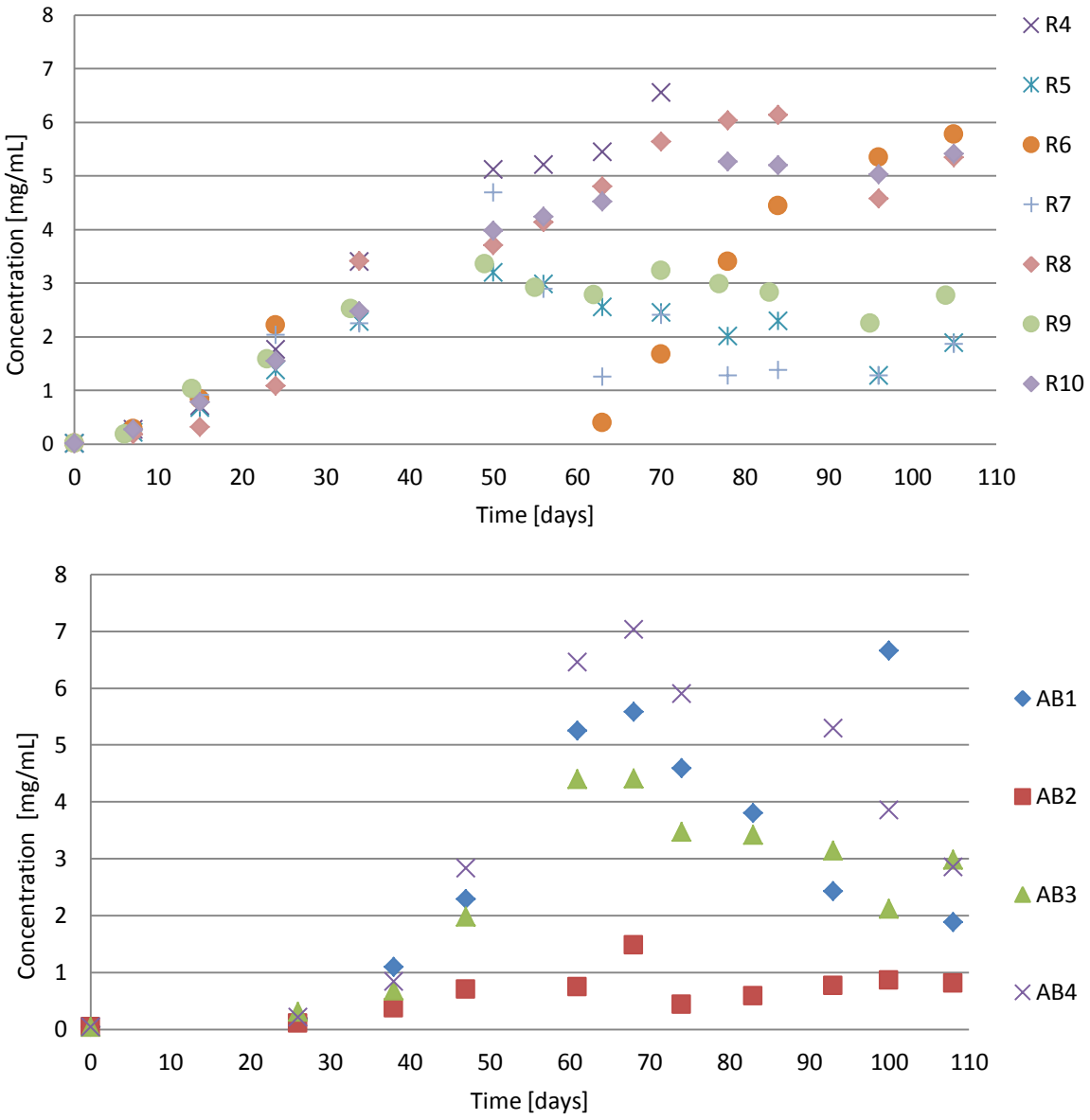


**Figure B13:** BEGO concentration over time calculated using the UV-Vis method at wavelength 300nm for the LSRB (top) and LSRA (bottom). Reactor R6 was terminated on day 24 for BEGO harvesting and restarted on day 57 with new media. Reactor R4 was terminated on day 67 due to current decreasing to zero and rod samples were needed for surface chemistry analysis. All of the other reactors reached zero current at different rates (Figure A7) and were terminated on day 105 for the LSR2B and day 108 for the LSR2A

# APPENDIX C: PROGRESS PHOTOS

**Figure C1**: D reactors for SSR1 trial on day 20 (left) and day 317 (right). 1) D1 connected. 2) D2 connected. 3) CD1 disconnected 4) CD2 disconnected

**Figure C2:** P reactors for SSR1 trial on day 20 (left) and day 317 (right). 1) P1 connected. 2) P2 connected. 3) CP1 disconnected 4) CP2 disconnected

**Figure C3:** N reactors for SSR1 trial on day 20 (left) and day 317 (right). 1) N1 connected. 2) N2 connected. 3) CN1 disconnected 4) CN2 disconnected. Photo for N2 after operation was taken on day 294 due to the reactor being terminated early

**Figure C4:** Rods AB1, AB2, AB3, and AB4 after lifetime for LSR2

**Figure C1:** D reactors for SSR1 trial on day 20 (left) and day 317 (right). 1) D1 connected. 2) D2 connected. 3) CD1 disconnected 4) CD2 disconnected

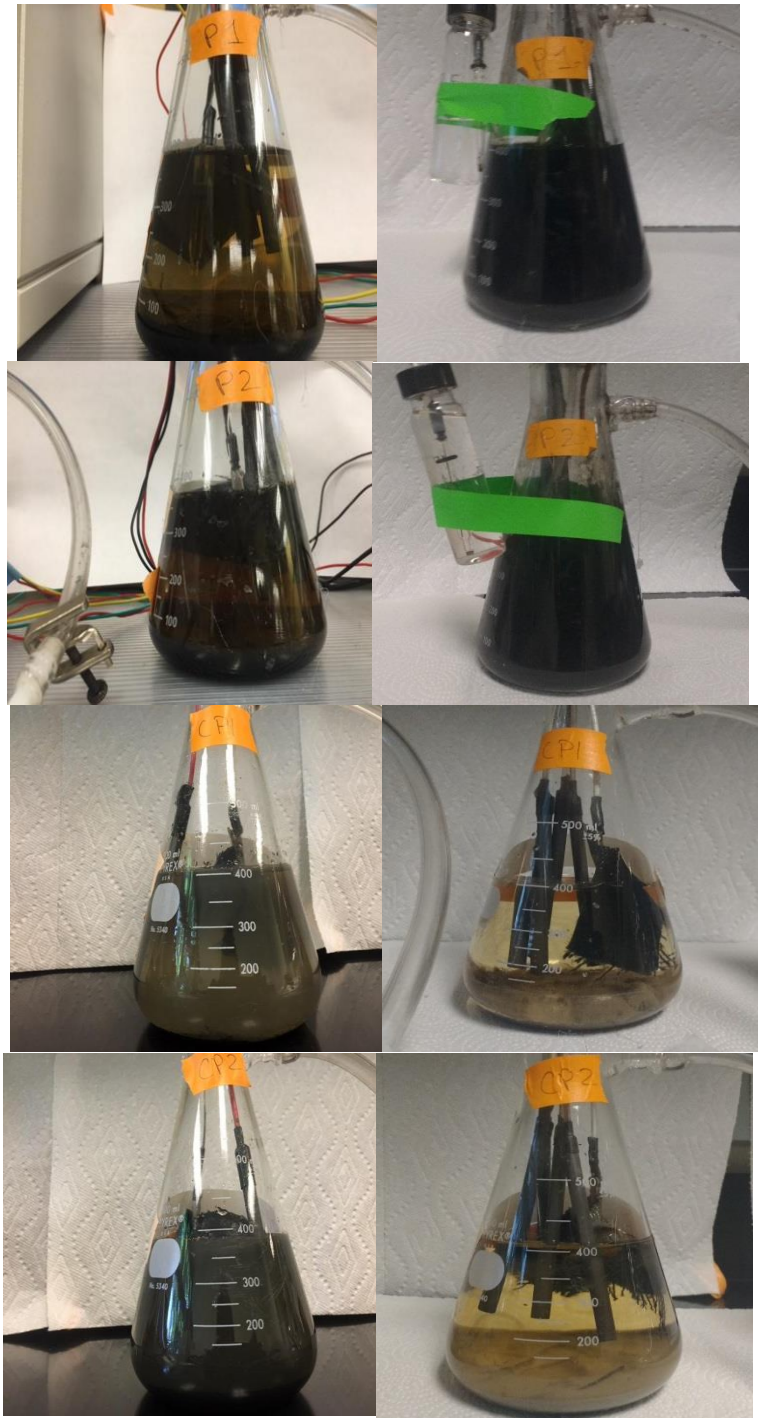


**Figure C2:** P reactors for SSR1 trial on day 20 (left) and day 317 (right). 1) P1 connected. 2) P2 connected. 3) CP1 disconnected 4) CP2 disconnected

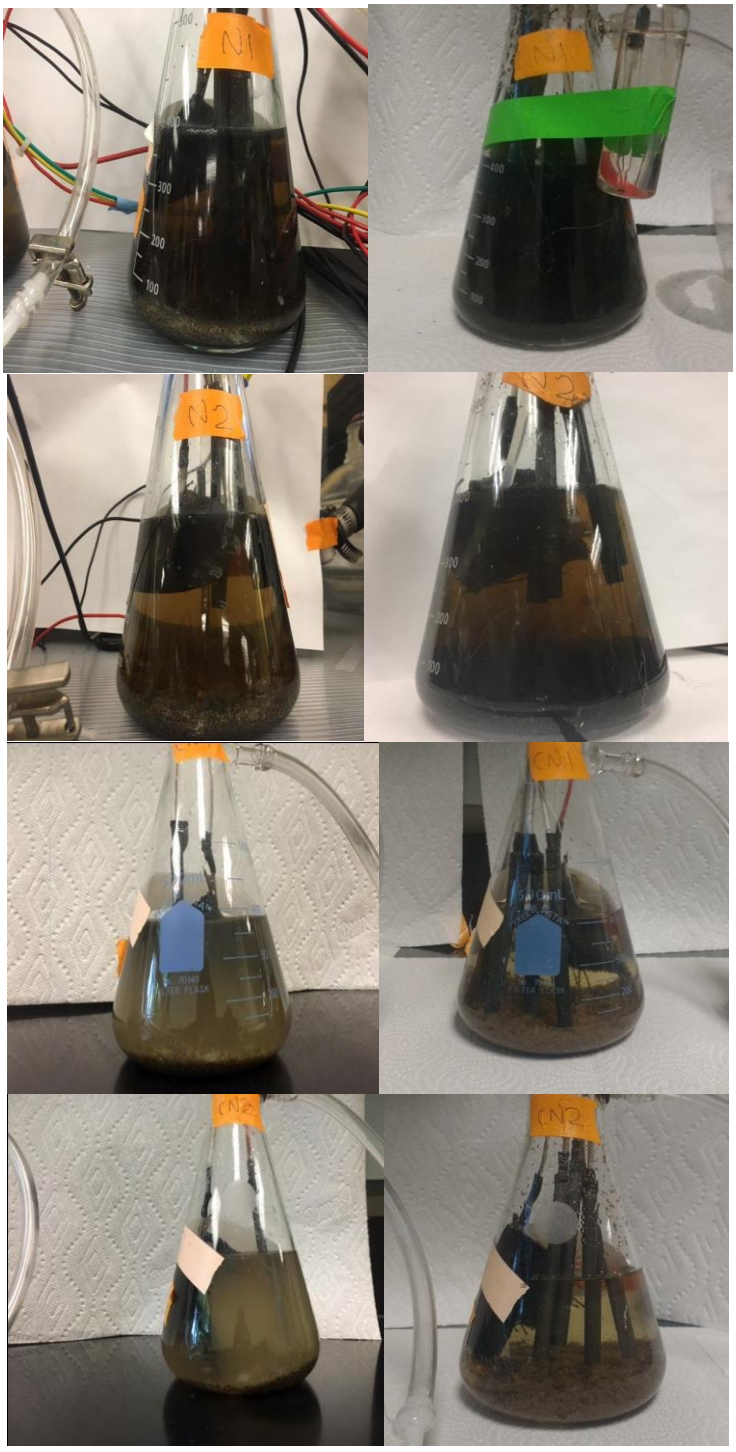


**Figure C3:** N reactors for SSR1 trial on day 20 (left) and day 317 (right). 1) N1 connected. 2) N2 connected. 3) CN1 disconnected 4) CN2 disconnected. Photo for N2 after operation was taken on day 294 due to the reactor being terminated early


**Figure C4:** Rods AB1, AB2, AB3, and AB4 after lifetime for LSR2

# APPENDIX D: PRODUCTION RATES

**Experiment SSR1: Small-scale reactors - trial 1**

**Figure D1:** Rate constant for BEGO production phase using the dCOD method from day 176 to day 286

**Experiment SSR2: Small-scale reactors - trial 2**

**Figure D2:** BEGO concentrations using UV-Vis method at 229 nm (top) and 300 nm (bottom) for the Drake (D) and New Belgium (N) inoculated reactors. Samples were purified using the centrifugation (C) and filtration (F) protocols for the SSR2

**Experiment LSR2: Large-scale reactors - trial 2**

**Figure D3:** BEGO concentrations using UV-Vis method for the biotic reactors (left) and the abiotic reactors (right) using the 300 nm UV-Vis method for the LSR2

## Experiment SSR1: Small-scale reactors - trial 1

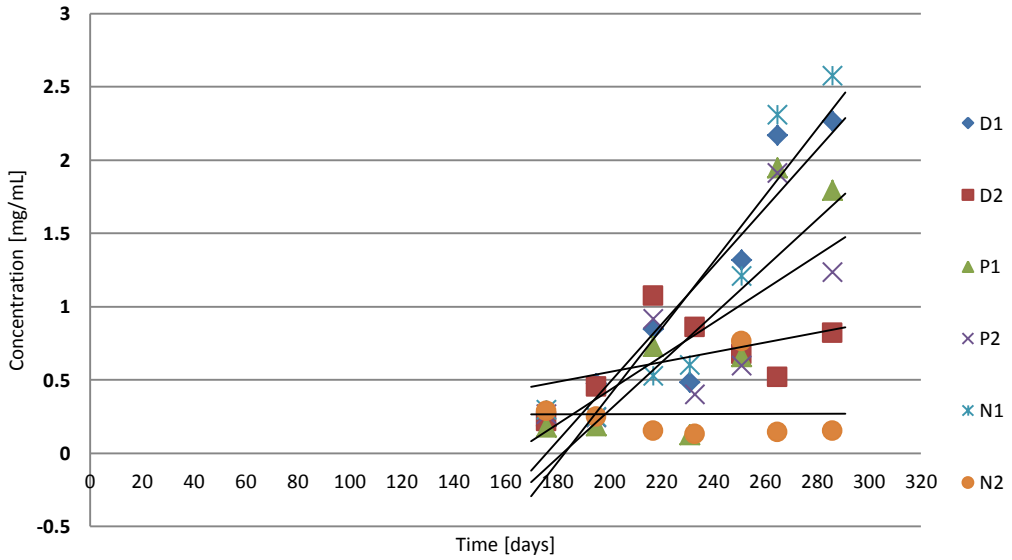


| Reactor | Production rate [mg/Lday] | R2 value |
|---|---|---|
| D1 | 19.9 | 0.855 |
| D2 | 3.4 | 0.208 |
| P1 | 16.3 | 0.680 |
| P2 | 11.5 | 0.539 |
| N1 | 22.8 | 0.844 |
| N2 | ~0 | ~0 |

**Figure D1:** Rate constant for BEGO production phase using the dCOD method from day 176 to day 286

## Experiment SSR2: Small-scale reactors - trial 2

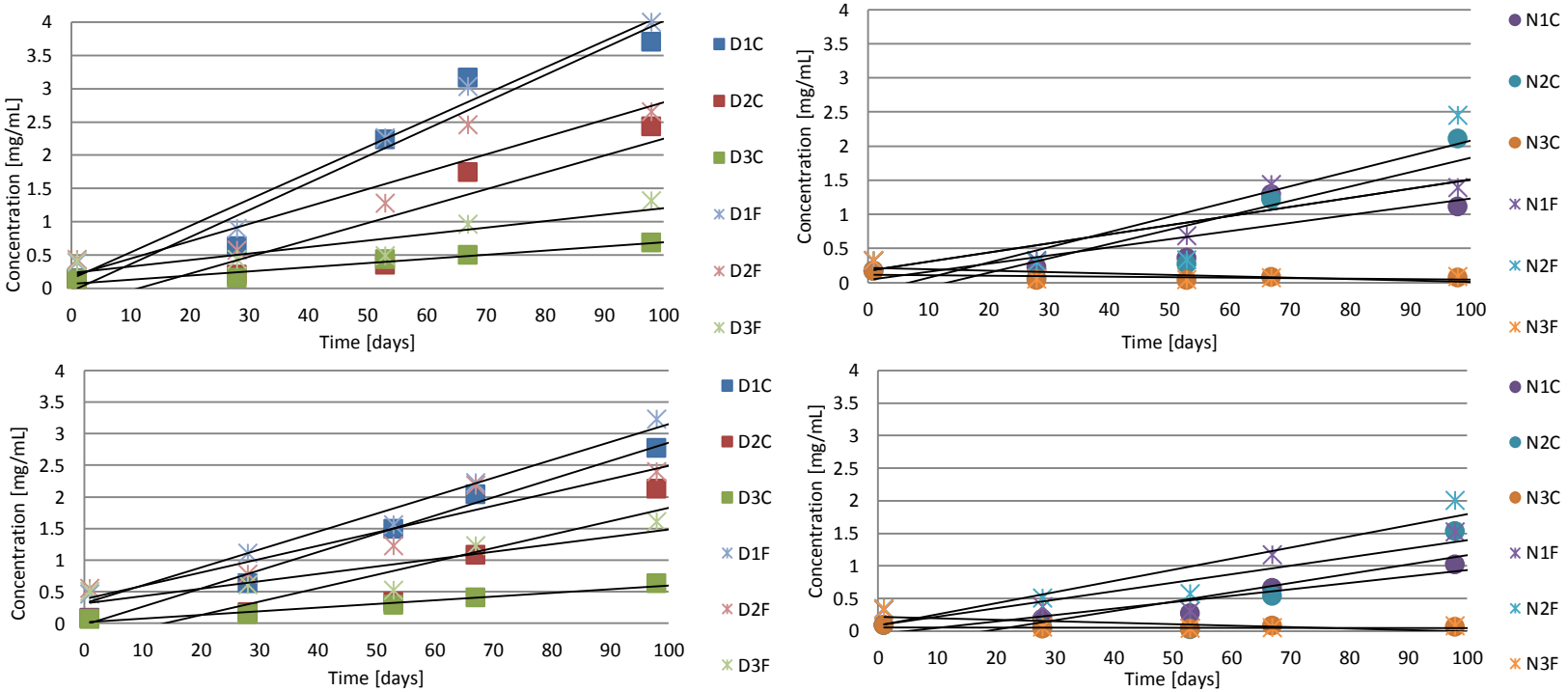


| Reactor | Production rate [mg/Lday] | | | | $R^2$ value | | | |
|---|---|---|---|---|---|---|---|---|
| | C 229 | F 229 | C 300 | F 300 | C 229 | F 229 | C 300 | F 300 |
| D1 | 40.7 | 39.7 | 28.9 | 28.4 | 0.943 | 0.975 | 0.990 | 0.878 |
| D2 | 25.3 | 26.1 | 21.2 | 21.1 | 0.800 | 0.875 | 0.831 | 0.683 |
| D3 | 6.2 | 9.7 | 5.9 | 11.6 | 0.940 | 0.814 | 0.967 | 0.027 |
| N1 | 11.9 | 13.4 | 9.8 | 13.1 | 0.690 | 0.800 | 0.978 | 0.727 |
| N2 | 21 | 22.3 | 14.3 | 17.1 | 0.783 | 0.739 | 0.895 | 0.833 |
| N3 | 0 | 0 | 0 | 0 | 0.248 | 0.409 | 0.755 | 0.461 |

**Figure D2:** BEGO concentrations using UV-Vis method at 229 nm (top) and 300 nm (bottom) for the Drake (D) and New Belgium (N) inoculated reactors. Samples were purified using the centrifugation (C) and filtration (F) protocols for the SSR2

## Experiment LSR2: Large-scale reactors - trial 2

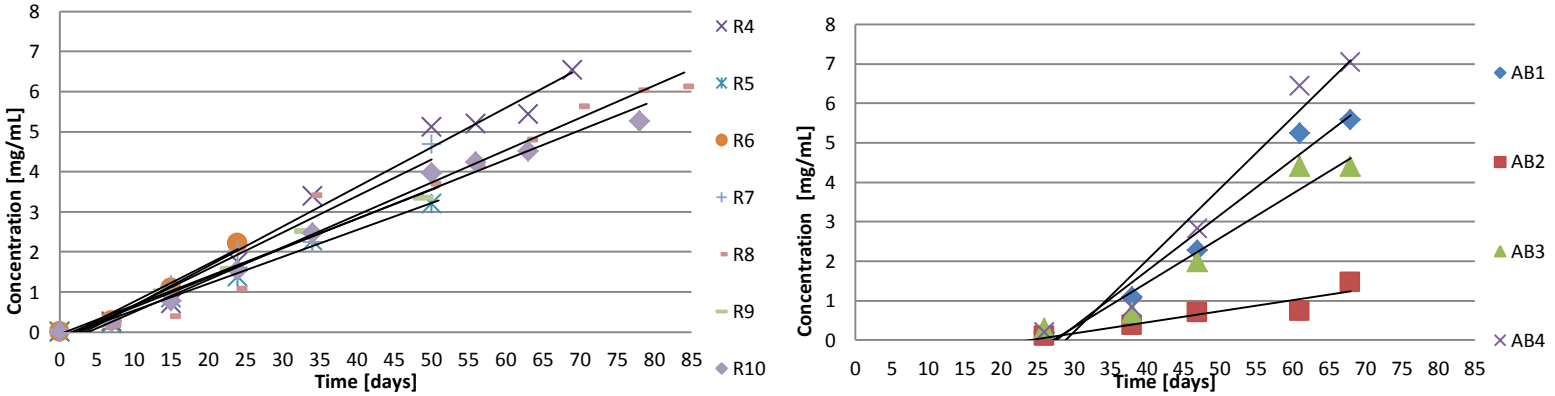


| Production rate [mg/Lday] | | | | | | | |
|---|---|---|---|---|---|---|---|
| **Reactor** | **300** | **$R^2$** | **Lag [days]** | **Reactor** | **300** | **$R^2$** | **Lag [days]** |
| R4 | 98.7 | 0.980 | 0 | AB1 | 140.8 | 0.983 | 26 |
| R5 | 66.9 | 0.992 | 0 | AB2 | 28.1 | 0.837 | 26 |
| R6 | 94.2 | 0.932 | 0 | AB3 | 112.6 | 0.940 | 26 |
| R7 | 91.1 | 0.938 | 0 | AB4 | 180.9 | 0.935 | 26 |
| R8 | 80.8 | 0.969 | 0 | | | | |
| R9 | 72.1 | 0.988 | 0 | | | | |
| R10 | 73.6 | 0.984 | 0 | | | | |

**Figure D3:** BEGO concentrations using UV-Vis method for the biotic reactors (left) and the abiotic reactors (right) using the 300 nm UV-Vis method for the LSR2

# APPENDIX E: CHARACTERIZATION

## UV-Vis

**Figure E1:** GO Sigma Aldrich standard UV-Vis scan at different concentrations in mg/mL

**Figure E2:** UV-Vis of BEGO from scrapped membranes of the R2 reactor from the LSR1 trial at different dilutions in DI water using mixing

**Figure E3**: UV-Vis scans of the SSR1 reactors on day 217 with dilutions in DI water

**Figure E4:** UV-Vis scans of the SSR2 reactors on day 98 purified using centrifugation (top) and filtration (bottom) protocols at dilutions in DI water

**Figure E5:** UV-Vis scans of the LSRB2 reactors on day 70 (top) and day 105 (bottom) at dilutions in DI water

**Figure E6:** UV-Vis scans of the LSRA2 reactors on day 92 with dilutions in DI water

## FT-IR

**Figure E7:** FT-IR spectrum of the SSR1 trial compared with a GO standard. Concentration in each sample varies affecting absorbance. Data collected early on the experiment on day 115

**Figure E8:** FT-IR spectrum of the SSR1 trial at the end of the trial. Samples collected using the two-filtration system with solids in the BEGO membrane. Concentrations of the solids were low thus the low in absorbance

## TEM

**Figure E9:** TEM images and FFT for the D1 (top) and D2 samples

**Figure E10:** TEM images and FFT for the P1 (top) and P2 samples

**AFM**



**XPS**



**ICP-MS**

**Figure E22:** ICP-MS concentration of metals in the media in the SSR2 reactors at a trace concentration threshold

**Conductivity in solution**

**Table E23:** Conductivity of DI water, media and purchased GO standards

**Table E24:** Conductivity of the SSR1 bulk solutions on day 245

**Table E25:** Conductivity of the LSR1 bulk solutions on day 54

**UV-Vis**

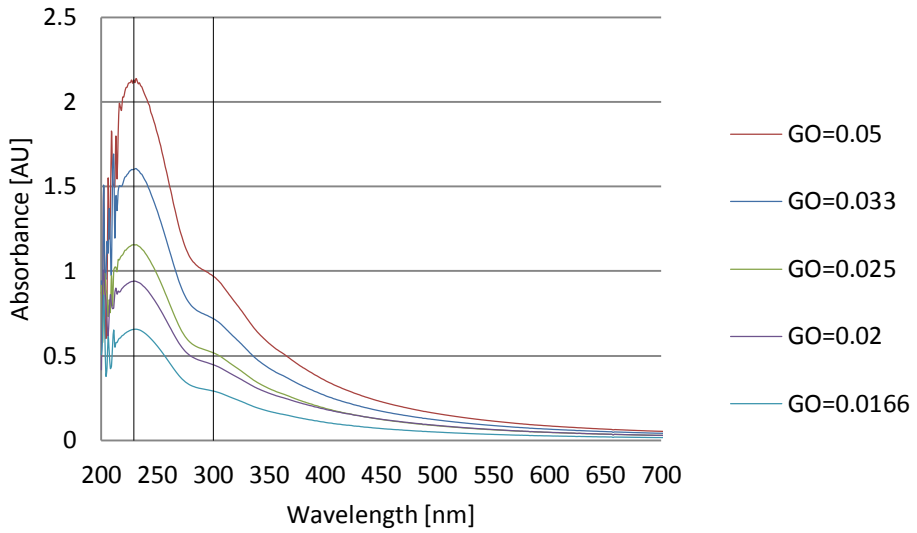


**Figure E1:** GO Sigma Aldrich standard UV-Vis scan at different concentrations in mg/mL

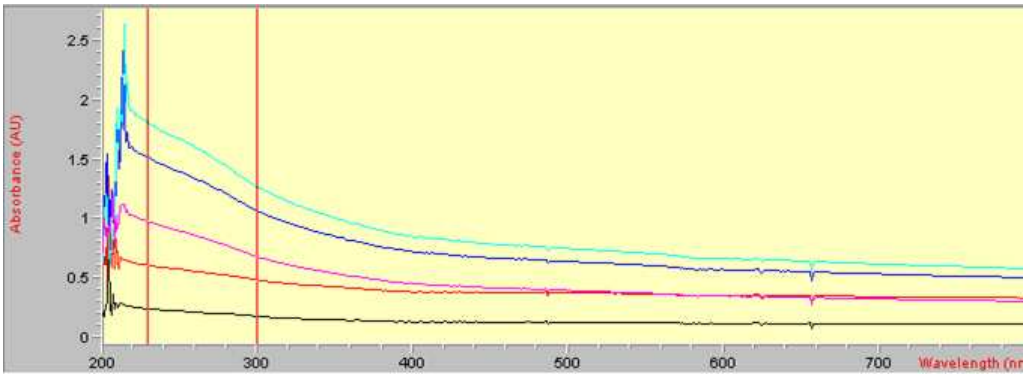


**Figure E2:** UV-Vis of BEGO from scrapped membranes of the R2 reactor from the LSR1 trial at different dilutions in DI water using mixing

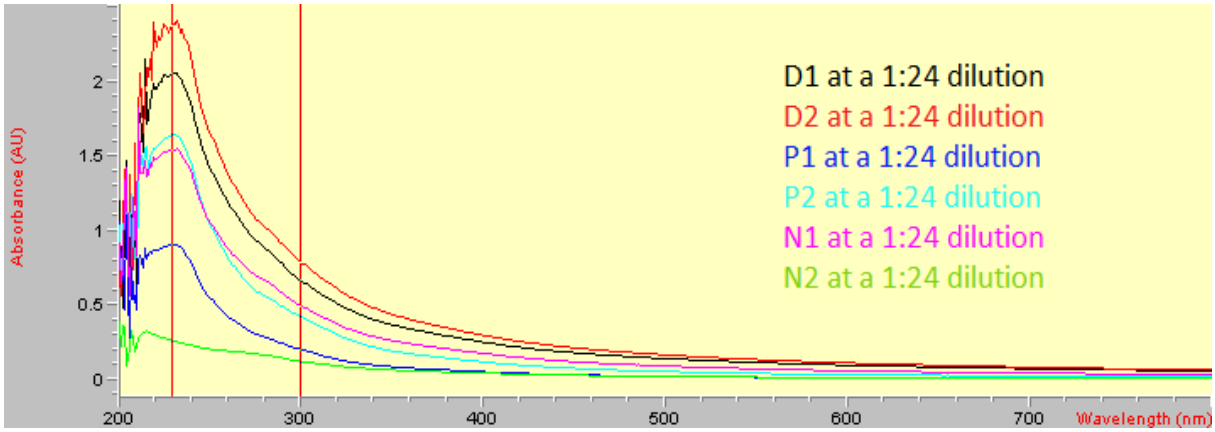


**Figure E3:** UV-Vis scans of the SSR1 reactors on day 217 with dilutions in DI water

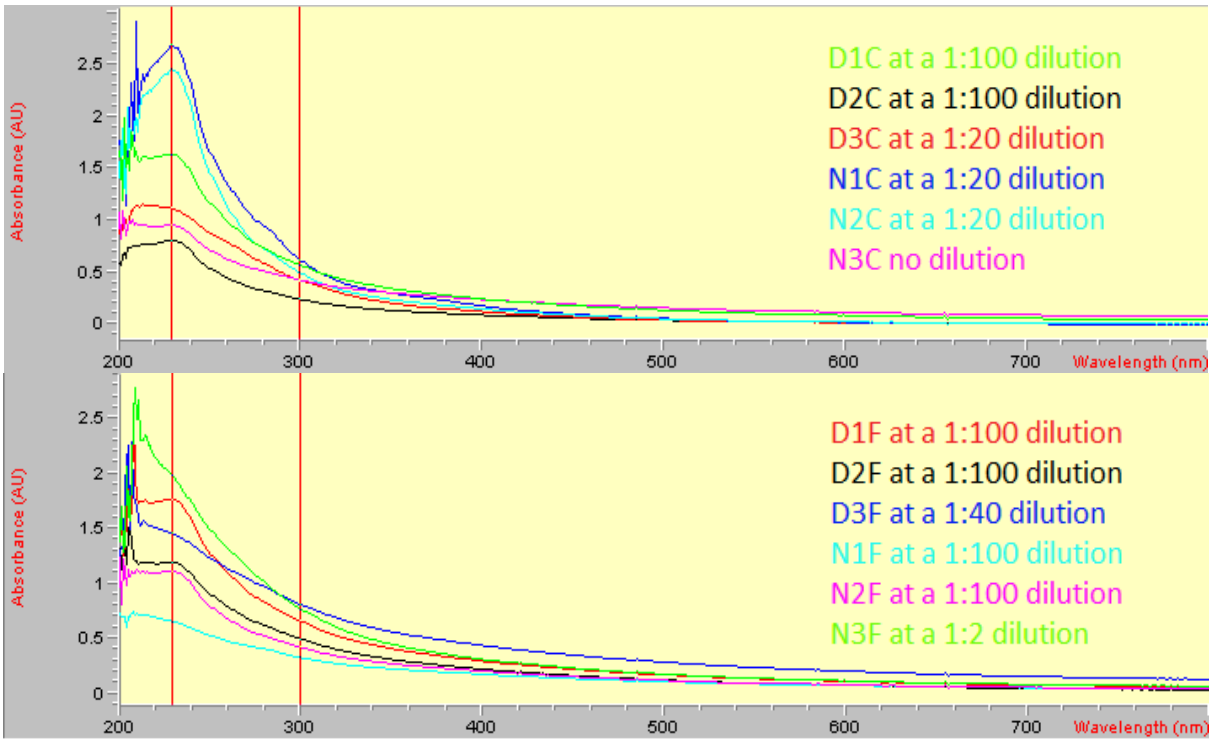


**Figure E4:** UV-Vis scans of the SSR2 reactors on day 98 purified using centrifugation (top) and filtration (bottom) protocols at dilutions in DI water

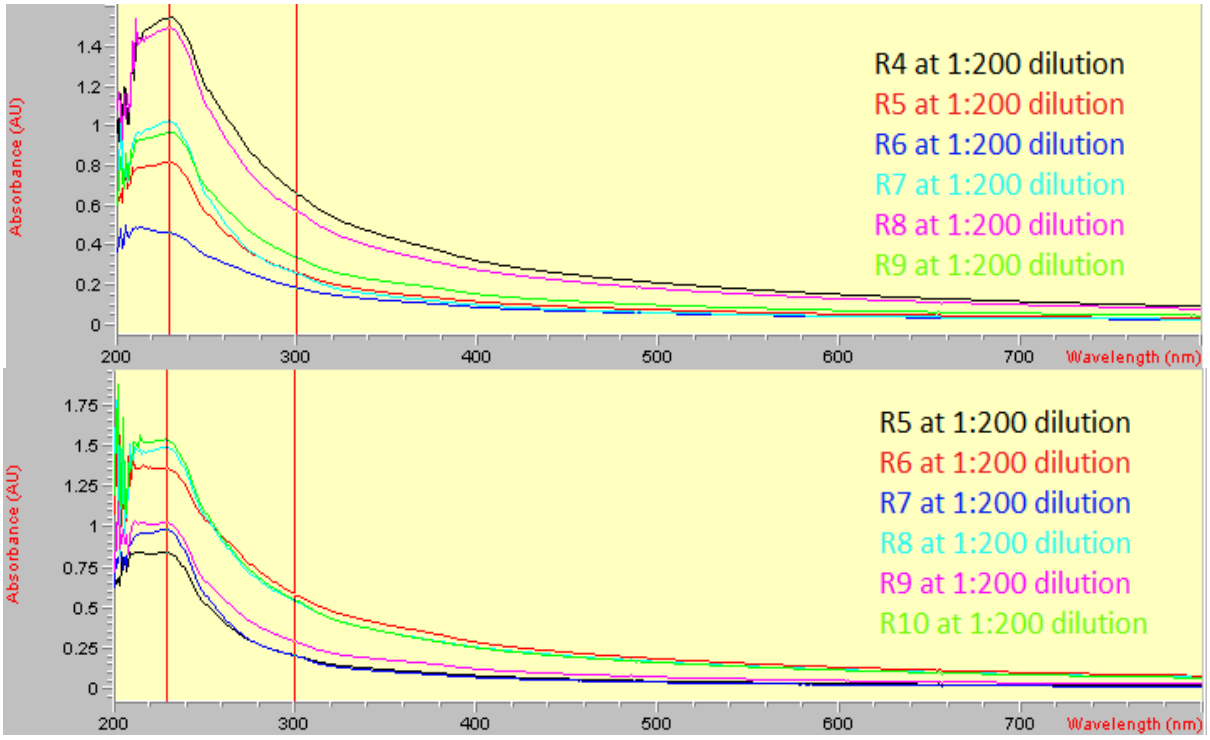


**Figure E**5: UV-Vis scans of the LSRB2 reactors on day 70 (top) and day 105 (bottom) at dilutions in DI water

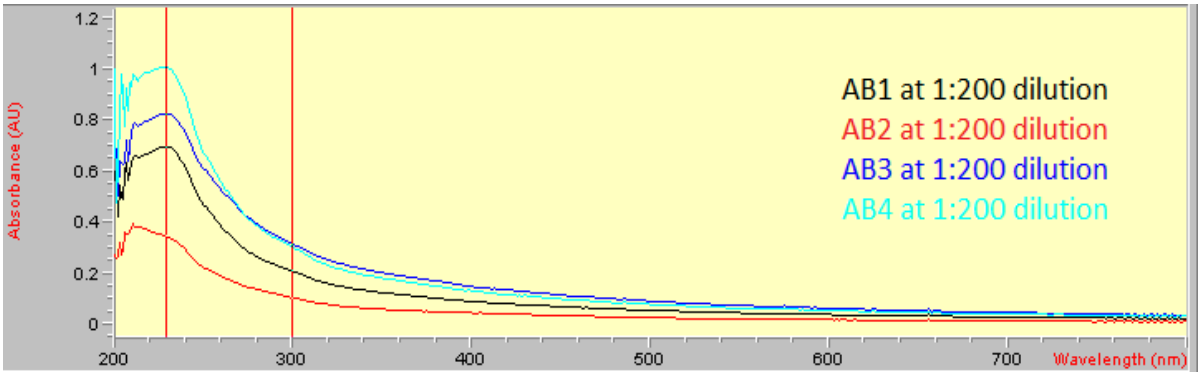


**Figure E6:** UV-Vis scans of the LSRA2 reactors on day 92 with dilutions in DI water

**FT-IR**

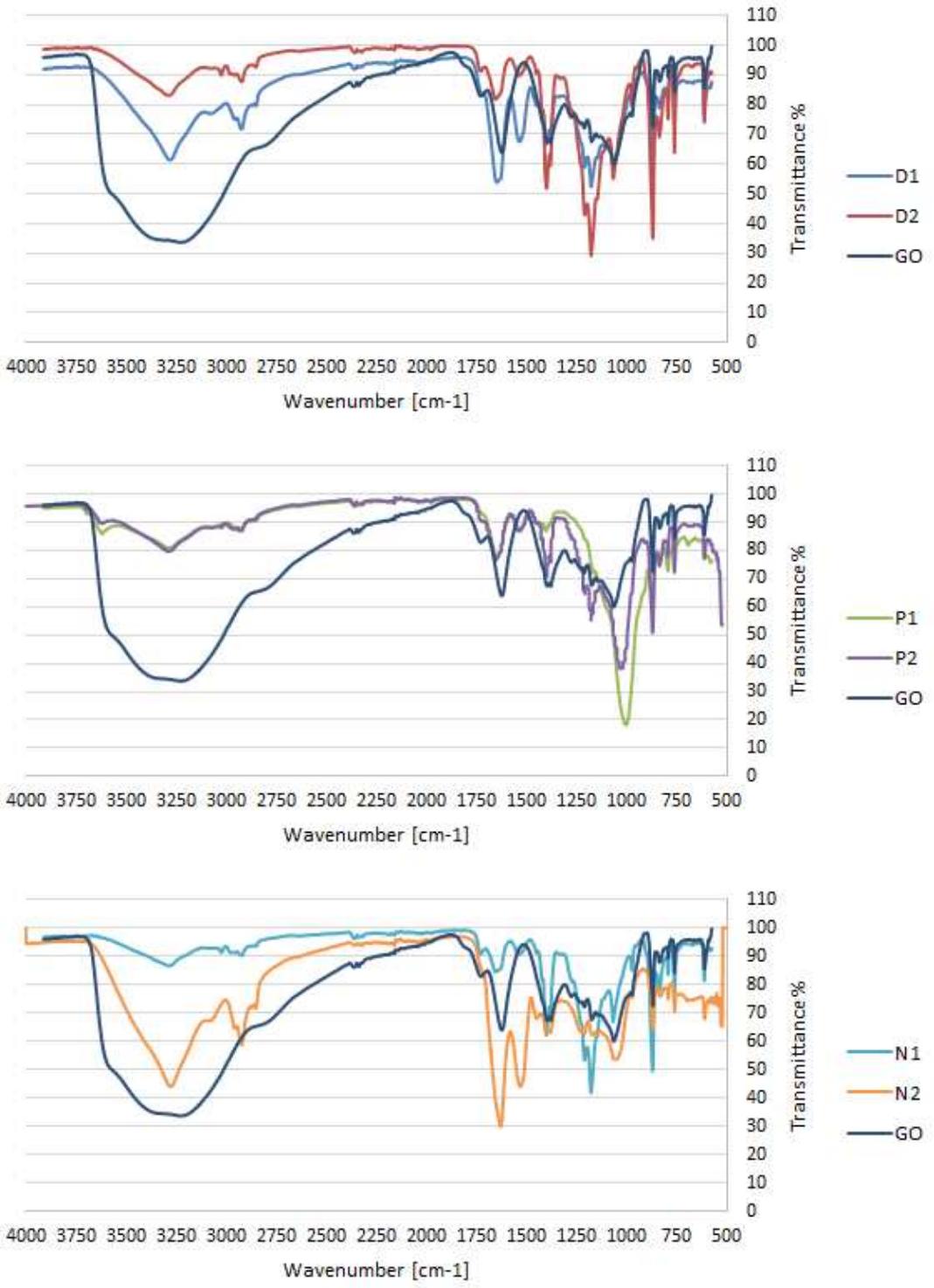


**Figure E7: FT**-IR spectrum of the SSR1 trial compared with a GO standard. Concentration in each sample varies affecting absorbance. Data collected early on the experiment on day 115

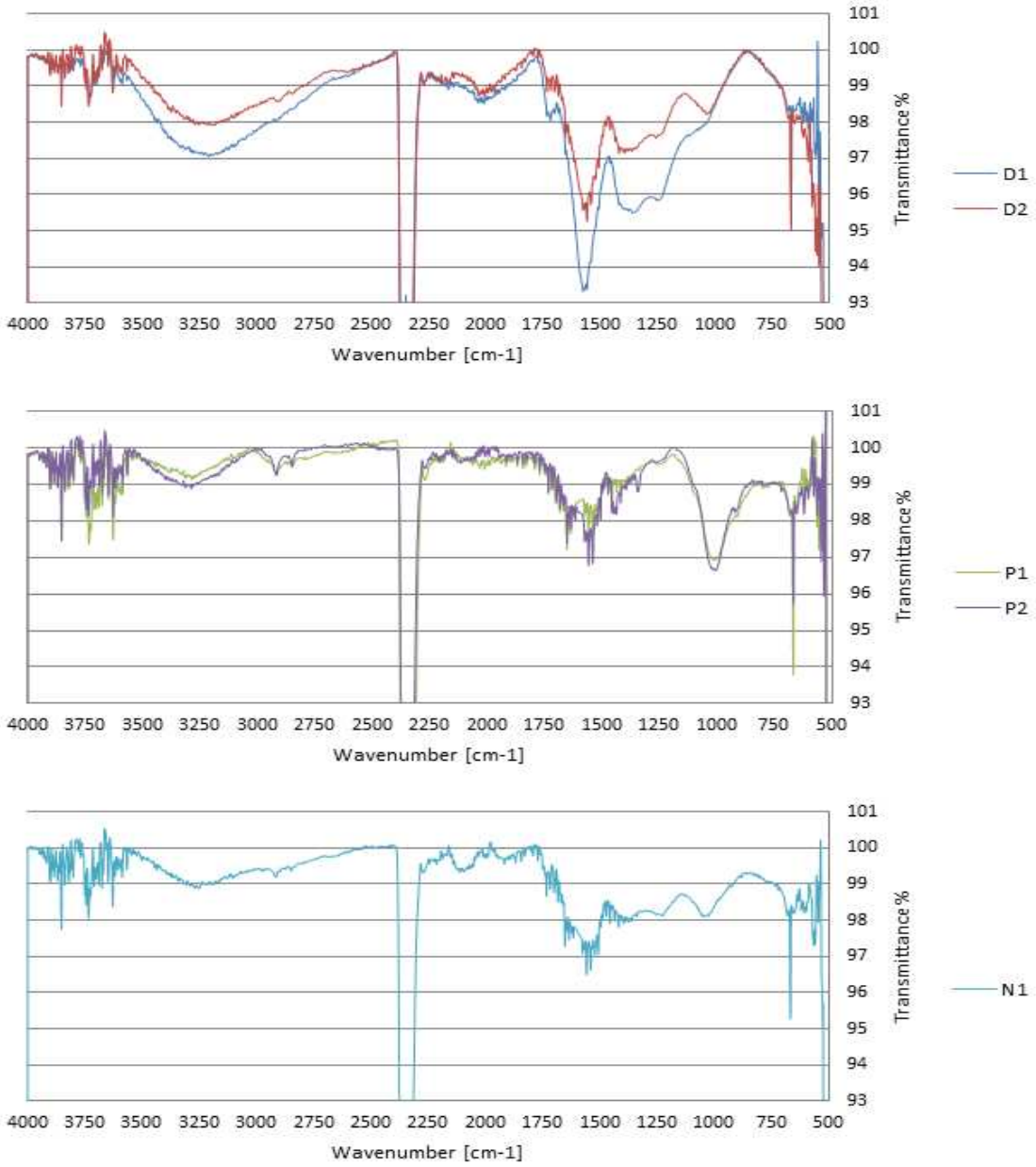


| ID | C-OH stretch/ hydroxyl groups | C-H Alkenyl stretch | C-H Alkyl stretch | C≡C Alkynyl | C=O stretch/ carbonyl | C=C aromatic bend | C-OH bend | C-O | O-H bend | C-O stretch of C-O-C /epoxy | C-O stretch of C-O /alcoxyl |
|---|---|---|---|---|---|---|---|---|---|---|---|
| D1 | 3232 | | | 2049 | 1722 | | 1564 | | 1365 | 1241 | 1035 |
| D2 | 3207 | 2885 | | 2040 | 1735 | | 1567 | | 1384 | 1247 | 1031 |
| P1 | 3297 | 2890 | | 2034 | | 1662 | 1550 | 1446 | | | 1018 |
| P2 | 3318 | 2923 | 2858 | 2098 | | 1645 | 1542 | 1540 | | 1253 | 1016 |
| N1 | 3247 | 2912 | 2850 | 2103 | 1720 | 1639 | 1538 | | 1367 | 1228 | 1045 |

**Figure E8:** FT-IR spectrum of the SSR1 trial at the end of the trial. Samples collected using the two-filtration system with solids in the BEGO membrane. Concentrations of the solids were low thus the low in absorbance

**TEM**

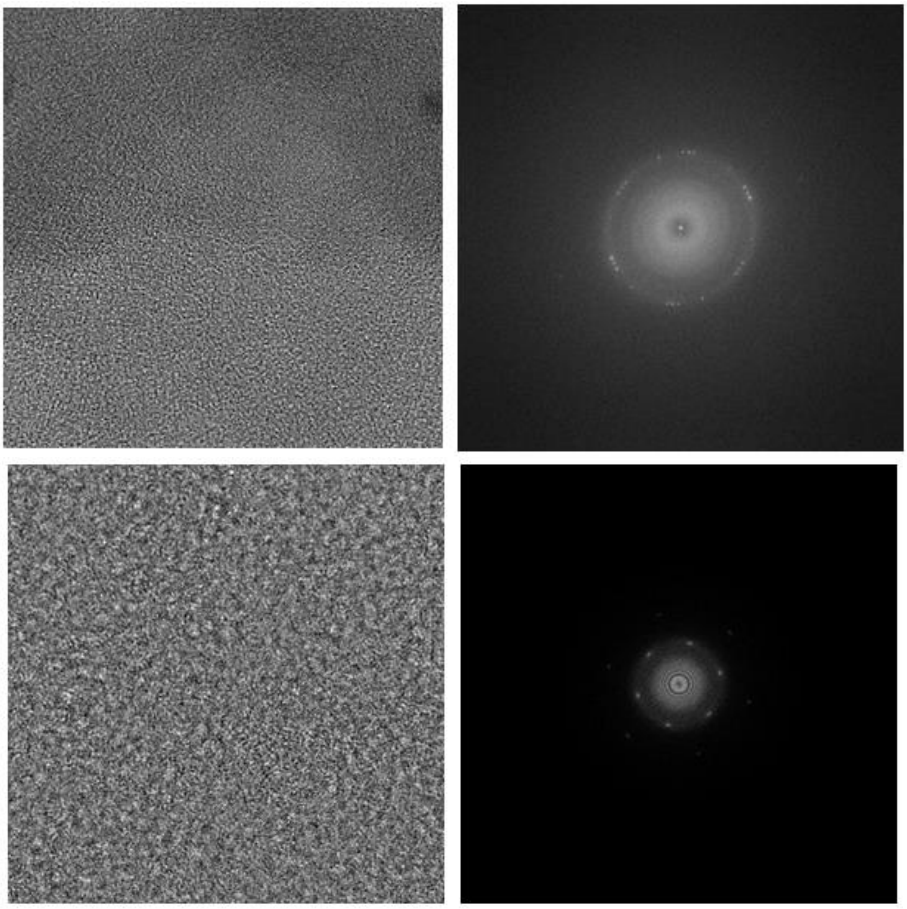

**Figure E9:** TEM images and FFT for the D1 (top) and D2 samples

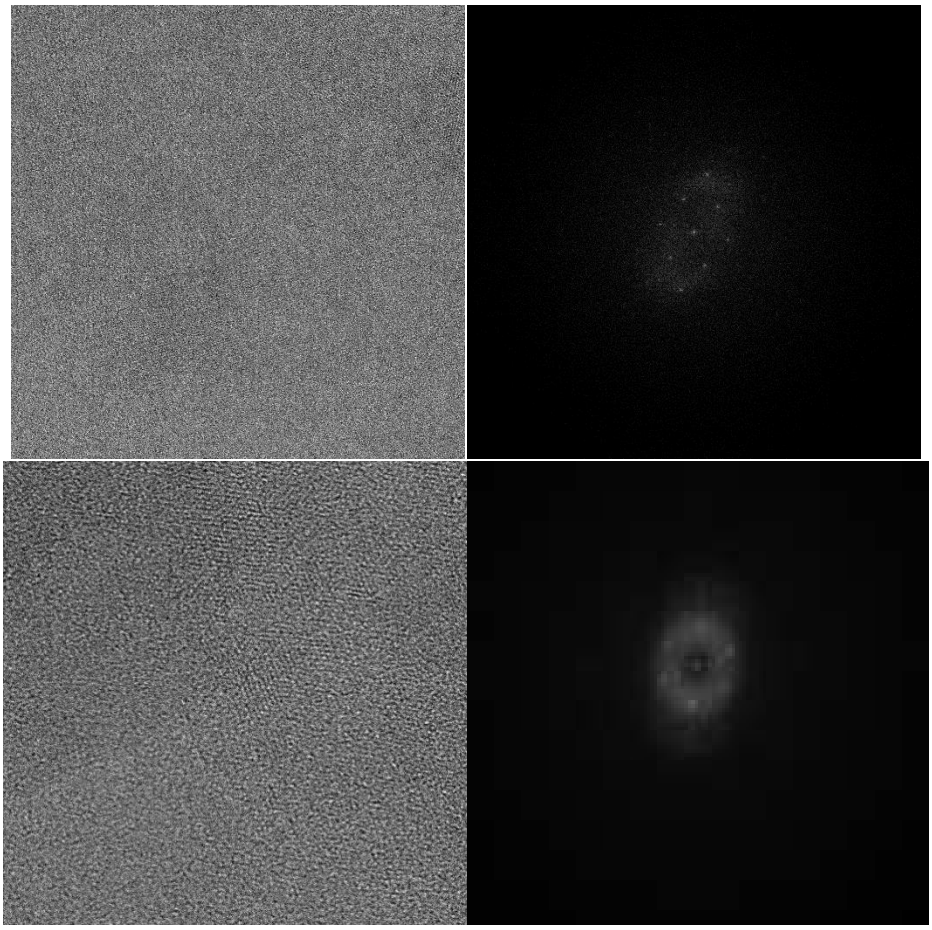

**Figure E10:** TEM images and FFT for the P1 (top) and P2 samples

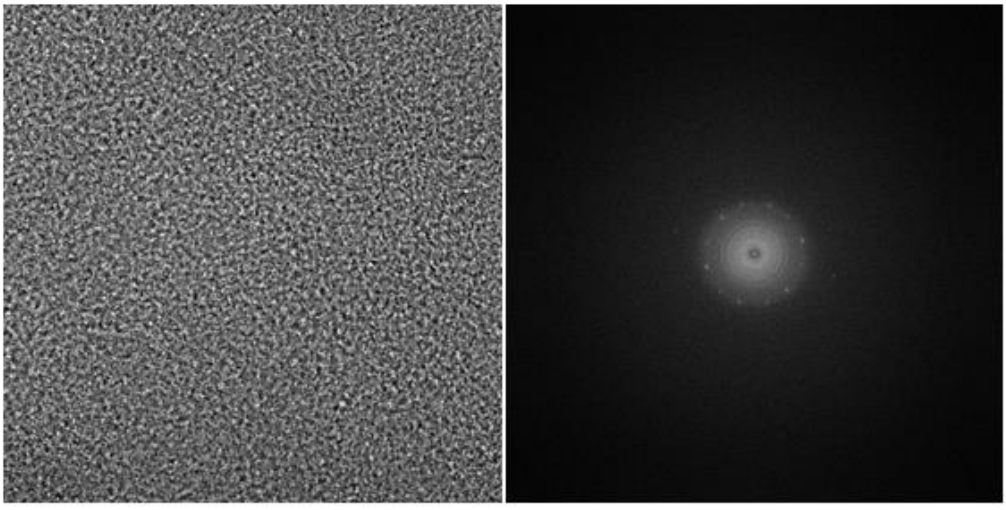

**Figure E11:** TEM images and FFT for the N1 sample

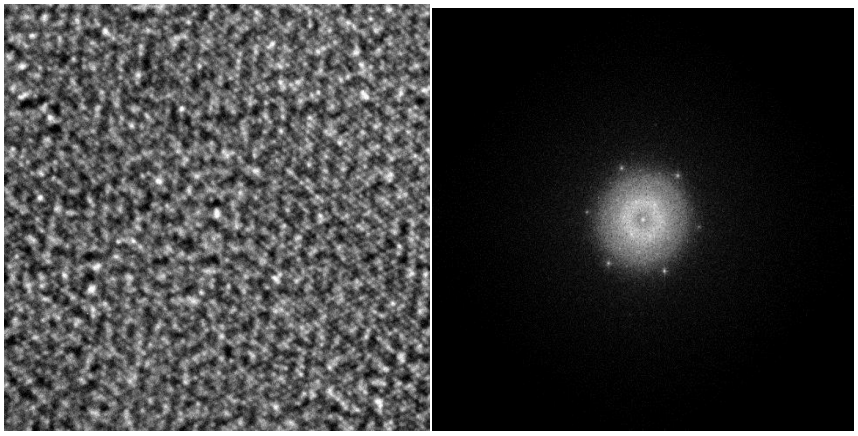

**Figure E12:** TEM image 11.4x10.6nm (left), and a FFT image of the section for sample taken from R2 reactor from LSR1

## AFM

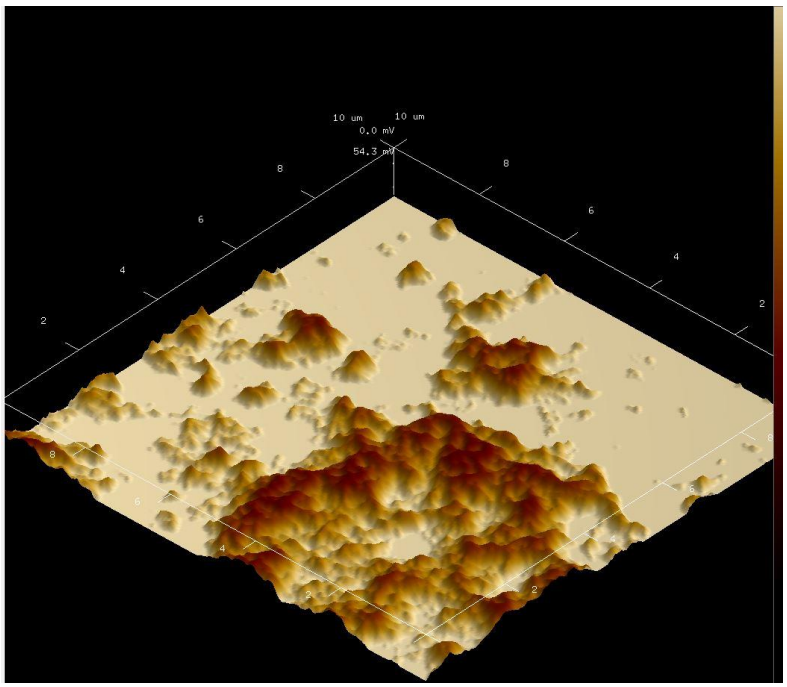


**Figure E13:** High senor 3D image of the R9 reactor diluted sample of the LSR2 trial

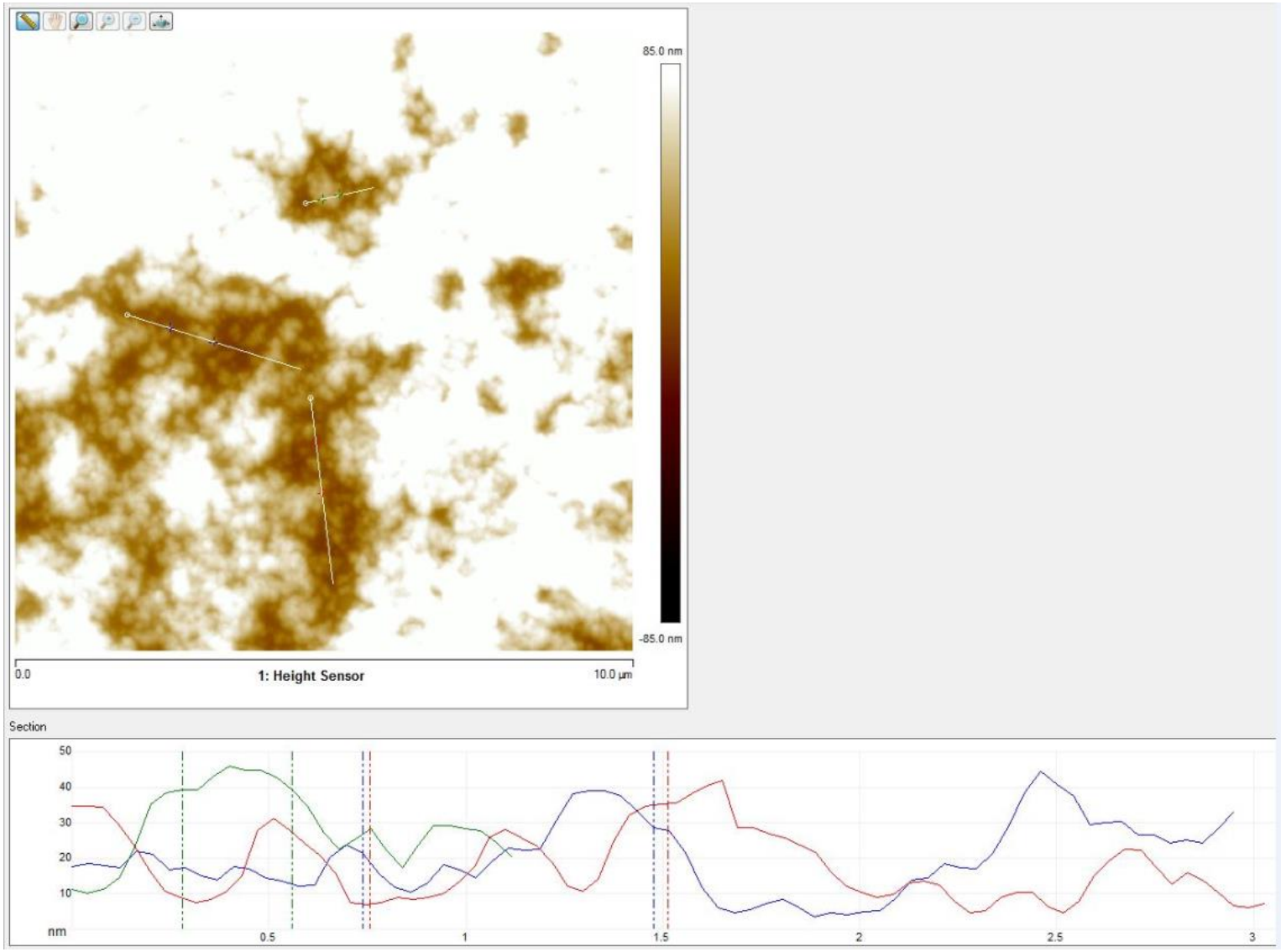


**Figure E14:** Step analysis on the R9 diluted sample from the LSR2 trial

**XPS**

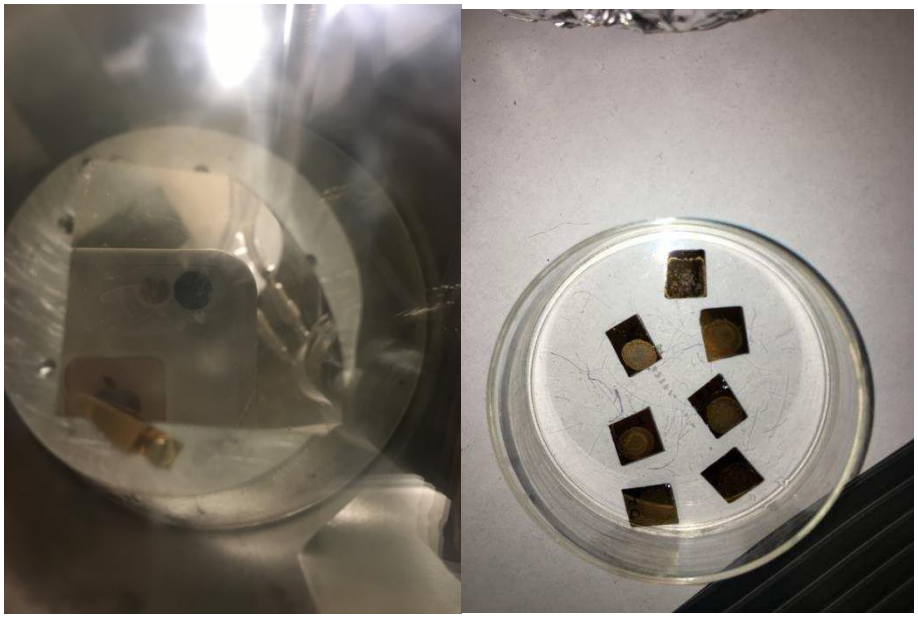

**Figure** E15: XPS samples inside of instrument on silica substrate (left), with samples later on top of a coating of gold to avoid contaminants from substrate in the XPS spectrum (right)

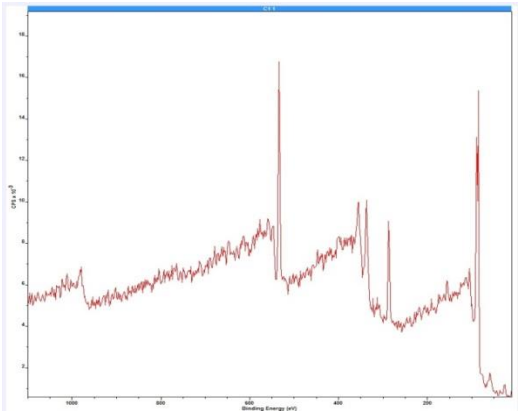

**Figure E16:** Survey scan of a D1 sample from SSR1

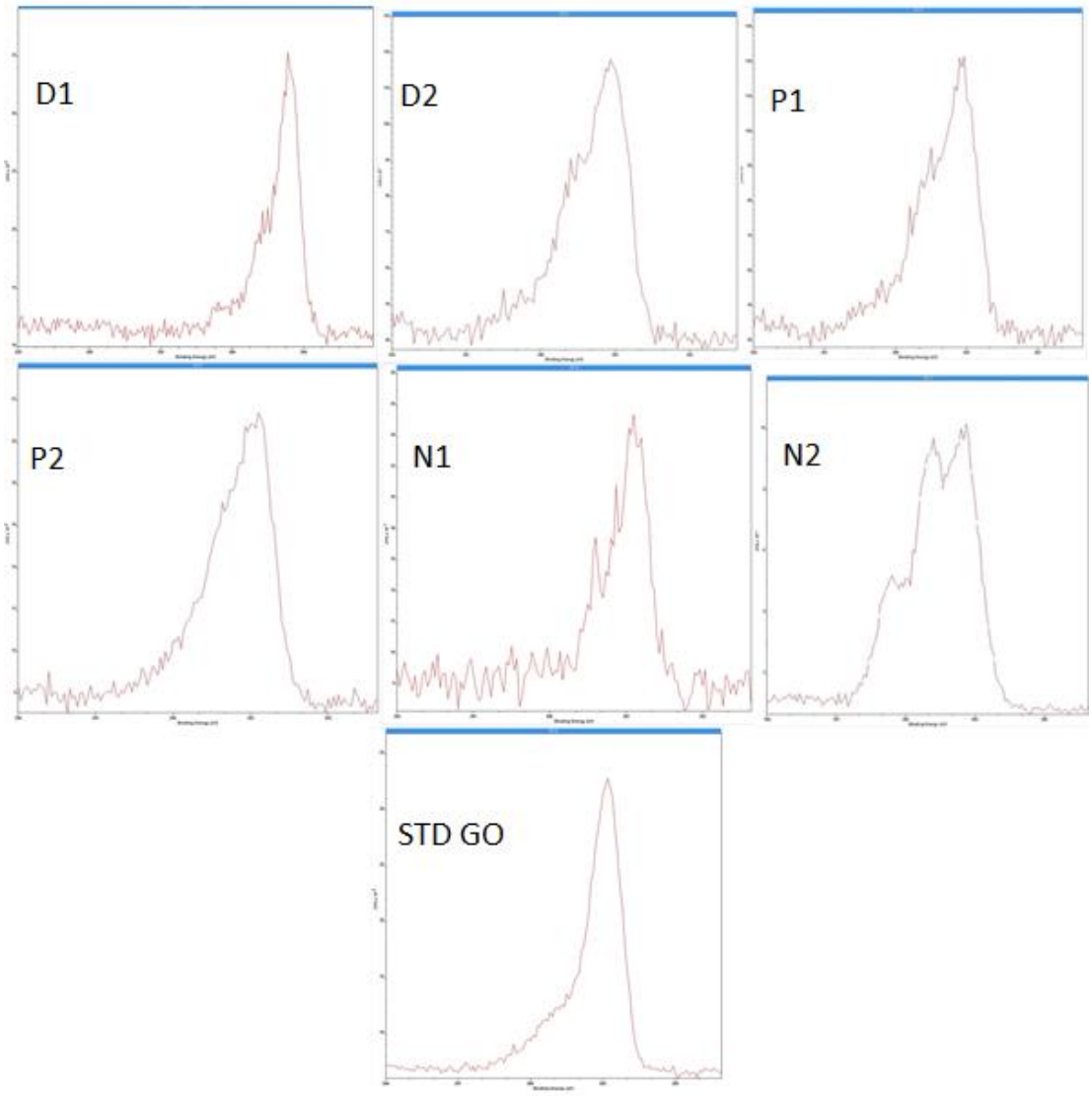


**Figure E17:** HR scan of carbon peak of Carbon HR peak data exported into CasaXPS of 1) D1 sample, peak height: ~35*10-2 CPS 10-1. 2) D2 sample, peak height: ~120*10-1 CPS 10-1 3) P1 sample, peak height: ~120*10-1 CPS 10-1 4) P2 sample, peak height: ~22*10-2 CPS 10-1 5) N1 sample, peak height. Screenshots directly from XPS imaging

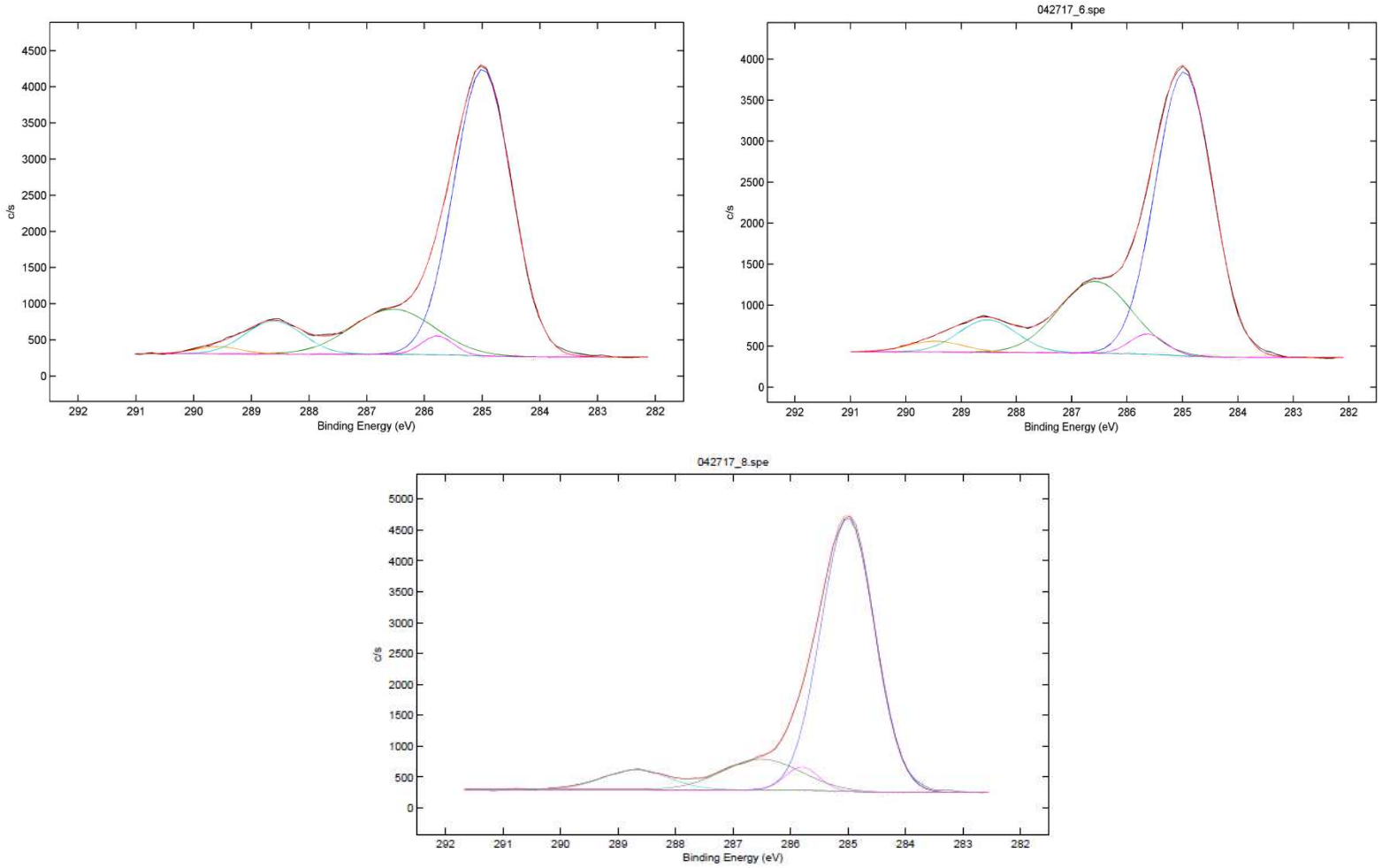


| Functional group | | Binding Energy [eV] |
|---|---|---|
| Hydrocarbon | C-H, C-C | 285 |
| Alcohol, ether | C-O-H, C-O-C | 286.5 |
| Carbonyl | C=O | 288 |
| Carboxyl, ester | O=C-O-C,O=C-OH | 289 |

**Figure E18:** HRES spectrum for C1 data with possible functional group distribution. Samples taken from R1 (top, left), R2 (top, right), R3 (bottom, left) of the LSR1 trial

## ICP-MS

**Table E19:** Key code of ICP-MS samples

| Sample ID | |
|---|---|
| Blanked in 2% HNO3 | |
| M | Media alone |
| Blanked in 2% HNO3 + 100µL media | |
| D1 | D1 potentiostat SSR2 |
| N1 | N1 potentiostat SSR2 |
| N3 | N3 potentiostat SSR2 |

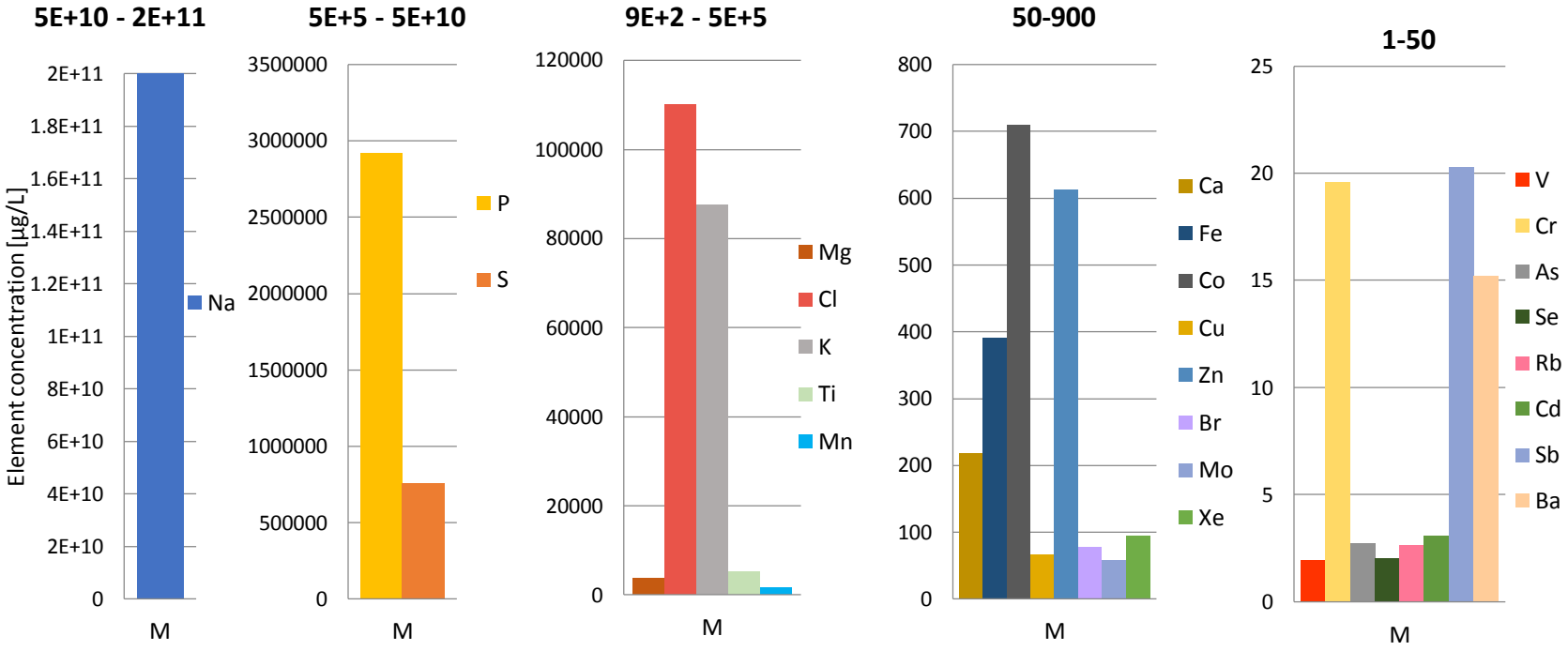


**Figure E20:** ICP-MS concentration of metals in the media at different concentration threshold

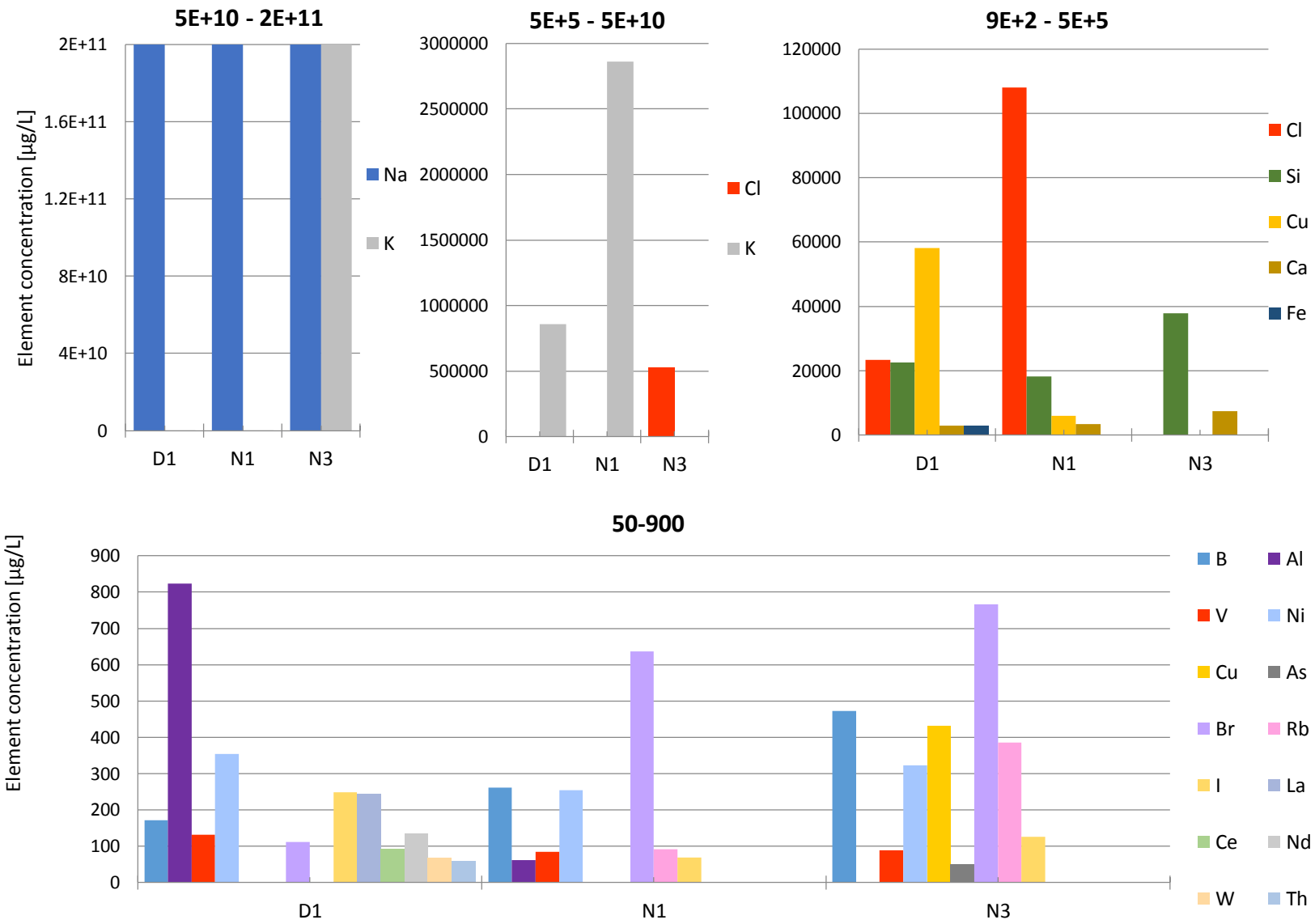


**Figure E21:** ICP-MS concentration of metals in the media in the SSR2 reactors at different concentration threshold

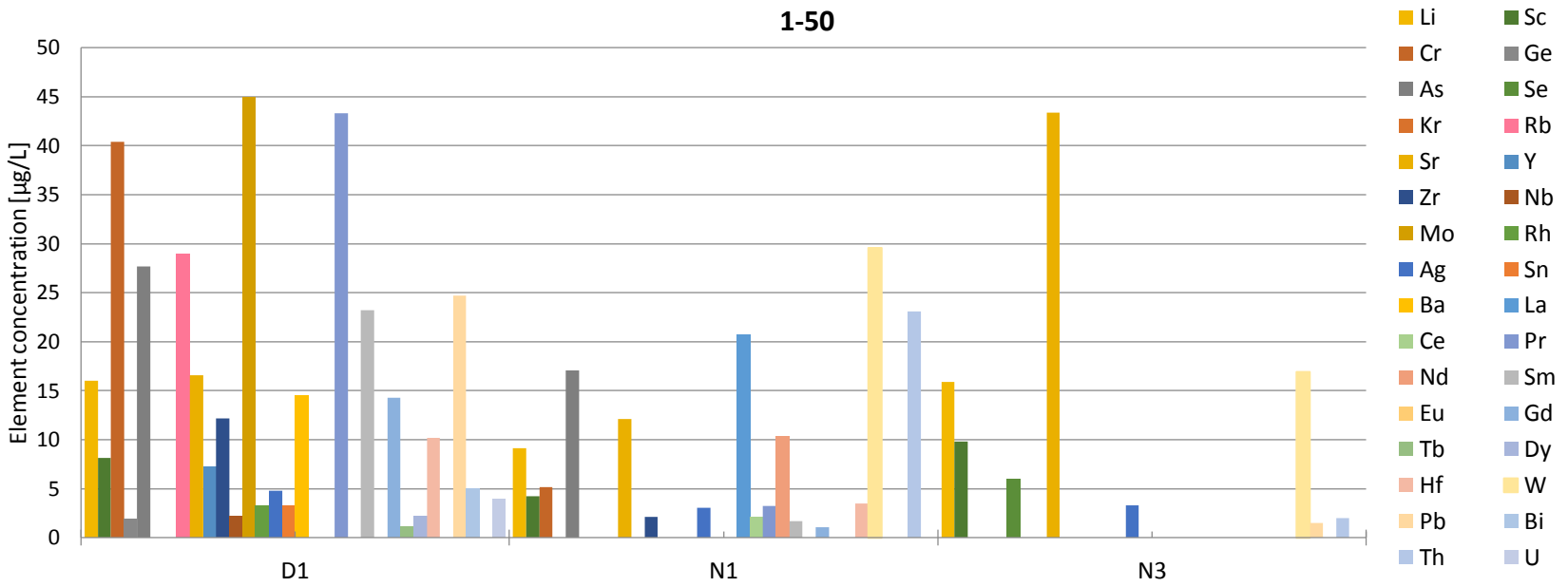


**Figure E22:** ICP-MS concentration of metals in the media in the SSR2 reactors at a trace concentration threshold

All of the reactor have very large salts concentrations (Na, K, Cl) possibly coming from leaks from the salt bridges (5E+10 - 2E+11 µL scale). These salts are more prominent in N3 which had been performing poorly from the beginning and showed the least detected BEGO production. All samples contain significant Si and Ca but only D1 and N1 have Cu at the 9E+2 - 5E+5 scale. At the same scale, D1 also has the largest amount of Fe.

At the 500-900 µL scale, both replicates of N show significant Br and Rb. All of the reactors contain B, V, Ni, and Ifollowed by B, Ni, Rb, V and I. D1 has a much larger concentration of Al and some traces of other metals not present in the N reactors at this scale such as La, Ce, Nd, and Th. N1 does have some Al at this scale bit N3 does not.

At the trace scale (1-50 µL), D1 shows a much richer mineral pool (N3 the least rich) with elements such as Cr, Mo and Pr as well as a much diluted amount of Rb compared to the N replicates in the scale before. Smaller amounts include Ba, Y, Bi, U, Sn, Rh, Nb, Dy, Ge, Tb from highest, to lowest concentrations (14.5-1.14µg/L). D1 and N1 have Zr, Sm, Gd, and Hf as well as As which is at a lower concentration compared to N3 in the scale before. N1 and N3 have smaller concentrations of La, Ce, Nd, W, and Th compared to D1 from the scale before. D1 and N3 contain Pb, D1 at a much larger concentration. N1 is the only reactor that has Nd, and N3 the only one that has Se. All reactors contain Li, Sc, Sr, and Ag.

**Conductivity in solution**

**Table E23:** Conductivity of DI water, media and purchased GO standards

| Standard solutions | |
|---|---|
| Reactor | Conductivity [µS/cm] |
| DI water | 0.87 |
| NG media | 6.74 |
| Pure GO (2mg/mL) | 193.8 |
| Pure GO (0.2mg/mL) | 70.4 |
| Pure GO (0.4mg/mL) | 22.4 |
| graphite (2mg/mL) | 10.1 |
| graphite oxide (2mg/mL) | 12.07 |

**Table E24:** Conductivity of the SSR1 bulk solutions on day 245

| SSR1 | |
|---|---|
| Reactor | Conductivity [µS/cm] |
| D1 | 5.84 |
| D2 | 6.02 |
| P1 | 7.3 |
| P2 | 6.56 |
| N1 | 6.85 |
| N2 | 7.81 |

**Table E25:** Conductivity of the LSR1 bulk solutions on day 54

| LSR1 | |
|---|---|
| Reactor | Conductivity [µS/cm] |
| R1 | 6 |
| R2 | 5.7 |
| R3 | 6 |

# APPENDIX F: MICROBIAL ANALYSIS

**Figure F1:** Relationships between collected samples of the SSR1 reactor microbial data from day 32

**Figure F2:** Microbial distributions between the most abundant communities per sample technique regardless of the inoculum source. Analysis was conducted on extractions done on day 32

**Figure F3:** LSR2 sequencing results at a phyla classification with 1% microbial cut-off at the end of the experiment

**Figure F4:** LSR2 sequencing results at a genus classification with 5% microbial cut-off at the end of the experiment

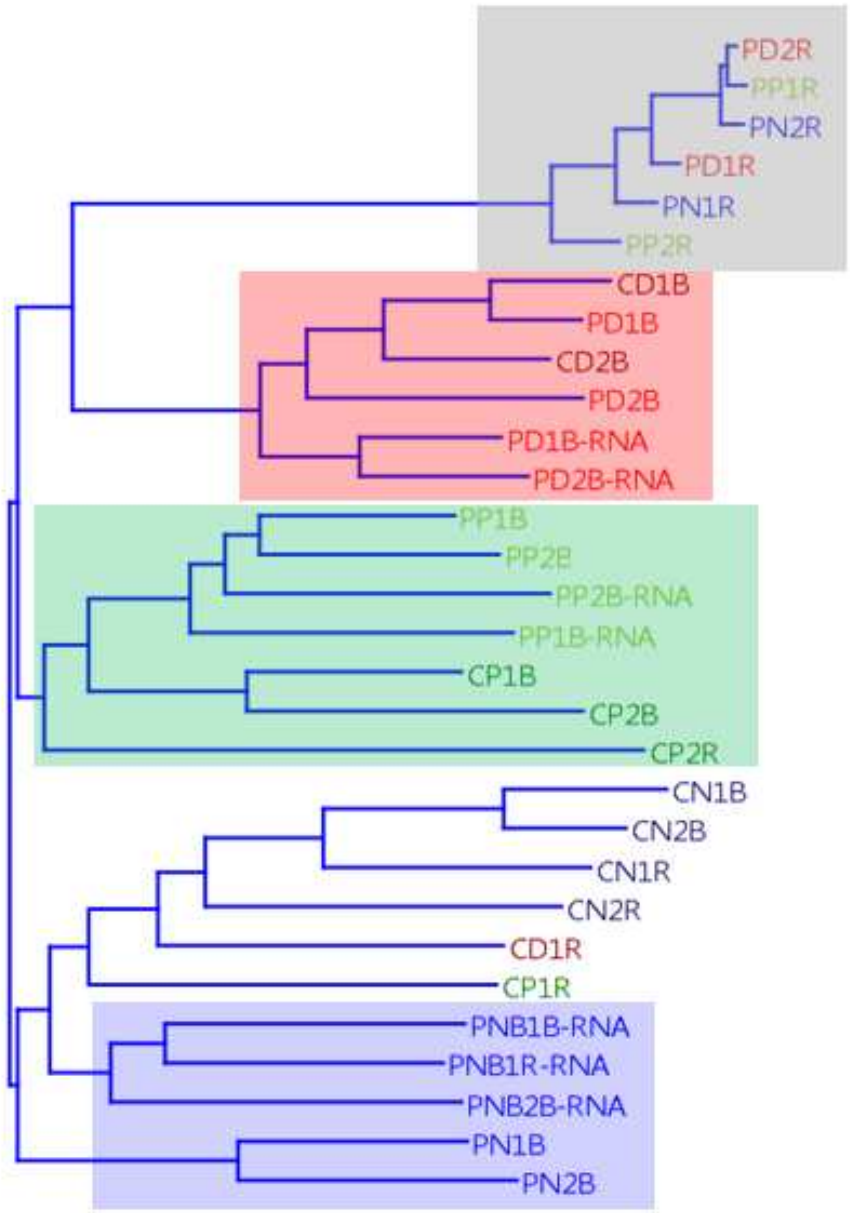


**Figure F1:** Relationships between collected samples of the SSR1 reactor microbial data from day 32

| | BULK-DNA | BULK-RNA | ROD-DNA | ROD-RNA |
|---|---|---|---|---|
| Unknown (Porphyromonadaceae) | X | X | | |
| Unclassified (Bacteroidales) | X | | | |
| Unknown (Bacteroidales) | X | | | |
| Unclassified (Bacteroidetes) | X | | | |
| Unknown (Bacteroidetes) | X | X | X | X |
| Candidatus Cloacimonas | X | | | |
| Ochrobactrum | X | | | X |
| Shinella | X | X | | |
| Comamonas | X | X | | X |
| Desulfobacula | X | X | | |
| Unclassified (Campylobacteraceae) | X | X | | |
| Sulfuricurvum | X | X | | |
| Pantoea | X | | X | |
| Sphaerochaeta | X | | | |
| Mesotoga | X | | | |
| Unknown | X | | | |
| Nodularia | | X | | |
| Unknown (Peptostreptococcaceae) | | X | | |
| Unknown (Rhizobiales) | | X | | X |
| Gemmobacter | | X | | |
| Dechlorospirillum | | X | | |
| Methylomonas | | X | | |
| Pseudomonas | | X | | X |
| Leucobacter | | | | X |
| Marinobacter | | | | X |

**Figure F2:** Microbial distributions between the most abundant communities per sample technique regardless of the inoculum source. Analysis was conducted on extractions done on day 32

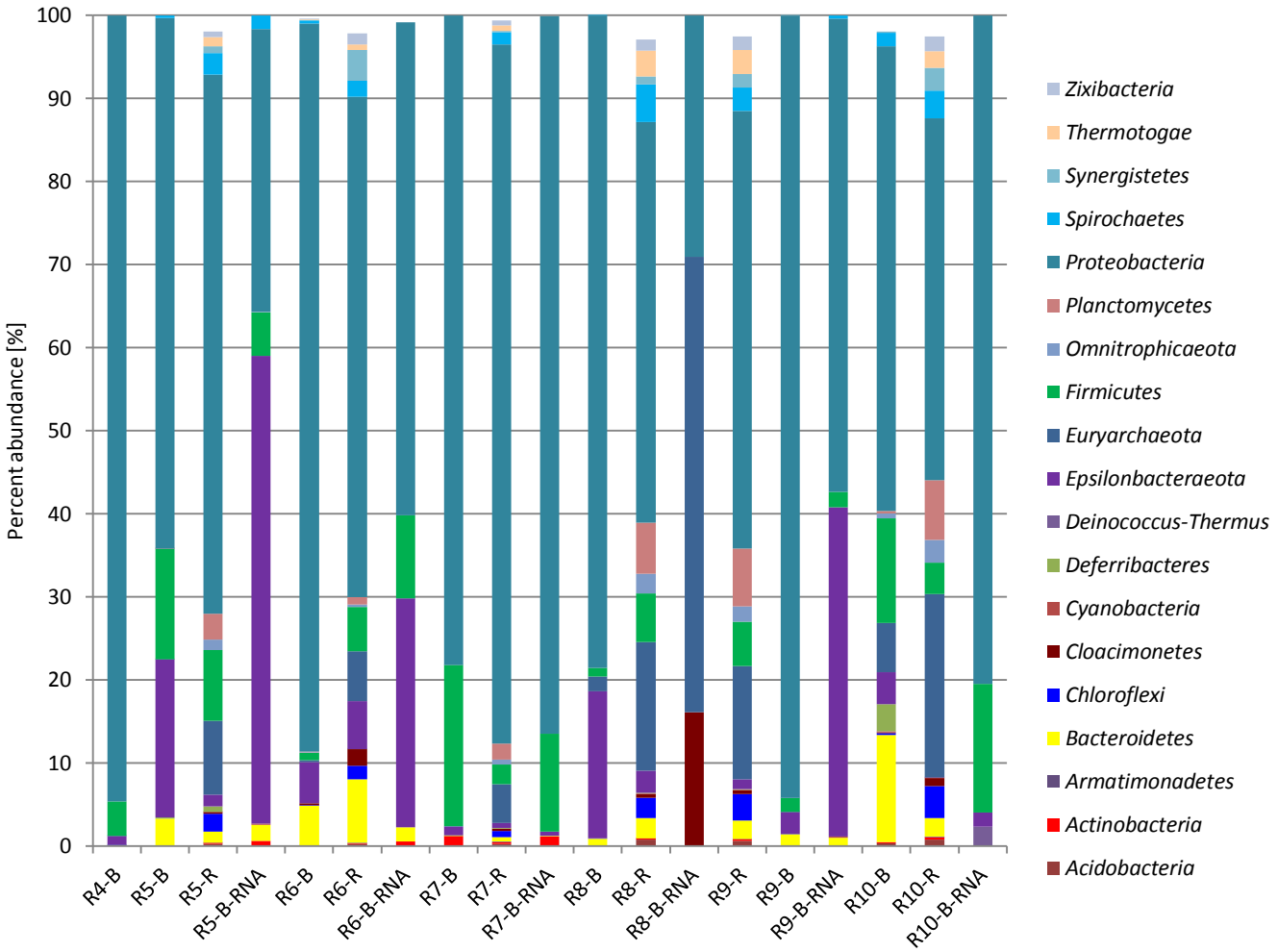


**Figure F3:** LSR2 sequencing results at a phyla classification with 1% microbial cut-off at the end of the experiment

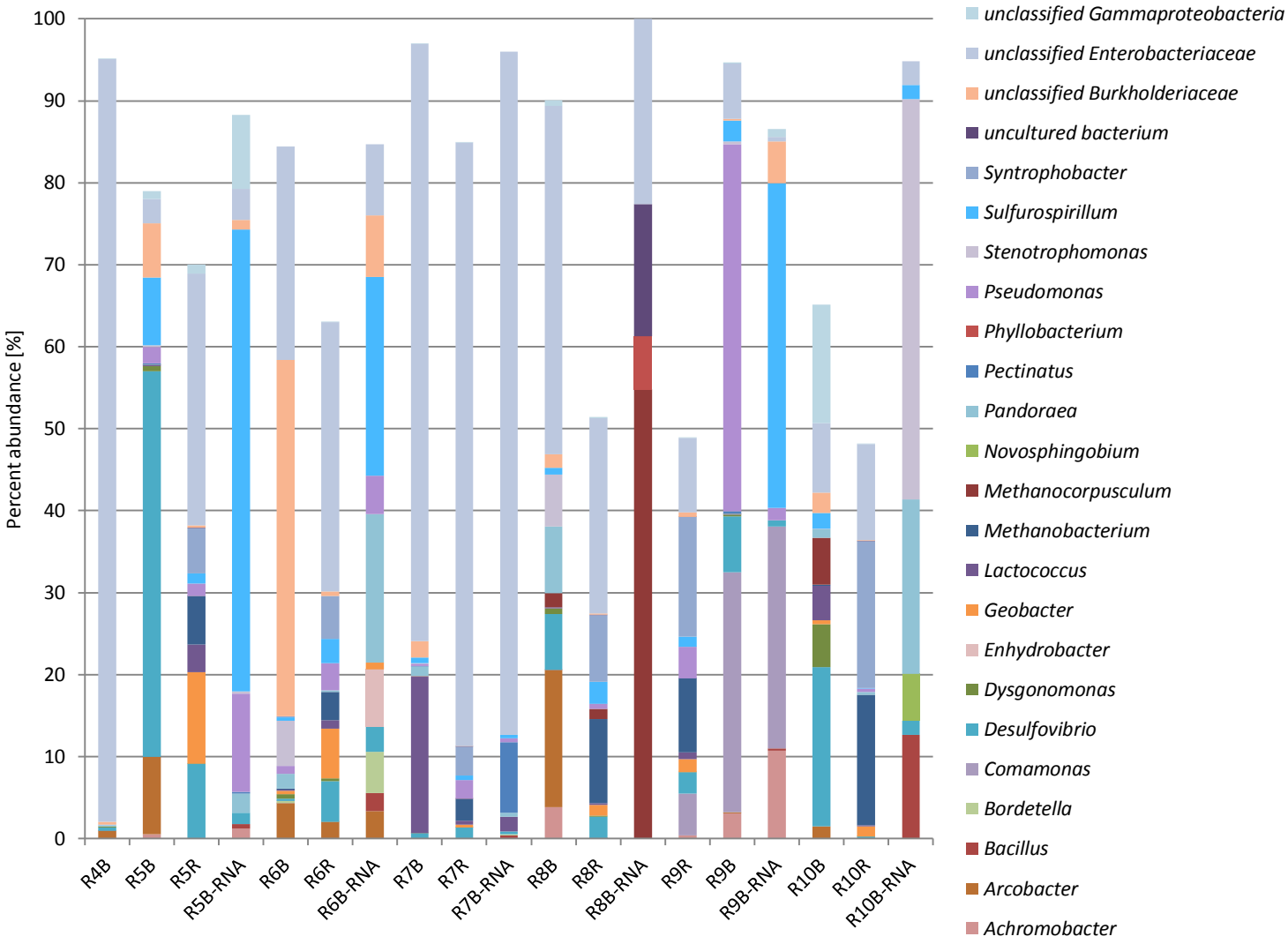


**Figure F4:** LSR2 sequencing results at a genus classification with 5% microbial cut-off at the end of the experiment